Improving Biospecimen Imaging in Liquid Phase Electron Microscopy

by

Nicolette Shaw

A thesis

presented to the University of Waterloo

in fulfillment of the

thesis requirement for the degree of

Master of Science

in

Chemistry

Waterloo, Ontario, Canada, 2023

© Nicolette Shaw 2023

Author's Declaration

This thesis consists of material all of which I authored or co-authored: see Statement of Contributions included in the thesis. This is a true copy of the thesis, including any required final revisions, as accepted by my examiners.

I understand that my thesis may be made electronically available to the public.

Statement of Contributions

In this work, I outline developments made to the fields of bioimaging, and liquid phase electron microscopy (LPEM). My MSc has involved work in the development of liquid cells (LCs) including exploration of materials, LPEM experiments, investigation of low-dose techniques, and development of open-source software. Contributions to the work described in this thesis were made by Dr. Ariel Petruk (AP), Tyler Lott (TL), Dr. Kostyantyn Pichugin (KP), and Professor Germán Sciaini (GS).

Design of initial LCs (Lott, 2023 in Figure 5.8) was performed by AP, TL, and GS. Myself, AP, TL, and KP fabricated all other nanofluidic chips in the University of Waterloo's Quantum-Nano Fabrication and Characterization Facility (QNFCF). TL, AP, and GS designed the LPEM holder and loading station. Myself, TL, and AP performed all LPEM experiments with guidance from Dr. Carmen Andrei and Dr. Natalie Hamada at the Canadian Center for Electron Microscopy (CCEM). AP, GS and I devised all fabrication experiments outlined in chapter 4, which were performed by myself with help from AP. I analysed all image and spectra data obtained from these experiments, and I designed and implemented code independently for all software produced in this thesis.

The work described in chapter 3 also appears in the supplementary information for the following publication.

Lott, T. S.; Petruk, A. A.; Shaw, N. A.; Hamada, N.; Andrei, C. M.; Liu, Y.; Liu, J.; Sciaini, G. Robust fully controlled nanometer liquid layers for high resolution liquid-cell electron microscopy. *Lab on a Chip* **2023**, DOI: 10.1039/D3LC00190C

The work described in chapters 3, 5.1 and 8 also appears in the following publication.

Shaw, N. A.; Lott, T. S.; Petruk, A. A.; Hamada, N.; Andrei, C. M.; Liu, Y.; Liu, J.; Sciaini, G. High-Throughput Low-Dose Biomolecule Imaging in Liquid Phase Electron Microscopy. *Microsc. Microanal.* **2023**. Minneapolis, MN, USA, July 23 - 27.

Additional co-authored work not included in this thesis.

Lott, T. S.; Petruk, A. A.; Shaw, N. A.; Hamada, N.; Andrei, C. M.; Liu, Y.; Liu, J.; Sci'aini, G. A High-Throughput Method for Bulgeless Liquid Cell Imaging in the Transmission Electron Microscope. *Microsc. Microanal.* **2023**. Minneapolis, MN, USA, July 23 - 27.

Abstract

This thesis highlights the progress made in LPEM and the study of biosamples. The introduction provides a comprehensive overview of the challenges encountered in investigating molecular processes and traces the historical evolution of microscopy, leading up to the development of transmission electron microscopy (TEM), cryogenic electron microscopy (cryo EM), and LPEM. Two major hurdles in LPEM are outlined and addressed in this thesis: LC transmissibility, and electron-induced biosample damage.

Low electron transmission in thick silicon nitride (SiN_x) LCs reduces the achievable resolution during imaging. To address this, I developed a technique to fabricate thin SiN_x windows. These windows exhibit reduced bulging, higher transmission, and higher resolution imaging in the liquid phase than currently available SiN_x cells. Implementation of thin SiN_x LCs was demonstrated through imaging of apoferritin, adeno-associated virus (AAV), pAAV, and vesicles at high resolution. Though future work remains to produce thin LCs of reproducible liquid thickness, this work demonstrates a breakthrough in the capabilities of LPEM imaging.

Another principal hurdle in LPEM lies in sample damage inflicted by the electron beam. The concept of radiolysis and its impact on biosamples is elucidated and demonstrated, showing the need to mitigate sample damage during imaging. The thesis addresses this challenge through the evaluation of inpainting techniques, which can be used to perform reduced-dose imaging. *In silico* analysis showed that algorithmic inpainting can be used to inpaint biosample images up to 80% with high accuracy. The analysis also showed that spiral inpainting does not significantly compromise image quality, indicating its potential

for performing low-dose imaging when spiral distortion is corrected.

Overall, this thesis provides invaluable technical insights into LPEM and the cutting-edge advancements made in this work. It sets the stage for future research endeavours and groundbreaking discoveries in the realm of *in situ* bioimaging.

Acknowledgements

I want to thank Dr. Natalie Hamada and Dr. Carmen Andrei at the CCEM for their expertise, patience, and help in using the TEMs at the facility. Also, thank you to Professor Brian Ingalls for allowing me to use the flow cytometer in his lab, Professor Josh Neufled for allowing me to use the ultracentrifuge in his lab, and Professor Scott Hopkins for donating CO_2 gas to my culturing efforts. I would also like to thank Professor Stephen Giovannoni and Dr. Chih-Ping Lee for providing the culture of *Pelagibacter communis* and providing guidance for culture maintenance.

The University of Waterloo's QNFCF facility was used for this work. This infrastructure would not be possible without the significant contributions of Canada First Research Excellence Fund (CFREF)-TQT, Canada Foundation for Innovation (CFI), ISED, the Ontario Ministry of Research and Innovation, and Mike and Ophelia Lazaridis. I would like to thank all the staff members and members of the QNFCF community for their support, in particular, Dr. Sandra Gibson for her guidance in using the atomic force microscope.

I would also like to acknowledge funding from the National Science and Engineering Research Council of Canada (NSERC), the CFI, the Ontario Early Researcher Award (ERA) program, and the CFREF, without which this research would not be possible. I would also especially like to thank the Chan Zuckerberg Initiative (CZI), which has provided many learning opportunities, as well as significant funding contributions to this work.

I would like to thank all the members of my lab, the Ultrafast Electron Imaging Lab (UeIL), in the Chemistry Department of the University of Waterloo. Particularly, thank

you to Tyler Lott and Dr. Ariel Petruk, who performed LC assembly and microscopy with me at CCEM throughout this project. Also thank you to Dr. Ariel Petruk, Dr. Kostyantyn Pichugin and Tyler Lott for their contributions to the fabrication of LCs in the QNFCF. I would like to give special thanks to Dr. Ariel Petruk for mentoring me in all nanofabrication processes, and working with me to fabricate thin SiN_x windows. Tyler Lott, Dr. Ariel Petruk, and Professor Germán Sciaini all deserve extra acknowledgement for their work on the UeIL loading station, holder, and nanofabricated LCs, which through the culmination of years of work, provided the foundation for this research.

I would finally like to thank my supervisor, Professor Germán Sciaini, for his teaching, guidance, encouragement, and understanding. Though this work came with unique trials, his support helped me persist. Thank you for making me a better scientist.

Dedication

To my beloved husband Daniele, whose love, support, and encouragement have been the driving force behind my academic journey. Your faith in my abilities has given me the courage to pursue my dreams and the strength to overcome any obstacle. Thank you, especially for your advice on how to make my code faster and more maintainable. I am grateful for every moment spent by your side, and for all the time together to come.

And to Fluffy, my furry feline companion, thank you for being so soft, and providing cuddles when I needed it most.

Table of Contents

Author's Declaration ii

Statement of Contributions iii

Abstract v

Acknowledgements vii

Dedication ix

List of Figures xv

List of Tables xviii

List of Code Repositories xix

List of Abbreviations xx

1 Introduction **1**

1.1 The evolution of microscopy . . . 2

1.2 Transmission electron microscopy . . . 3

1.3 Biological samples in transmission electron microscopy . . . 5

1.4 Liquid phase electron microscopy . . . 6

1.5 Liquid cells . . . 7

1.5.1 Carbon-based liquid cells . . . 7

1.5.2 Silicon nitride cells . . . 8

1.5.3 Microwells . . . 12

1.5.4 Hybrid cells . . . 12

1.6 Challenges for LPEM study of biomolecules . . . 13

2 Methods **16**

2.1 Fabrication of thin liquid cell windows . . . 16

2.1.1 Measurement of etch rates for Al_2O_3, TiO_2, and HfO_2 . . . 16

2.1.2 Measurement of stress for Al_2O_3 . . . 17

2.2 Microscopy methods . . . 18

2.3 Characterisation of thin nanofluidic cells . . . 19

2.3.1 EELS measurement of transmission data . . . 19

2.3.2 AFM characterisation of thin windows 19
2.3.3 Liquid cell assemblies for experiments showing liquid layer thickness 20
2.3.4 Liquid cell assembly 20
2.4 LPEM biomolecule imaging 21
2.5 Inpainting 23

3 Theoretical electron transmission through materials 24
3.1 Calculation of transmission 25
3.2 Liquid cell calculations 27

4 Fabrication of thin liquid cell windows 32
4.1 Nanofluidic cell design 32
4.2 Window release methods 34
4.3 Materials exploration 36

5 Characterisation of thin nanofluidic cells 41
5.1 Thickness determination with EELS 42
5.2 EElS thickness characterisation 43
5.3 Liquid cell characterisation 51

6 LPEM biomolecule imaging **57**

6.1 Adeno-associated virus 57

6.2 Ferritin and apoferritin 59

6.3 Vesicles 60

6.4 Plasmid DNA 60

6.5 Live cells 65

7 Data analysis tools **68**

7.1 Image data and metadata analysis 68

7.2 EELS data analysis 70

8 Mitigation of sample damage **74**

8.1 Dose 74

8.2 Reducing electron dose 75

8.3 Sparse sampling techniques 78

8.4 Inpainting methods 79

8.5 Implementation of inpainting 80

9 Conclusions and future outlook **86**

Bibliography **90**

Appendices **105**

A Photolithography **106**

B Inpainting results **108**

C Electron dose calculations **115**

C.1 Method 1: Screen current 115

C.2 Method 2: Counts to electrons 118

Glossary **119**

List of Figures

1.1 **Types of LC systems.** 9

1.2 **UeIL SiN_x liquid cells.** 11

3.1 **Theoretical transmission through LC materials.** 28

3.2 **Theoretical total mean free paths of LC compounds.** 30

3.3 **Thickness of water equivalent with transmission equivalent to 10 nm SiN_x.** 31

4.1 **Dimensions of the nanofluidic cell chips and assembly.** 33

4.2 **Cross sections of wafers showing thin window fabrication processes.** 35

4.3 **Etch rates of Al_2O_3, TiO_2, and HfO_2 films in standard nanofabrication wet process steps.** 37

4.4 **Stress measurements of thin Al_2O_3 films.** 39

5.1 **EELS spectra of a dry 5 nm SiN_x liquid cell assembly.** 45

5.2 **AFM measurements of broken 5 nm LCs.** 47

5.3 **AFM measurements of intact 5 nm LCs.** 48

5.4 **AFM scans across 5 nm freestanding SiN_x windows at different angles.** 48

5.5 **Theoretical and experimental transmission of inelastic electrons through SiN_x.** 50

5.6 **Images and FFTs of gold nanorods on dry 5, 15 and 60 nm SiN_x windows.** 52

5.7 **EELS line scan data of liquid assemblies made with two 5 nm membrane LCs.** 53

5.8 **LC chip design versions.** 55

5.9 **Two V09 chips after TEM, showing broken windows.** 56

6.1 **LPEM images of AAV.** 58

6.2 **LPEM images of apoferritin protein from equine spleen sample.** . 61

6.3 **LPEM images of ferritin protein in liquid.** 62

6.4 **LPEM images of vesicles in equine spleen sample.** 63

6.5 **LPEM images of pAAV plasmid DNA.** 65

6.6 **LPEM images of salt crystal formation in *Pelagibacter communis* sample.** 67

7.1 **Napari-EMD plugin for visualisation of EMD images, videos, and metadata.** 71

8.1 **Low dose imaging techniques.** 77

8.2 **Basic rationale for algorithmic inpainting.** 80

8.3 **Inpainting results for biomolecule images at 80%.** 82

8.4 **Inpainting quality assessments.** 84

8.5 **Inpainting quality assessments comparing spiral and random masks.** 85

A.1 **General scheme for patterning a mask on a wafer via photolithography.** 107

B.1 **Inpainting results for selected image of vesicles.** 109

B.2 **Inpainting results for selected image of AAV.** 110

B.3 **Inpainting results for selected image of pAAV plasmid.** 111

B.4 **Inpainting results for selected image of vesicles.** 112

B.5 **Inpainting results for selected image of salt.** 113

B.6 **Inpainting results for selected image of gold nanoparticles.** 114

C.1 **Image of vesicles to estimate dose rate.** 116

List of Tables

2.1 **Annealing conditions for Al_2O_3, TiO_2, and HfO_2 thin films.** 17

2.2 **Etching conditions for Al_2O_3, TiO_2, and HfO_2 thin films.** 17

2.3 **LC assembly configurations for 5nm membranes shown in Figure 5.7** 20

2.4 **LC assembly configurations for biomolecule data in Figures 6.1 of AAV, 6.2 of apoferritin, 6.4 of vesicles, 6.5 of plasmid DNA, and 6.6 of salt crystals.** 23

C.1 **Metadata summary for the image of vesicles describing dose.** . . . 117

List of Code Repositories

Estimating electron transmission from theoretical electron scattering data:

https://github.com/UeIL-Waterloo/Electron_transmission

Viewing EMD file images and metadata in the graphical user interface, Napari:

https://github.com/NickiShaw/napari-EMD

Extracting images and metadata from EMD files, and analysing EELS data including estimation of water thickness:

https://github.com/NickiShaw/microscopeFileProcessing

Inpainting images using Telea and Biharmonic inpainting algorithms, with random or spiral masks:

https://github.com/UeIL-Waterloo/InpaintingEMdata

List of Abbreviations

Λ_{tot} total mean free path, Glossary: total mean free path (Λ_{tot})

λ_{inel} inelastic mean free path, Glossary: inelastic mean free path (λ_{inel})

SiN_x silicon nitride

$\boldsymbol{r}$ pearson correlation coefficient

AAV adeno-associated virus

ADF annular dark field

AFM atomic force microscopy, Glossary: atomic force microscopy (AFM)

ALD atomic layer deposition, Glossary: atomic layer deposition (ALD)

BF bright field

CCEM Canadian Center for Electron Microscopy

CLV constant linear velocity, Glossary: constant linear velocity (CLV)

cryo EM cryogenic electron microscopy, Glossary: cryogenic electron microscopy (cryo EM)

CTEM conventional transmission electron microscopy, Glossary: conventional transmission electron microscopy (CTEM)

EELS electron energy loss spectroscopy

HAADF high-angle annular dark field

KOH potassium hydroxide

LC liquid cell, Glossary: liquid cell (LC)

LPCVD low-pressure chemical vapour deposition, Glossary: low-pressure chemical vapour deposition (LPCVD)

LPEM liquid phase electron microscopy

QNFCF Quantum-Nano Fabrication and Characterization Facility

RIE reactive ion etching

RMSE root mean squared error

RTP rapid thermal processor

STEM scannning transmission electron microscopy, Glossary: scannning transmission electron microscopy (STEM)

TEM transmission electron microscopy

UeIL Ultrafast Electron Imaging Lab

ZLP zero loss peak, Glossary: zero loss peak (ZLP)

Chapter 1

Introduction

On the edge of biochemical research, scientists strive to understand the intricate mechanisms by which molecular processes drive life. These processes that create life are still barely understood, largely due to the fact that biomolecules such as proteins, DNA, and even larger viruses and cells, are so small that they are difficult to study. For centuries scientists have developed methods to study molecular processes on large scales. Now the tools to study single particle dynamics are being pioneered, and are poised to revolutionise the way we understand living systems.

This chapter aims to provide a brief overview of transmission electron microscopy (TEM), and how developments in this field have led to the dawn of liquid phase electron microscopy (LPEM). Then, challenges in LPEM and biomolecule imaging in TEM will be introduced to provide context to the work I have undertaken for this thesis.

1.1 The evolution of microscopy

The first use of a microscope is often traced to the 1670s when Dutch scientist Antonie van Leeuwenhoek founded the field of microbiology through his observations of bacteria at ∼300 times magnification.[2] Centuries later in 1838, Dutch chemist Gerardus Johannes Mulder and Swedish chemist Jöns Jacob Berzelius discovered proteins, long before these particles would ever be seen with a microscope.[3] It was not until 1931 that Ernst Ruska and Max Knoll, two electrical engineers working in Berlin, built the first TEM.[4] At the time, the second generation TEM built by Ruska had approximately 500 Å resolution, which could still not visualise proteins.[4] However, the impact electron microscopy would have on biology and medicine was known even then. Research in TEM is so impactful, that only 31 years after Ruska received the noble prize for his work, another nobel prize was awarded to groundbreaking research in cryogenic electron microscopy (cryo EM).[4,5]

The first microscopes used light to create images, but resolution in optical microscopy is limited by the Abbe diffraction limit.[6] This limit states that the resolution limit (d) of a light microscope is equal to half of the wavelength (λ) of the imaging light. The light must pass through a numerical aperture, which will produce a cone of light with angle θ, travelling through a medium of refractive index n. This limit is also described similarly through the Rayleigh criterion.[7]

$$d = 1.22\frac{\lambda}{2nsin(\theta)} \tag{1.1}$$

The best resolution achievable with light microscopy was then considered to be approx-

imately 200 nm (half the smallest wavelength of visible light),[8] or 1000X magnification.[2] Thus the smallest particle that could be seen with optical microscopy was bacterial cells.[2] However, in 1924 Luis deBroglie discovered that particles can be expressed as waves, opening the door for electron microscopy.[9] Higher electron accelerating voltages produce smaller wavelengths, thus conferring higher resolution. Electron microscopy was a fantastic step for research in biomolecule structures. Unsurprisingly, once electron microscopes were built, some of the first experiments done by Helmut Ruska (alongside Ernst Ruska), were the visualisation of viruses (pox viruses, tobacco-mosaic virus, varicella-zoster virus, and bacteriophages).[8,10]

1.2 Transmission electron microscopy

Transmission electron microscopy works by passing an accelerated beam of high-energy electrons through a sample in a vacuum chamber. Some but not all electrons are scattered via interactions with the sample. The electrons then hit a detector which records the electron counts, translating to pixel intensities in an image. The microscope employs a host of electromagnetic lenses and apertures to focus the electron beam produced by the source. High-resolution electron microscopy typically occurs above 100 keV accelerating voltage, thus over approximately half the speed of light.[11]

Electrons scatter as a function of the Coulomb (electrostatic) potential they experience as they pass atoms in the sample.[12] There are two types of scattering that occur: elastic scattering, where electrons appear at high scattering angles, and inelastic scattering, where electrons appear at low angles (<10 mrad).[12] Inelastic, elastic and unscattered electrons

are measured in electron energy loss spectroscopy (EELS), where the unscattered and elastically scattered electrons produce a zero loss peak, and inelastically scattered electrons produce a core loss peak.[13] Measuring EELS spectra is key in determining the liquid layer thickness (see setcion 3).[14]

There are also two types of imaging modes in the TEM: conventional transmission electron microscopy (CTEM), and scannning transmission electron microscopy (STEM). In CTEM mode, the microscope used a beam spread over the frame area to acquire an image. In STEM mode the beam is focused to a point (known as a probe), and scanned across the sample in a raster fashion. STEM detectors are split into 3 categories depending on their collection angles: bright field (BF) at <10 mrad, annular dark field (ADF) at 10-50 mrad, and high-angle annular dark field (HAADF) at >50mrad.[12] Because the HAADF and ADF detectors are shaped as annular rings, thus EELS spectra can be obtained using the central transmitted electrons simultaneously.[13] BF measures unscattered electrons, where ADF and HAADF measure scattered electrons.[15] HAADF signals are collected at high angles thus measures predominately elastic scattering.[12]

HAADF STEM measures elastic scattering, and is more sensitive to changes in electron mass, also referred to as Z contrast.[16] STEM mode imaging is better at imaging samples where the difference between the sample and background is high than TEM mode imaging.[17] However, when light (low-mass) samples such as biomolecules are imaged in water, there is very little Z contrast, thus TEM is typically able to gain higher-resolution images.[16,17]

TEM images are created from transmitted electrons, which create a BF image. The loss

of scattered electrons blocked by an aperture can generate an image.[15] However, sufficiently thin and light samples like biomolecules, produce images through phase contrast.[18] The biomolecule sample imparts a phase shift, which is not visible in the image result, however with some defocus the phase shift will cause constructive/destructive interference, which will produce a signal in the image.[18]

1.3 Biological samples in transmission electron microscopy

Initially, the major drawback of studying biomolecules with TEM was the need to fix, dry, and stain samples with heavy metal salts to protect samples from the vacuum in the microscope, and achieve sufficient contrast for particles to be seen.[19] In 1981, vitrification techniques were being investigated as an alternative way to preserve samples in vacuum environments, the foundation for cryo EM.[19] Utilisation of this technique led to the measurement of a 7.5 Å structure of the 50S ribosome in 1999.[20] Prior to the advent of cryo EM, most protein structures were discovered with x-ray crystallography, but today cryo EM has become a much more convenient technique for structure determination.[5] In early 2020, the Electron Microscopy Data Bank (EMDB) gained its 10,000th biological structure acquired using cryo EM.[5]

Cryo EM has been a key step in furthering our ability to study biological systems at high resolution, pushing technology from sample preparation to image and structural analysis to achieving up to 1.25 Å resolution (atomic resolution) in 2020.[21] However,

concurrent advancements in LPEM, have showed promising results in elucidating structures of biomolecules as well.[22]

1.4 Liquid phase electron microscopy

Where cryo EM experiments must acquire time series of vitrification procedures to yield dynamics, LPEM provides real-time dynamics, which can yield tremendous insight into biological systems.[23] The dynamics between biomolecules can give insights into a massive range of systems: cell-to-cell signalling, DNA-protein interactions, drug-receptor interactions, immunological cascades, biomineralisation, and more.

The major hurdle to imaging liquids in a TEM was the ability to shield the liquid sample from the vacuum environment required for transmission of the high energy electrons without discharging.[24] In 1942, scientists demonstrated the first successful *in situ* microscope experiment in low-pressure gas, protected from the electron microscope vacuum by a Lenard window, to image colloidal silver particles.[25] In 1944, the first liquid phase experiment was performed using a closed nitrocellulose cell.[24] Many advancements in nanofabrication technology eventually led to the first demonstration of liquid phase *in situ* experiments with silicon nitride (SiN_x) liquid cells (LCs) in 2003.[26] LPEM has recently begun to reach high-resolution structural reconstruction of viruses at 3.4 Å resolution, on part with many cryo EM experiments.[22]

In addition, liquid phase experiments have been demonstrated to have lower rates of sample damage induced by the electron beam, due to the increased rate of diffusion of

radicals.[22,27] With new developments in LPEM technology, LPEM is poised to become the new forefront for high-resolution biological imaging, offering both structural and dynamic information.[23] Developments in methods to enclose liquid samples in LCs have been key in the development of LPEM.

1.5 Liquid cells

LC are used to enclose liquid samples to protect them from the vacuum environment of the electron microscope. There exist multiple types of LCs: graphene, and amorphous carbon LCs (in conjunction referred to as carbon-based LCs), SiN_x LCs, and a combination of carbon and SiN_x - hybrid cells (all depicted in Figure 1.1). Though all LCs are capable of enclosing liquid samples for viewing in an electron microscope, there are strengths and weaknesses to each system.

1.5.1 Carbon-based liquid cells

Carbon-based liquid cells include two types of LCs: graphene and amorphous carbon. These LCs are assembled rather laboriously, through the assembly of two thin sheets of material that encapsulate a liquid sample in droplets (Figure 1.1B).[28,29] The motivation for using carbon-based materials is that they are very thin and light, thus very transmissive and able to confer very high-resolution data.[30] Because of the way samples are encapsulated, pockets of water are created and the samples have to be searched for throughout the film layers.[31] These films are susceptible to the formation of cracks, so the self-sealing pockets

are advantageous in this regard.[28] However, cracks in these carbon-based membranes may not always be apparent, especially in tightly encapsulated samples with little movement, and the liquid can shift to a gel state as evaporation occurs..[28] Additionally, the process of encapsulating samples in carbon-based LCs involves an evaporation step,[28,29] which is not ideal for experiments on samples where buffer systems or concentrations must be kept constant.

The first carbon LCs were made of single-layer graphene, which is the most transmissive material available in LCs.[30] In addition, graphene has been shown to confer reduced radiolytic damage to samples, which has been attributed to the radical scavenging properties of this material.[32,33] However, graphene LCs are fragile, and hydrophobic, thus they are susceptible to breaking and dewetting.[28] Amorphous carbon is a more durable alternative to graphene LCs .[23] and thus has gained popularity in recent years as they are still very transmissive.[23]

1.5.2 Silicon nitride cells

SiN_x liquid cells allow more flexibility in LC design, and reproducibility offered from silicon fabrication techniques.[34] In typical drop-cast LC systems, two chips made of silicon are fabricated with freestanding SiN_x windows, and a spacer placed between the chips (Figure 1.1A). SiN_x LCs can be patterned with electrodes, and integrated with liquid flow, and heating.[24] SiN_x LCs also have the ability to confer reproducible and uniform liquid layers, which carbon-based techniques do not.[1] Standard SiN_x LCs are also more durable than carbon-based LCs,[29] and it is very apparent when windows break, thus removing the danger

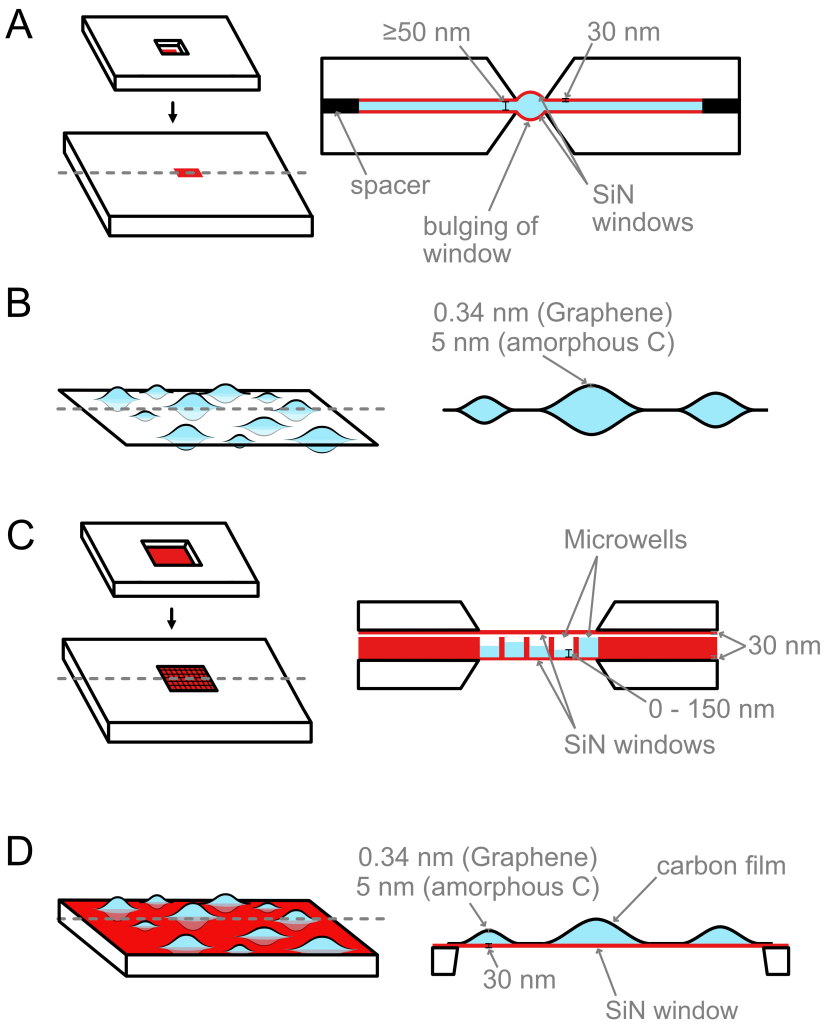


Figure 1.1: Types of LC systems. Each system shows the general view (left) and cross-section (right, as depicted by the grey dashed line). Panel A shows a generic silicon nitride LC, where two silicon chips enclose liquid in an area separated by a spacer, and the freestanding window is experiencing bulging. Panel B shows a carbon-based cell, where two thin films encapsulate pockets of liquid. Panel C shows a microwell LC, a type of silicon nitride cell where the liquid sample fills smaller well structures, enclosing different liquid thicknesses across different wells. Panel D shows a hybrid cell, where a carbon film encloses pockets of sample on top of a silicon nitride chip. Illustrations are not to scale, but general feature dimensions are as indicated.

of forming gels.

Early SiN_x LCs were assembled with a free spacer between two chips sealed with resin or glue.[35–37] Ideally the spacer confers an exact thickness of liquid between the two windows.[24,35] However, sealant often invades the spacer region, making the size of the spacer non-reproducible.[35] Newer versions of liquid assemblies have employed melted indium spacers, but even these chips have nonuniform spacers and require further epoxy sealing.[38] Reproducible, uniform spacers are imperative to creating liquid cells that are reliable and provide reproducible data.

Another downside to this type of sealing is the trapping of air in the liquid cell.[35] Vaporisation of water in biological samples can negatively impact the buffer systems or environment the samples are viewed in (see chapter 6). Thus it is imperative to seal cells without any internal air, which was previously only possible in liquid flow holders (not in drop-cast systems).[34]

Sealing of liquid cells under atmospheric pressure causes the windows to bulge in the vacuum pressure in the electron microscope.[1,24,27,39] Bulging of windows creates thick liquid layers in the centre of the viewing area and limits the high-resolution viewing area to the window edges.[1,24,27,39] The bulging of window membranes is one of the major limitations of SiN_x liquid cells.[40] The other limitation has been the thickness of SiN_x membranes, which reduces the transmission of electrons and reduces image quality.[30] Both of these issues work in combination, if the thickness of SiN_x is decreased to improve transmission, the bulging of the membranes increases, reducing the transmission.[40] SiN_x windows tend to be > 30 nm thick (each), resulting in less transmission and lower resolution in comparison with

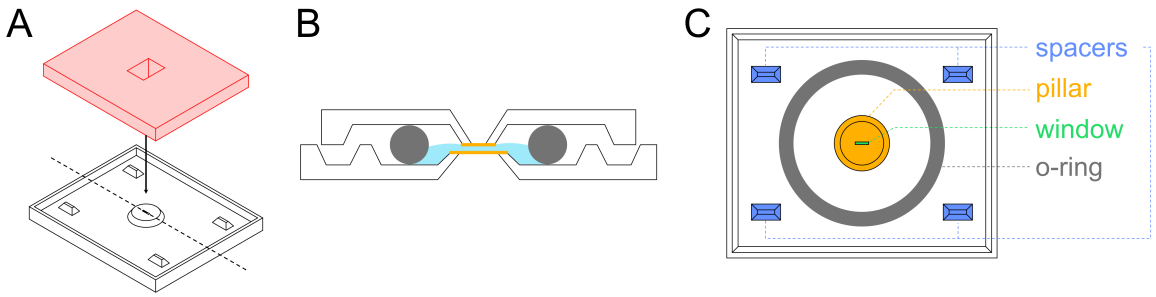


Figure 1.2: UeIL SiN_x liquid cells. Panel A shows the layout for the assembly of the LC made up of a top and bottom chip, the dashed line indicates the cross-section shown in panel B. Panel C shows the features and labels for the liquid cells: 4 spacers at each corner, 1 pillar in the centre, an o-ring around the area of the pillar, and a window in the centre of the pillar.

carbon-based LCs.[30,38]

Advances in standard SiN_x LCs made by myself and other members of the Ultrafast Electron Imaging Lab (UeIL), have allowed for minimal bulging and thin windows that yield homogenous, high-resolution data.[1] Bulging is minimized by sealing chips together under a vacuum environment, where evaporation of the sample droplet is prevented by saturating the chamber and pump (a gas syringe) with water vapour.[1] Chips are sealed with an internal o-ring, which provides uniform compression, delineated by spacers fabricated into the edges of the silicon chips (Figure 1.2C). The pillar containing the window (Figure 1.2C) is raised from the level of the o-ring to provide an area for the overflow of the liquid droplet, which is around 400 nL in volume.[1] We characterised the bulging of window membranes 30 nm thick, where bulging was found to be negligible with spacers of sizes 550 nm and 630 nm, and minimal (30 nm and 70 nm of bulging) for 100 nm and 180 nm spacers.[1]

1.5.3 Microwells

One other type of SiN_x-based cells is microwells, which are similar to regular SiN_x cells, except the spacer is determined by the height of the wells (Figure 1.1C). The wells are filled by placing a droplet on the wells, which are filled through capillary action.[30] During assembly, there is a risk that the liquid overflows the lid spacer region, and microwells are filled non-uniformly.[22] Though bulging is minimised across the area of the microwells, the SiN_x substrate must be sufficiently thick to support the microwell contents, where the thinnest reported layer is 30 nm.[22,41]

1.5.4 Hybrid cells

The final type of LC is hybrid cells, a combination of SiN_x and carbon-based cells.[23] A SiN_x cell is used as the base, and a carbon film (amorphous carbon or graphene) is used to envelop the sample.[23] Hybrid cells suffer from the same vulnerabilities as carbon-based cells, with some added durability from the SiN_x membrane. Hybrid cells also have reduced transmission, depending on the thickness of the SiN_x layer.[30]

LCs play key roles in the success and quality of LPEM experiments, evidenced through the broad range of cells and techniques researchers have tried to develop. In summary, robustness, reduced bulging, reproducibility, and electron transmission are the main properties of LCs that must be considered when performing LPEM.

1.6 Challenges for LPEM study of biomolecules

LPEM study of biomolecules is of high interest due to the ability to gain dynamic and structural information.[23] The major hurdles in LPEM research have been addressed by myself and other members of the UeIL. SiN_x LCs, more robust than carbon-based LCs have been developed, conferring bulgeless, uniform liquid layers that allow for reproducible sample imaging.[1] Though this was a huge step in LPEM research, SiN_x chips still require 30 nm of SiN_x material, reducing transmission compared to carbon-based LCs. In addition, a broad issue in electron microscopy of biomolecules is sample damage caused during imaging.

Material transmission

Thicker SiN_x material in LC membranes results in a loss of transmission and resolution.[30] Current commercially available thicknesses of LC SiN_x membranes are 50 nm each for microwells and regular chip formats.[41,42] Recent research has enabled the development of 30 nm SiN_x windows,[1] however reducing the thickness further would ideally allow SiN_x LCs to confer the resolution possible with carbon-based LCs.

The use of a freestanding 10 nm SiN_x membrane has recently been reported in an atmospheric-pressure system designed for scanning electron microscopy analysis.[43] In this system, there is no contact between the liquid and SiN_x membrane, thus the membrane bulging does not affect the liquid layer thickness.[43] Though this design is innovative, there is no possibility for transmission through the apparatus, and thus could not be used for TEM. Another report of 10 nm SiN_x LCs used the typical format, but two chips were bonded together, and filled by capillary action.[44] The authors did not discuss window

bulging in this paper which, as discussed, reduces the effective imaging area in LCs sealed under atmospheric pressure.[14,39]

There is a desire for SiN_x windows of even smaller thicknesses, down to 5 nm, as this can further improve the resolution of the samples being imaged. I performed theoretical calculations to study the relationship between material thickness and transmission (chapter 3), and developed a nanofabrication technique to generate 5 nm SiN_x windows (chapter 4). I then characterised these thin window LCs (chapter 5).

Sample irradiation

The other major hurdle in LPEM study of biomolecules is beam-induced sample damage.[24] There are two types of sample damage caused by electrons.[45] Elastic scattering causes displacement damage primarily in conducting samples such as metals, whereas inelastic scattering causes ionisation damage (radiolysis) which affects insulating materials, such as biomolecules.[45] The nature of inelastic scattering is that it results in a larger energy transfer, thus performing more damage to the specimen than elastic scattering.[46]

Radiolysis is the major concern with biomolecule samples, as the rapid deterioration of samples causes a loss of function and alteration of structure over time.[22,24] In addition, radiolysis causes high-resolution data to be lost first when samples are damaged.[22] Thus mitigating dose is imperative to structural measurements. New techniques are in development to quantify dose-related damage to biomolecules, as well as ways to reduce damage.[47] I investigated electron dose and inpainting techniques *in silico* (chapter 8) on biological data I acquired using the latest LC technology (chapter 6).

These challenges represent the next steps in furthering biological research with LPEM. However, LPEM research of biomolecules will still be limited by the ability to isolate pure and concentrated samples to view molecules of interest. In addition, it is still unknown how small volumes of liquid affect the activity of biomolecules.[48] Nevertheless, LPEM is poised to make a massive impact on biomolecule study, and tackling the challenges of transmission and sample damage aims to take on the main barriers in this field.

Chapter 2

Methods

In this chapter, the details of all experiments performed are explained.

2.1 Fabrication of thin liquid cell windows

2.1.1 Measurement of etch rates for Al_2O_3, TiO_2, and HfO_2

Etch rates shown in Figure 4.3 were determined after cleaning 2×2 cm silicon wafer pieces with piranha solution, then depositing ∼ 20 nm of each material (Al_2O_3, TiO_2, and HfO_2) onto each piece with atomic layer deposition (ALD). Pieces were annealed under the following conditions with 30-second ramp times.

Before etching, the thickness of the films was measured with ellipsometry (three scan points each). Then an annealed and not annealed piece of each film was exposed to

Film	Temperature (°C)	Gas	Time (seconds)
Al_2O_3	1100	N_2	90
TiO_2	500	N_2	240
HfO_2	600	N_2	240

Table 2.1: Annealing conditions for Al_2O_3, TiO_2, and HfO_2 thin films. The stress response of Al_2O_3 to annealing is shown in Figure 4.4, and the effect of annealing on etch rates for Al_2O_3, TiO_2, and HfO_2 is shown in Figure 4.3.

each of the etch conditions shown in Table 2.2, corresponding to the labels in Figure 4.3. The pieces were subsequently rinsed, dried, and their thicknesses were measured again with ellipsometry. The ellipsometer used was the Woollam M-2000, Model DI, from J.A. Woollam Co., using the completeEASE software. The rapid thermal processor used for annealing was the AccuThermo AW 610 from Allwin21 Corp.

Name	Chemical	Temperature (°C)	Time
BHF(1:10)	Buffered hydrogen fluoride, 1:10 dilution	25	10 min
HF (0.5)	Hydrogen fluoride, 0.5%	25	10 min
KOH (45%)	45%	70	3 hr
Piranha 2:1	concentrated sulfuric acid : 30% hydrogen peroxide, 2:1	25	15 min
RCA 1	water : 27% ammonium hydroxide : 30% hydrogen peroxide, 5:1:1	70	15 min
RCA 2	water : 27% hydrogen chloride : 30% hydrogen peroxide, 6:1:1	70	15 min

Table 2.2: Etching conditions for Al_2O_3, TiO_2, and HfO_2 thin films. Etch rate data for these conditions is shown in Figure 4.3.

2.1.2 Measurement of stress for Al_2O_3

Interferometry measurements to determine stress were performed on full 4-inch silicon wafers, where initial measurements were taken after an initial piranha clean, and final measurements were taken after ALD deposition (described herein), and each subsequent

anneal. The annealing was performed as stated previously, with the times and temperatures indicated in Figure 4.4. The interferometer used was the FLX-2320-R by TOHO Technology. Thicknesses required to measure the stress were measured with ellipsometry (with 5-point scans), as described previously.

2.2 Microscopy methods

Microscopy data was obtained at the Canadian Center for Electron Microscopy (CCEM), using the Spectra Ultra, and Talos 200 TEM microscopes (ThermoFisher Scientific, Waltham, MA). Both microscopes are equipped with Extreme-Brightness Cold Field Emission Guns. The Spectra employs a Ceta S CMOS camera, and the Talos uses a Ceta M CMOS camera. Images shown in this thesis were taken in CTEM mode. EELS spectra were obtained with Gatan imaging filter (GIF) systems, where the Spectra is equipped with a GIF Continuum HR camera, and the Talos is equipped with a GIF Continuum S camera. Images were acquired with the Velox software, and EELS spectra with the Gatan Digital Micrograph software.

Unless otherwise specified, EELS measurements in the Spectra used a collection semi-angle of 53.4 mrad and a convergence semi-angle of 28.0 mrad, at 300 keV. Spectra imaging was performed at 300 keV, and Talos imaging was performed at 200 keV.

2.3 Characterisation of thin nanofluidic cells

2.3.1 EELS measurement of transmission data

To measure transmission data in dry LC windows (Figure 5.5), the Spectra Ultra TEM was used to acquire 2D EELS scans. Each EELS scan was averaged across 2600 points of 4 × 4 nm area, with 0.05 eV resolution. Dispersion, magnification, step size, camera length (480 mm), slit width, entrance aperture size, and detectors were kept constant across each experiment. The collection semi-angle and convergence semi-angle were kept constant in the measurements at each acceleration voltage but varied slightly between measurements at different voltages. In addition, each scan was taken in an area that had not been scanned previously except to acquire an image, to keep the contribution from carbon contamination low.

2.3.2 AFM characterisation of thin windows

atomic force microscopy (AFM) was performed in the Quantum-Nano Fabrication and Characterization Facility (QNFCF) using the Bruker Dimension FastScan (Billerica, MA). The Bruker ScanAsyst-Air AFM probe was used in ScanAsyst mode. Optical microscopy was performed on the Olympus Canada model MX-61A in the QNFCF.

2.3.3 Liquid cell assemblies for experiments showing liquid layer thickness

Liquid cell assemblies for 5 nm membranes shown in Figure 5.7 had the configurations shown in Table 2.3.

Assembly	Top chip version	Bottom chip version	Window thickness (nm)	Spacer target (nm)
A	v09	v09	10	200
B	v09	v09	10	200
C	v07	v07	10	200
D	v07	v07	10	200

Table 2.3: LC assembly configurations for 5nm membranes shown in Figure 5.7 The chip styles correspond to the versions in Figure 5.8. The spacer targets may not reflect the liquid layer thicknesses in these assemblies, the true liquid layer thicknesses can be seen in Figure 5.7.

2.3.4 Liquid cell assembly

Loading of liquid samples into the SiN_x LCs was performed as follows. Nanofluidic chips were first cleaned with H_2/Ne/Ar plasma at 30 Watts for 2 minutes using the Gatan Solarus Model 950 Advanced Plasma System. First, a large chip is attached with carbon tape to the holder interior, with a small hole made in the carbon tape to prevent trapping of air between the tape and the chip. The loading station is prepared with ~0.1 mL of water in the reservoir, and two screws placed on the drivers. The lid is then fit into the pins above the screws. An external o-ring is placed centrally in the lid, followed by a small chip, and an internal o-ring is placed about the central pillar on the small chip. The sample is dispensed (normally 400 nL) using a micropipette onto the pillar, and the loading station

is sealed by lowering the piston, inserting the holder, and placing the lid on the assembly. A metal stopper is placed on the piston stage (to stop the piston from lifting when the vacuum is formed), and the inlet valve is sealed.

Next, a gas syringe is filled with water such that the syringe is at the zero mark, but there is no air or bubbles in the line or syringe. The syringe is connected to the inlet valve, sucked to the 60mL mark, and the value is slowly opened. This evacuation process under water vapour pressure is performed three times, and the final pressure in the chamber is the vapour pressure of water (20 Torr).[1] Finally, the metal stopper is removed and the piston is slowly released carefully so that the pins align with the holder. The screws are inserted with the drivers, then the valve is opened and the piston is lowered before the holder is removed. The carbon tape is removed and the holder is held to the light to ensure the alignment of the chips is correct (a small light should be visible where the windows of the two chips overlap). The screws are checked for tightness, and then the holder is ready to be inserted into the microscope. Further detail of the assembly can be found in Lott et al..[1]

2.4 LPEM biomolecule imaging

Images showing apoferritin (Figure 6.2), vesicles (Figure 6.4), and salt from bacterial cell culture media (Figure 6.6) were acquired in the Spectra Ultra TEM. Images showing ferritin (Figure 6.3), pAAV (Figure 6.5), and adeno-associated virus (AAV) (Figure 6.1), were acquired with the Talos 200 TEM. Apoferritin (#A3660) was purchased from Millipore sigma (Burlington, MA). AAV and pAAV (pAAV-CAG-GFP, #37825) were purchased

from addGene (Watertown, MA), where the virus was #37825-PHPeB (titer $\geq 1 \times 10^{13}$ vg/mL) and the plasmid was #37825-Vdna. nanoXact monodisperse Au nanorods (40 nm $\times$ 15 nm with sodium citrate capping agent at 1 optical density unit) were purchased from nanoComposix Inc. (San Diego, CA).

The culture of *Pelagibacter communis* was provided by Professor Stephen Giovannoni and Dr. Chih-Ping Lee at the Department of Microbiology, Oregon State University. Cultures were maintained through subculture in artificial seawater media, and storage conditions described elsewhere.[49] Flow cytometry was used to measure cell counts, using an ImageStream X Mark II Imaging Flow Cytometer, with excitation at 488nm, in the lab of Professor Brian Ingalls at the University of Waterloo. Cells were stained with SYBR Green dye for $\sim$ 50 minutes before quantification, SYBR Green I Nucleic Acid Gel Stain (#S7563) was purchased from ThermoFisher Scientific (Waltham, MA). Cell density was monitored every $\sim$ 14 days in order to keep cells in their viable cell density range (1×10^4 - 1×10^8 cells/mL). Culture flasks were purchased from Thomas Scientific (Swedesboro, NJ), Erlenmeyer polycarbonate flasks with duo caps (#1139G29) were used to prevent nutrient absorption and allow sufficient air exchange with 50 mL of culture.

LC assembly conditions for the images shown in chapter 6 are described in Table 2.4. Assembly was performed as described herein.

Sample	Top chip version	Bottom chip version	Window thickness (nm)	Spacer target (nm)
apoferritin / vesicles	v07	v07	15	200
Pc culture (salt)	v07	v09	30	100
pAAV	v08	v07	25	50
AAV	v09	v09	25	200

Table 2.4: LC assembly configurations for biomolecule data in Figures 6.1 of AAV, 6.2 of apoferritin, 6.4 of vesicles, 6.5 of plasmid DNA, and 6.6 of salt crystals. The chip styles correspond to the versions in Figure 5.8. The spacer targets may not reflect the liquid layer thicknesses in these assemblies, they only reflect the nominal thickness from fabrication techniques.

2.5 Inpainting

Images taken of biomolecules were converted from EMD to PNG format through the use of the Napari EMD plugin or using similar code from the independent software I developed. These images were masked using random or spiral constant linear velocity (CLV) masks with the software developed for inpainting. These defected images were then inpainted with the Telea fast marching method[50] implemented in the OpenCV[51] software package, and Biharmonic formula inpainting[52] implemented in the Scikit-Image[53] software package.

Output images were maintained in lossless PNG formats, and the root mean squared error (RMSE) and pearson correlation coefficient (r) formulas (equations 8.4 and 8.5 in chapter 8) were used to calculate the difference between the original (unmasked) images, and the inpainting result images. When spiral masks were compared, the original and inpainted images were masked such that the circle bounded by the image dimensions was the only data being compared. The same was also performed for images with random masks to generate the data where spiral and random mask inpainting results are compared, shown in Figure 8.5.

Chapter 3

Theoretical electron transmission through materials

Modelling the transmission of electrons through different materials is useful to predict image quality gained from LCs. More transmission will result in clearer signals and higher-quality images.[30] Predicting the relative contributions of water, sample, and window material in LCs also allows for informed optimisation of LPEM technology development.

The transmission of electrons can be modelled by accounting for inelastic and elastic scattering processes. Elastically scattered electrons appear at high scattering angles, and inelastically scattered electrons appear at small scattering angles.[13] The amount of electron scattering is calculated as a function of the angle from the central origin (the collection angle). These measurements can be used to produce a total scattering cross-section value, unique to each element.[54]

Theoretical calculations described elsewhere were used to generate total elastic cross-section data for selected elements.[54] Briefly, the calculations employ the partial-wave expanded Dirac equation to solve the motion of a scattered electron through a static potential field of the atomic charge density modelled by the Poisson equation.[54] I used these total elastic scattering cross-sections to estimate the transmission of electrons through different compounds.

3.1 Calculation of transmission

Electron transmission is calculated using theoretically calculated total elastic scattering cross-section (σ_{tot}) data.[54] The scattering cross-section is dependent on the material the electrons traverse, and the scattering cross-sections of compounds can be estimated from the stoichiometric sum of different elements where the cross-section of individual elements is known.[30]

The following relation is used to estimate inelastic scattering cross-section σ_{inel} data which occurs at small scattering angles.[30]

$$\sigma_{tot} = \sigma_{inel} + \sigma_{el} \tag{3.1}$$

$$\sigma_{inel} = \frac{18\sigma_{el}}{Z} \tag{3.2}$$

$$\sigma_{tot} = \frac{18\sigma_{el}}{Z} + \sigma_{el} \tag{3.3}$$

Where σ_{tot} is the total scattering cross-section, σ_{inel} is the inelastic scattering cross-

section, σ_{el} is the elastic scattering cross-section, and Z is the atomic number of the element.

We then calculate the total mean free path (Λ_{tot}), using the number densities of each element in the compound of interest.

$$\Lambda_{tot} = \frac{1}{\sum N_j \sigma_{tot,j}} \tag{3.4}$$

$$N = \frac{N_A \rho}{M} \tag{3.5}$$

Where N_j is the number density of element j, $\sigma_{tot,j}$ is the total scattering cross-section of element j, N_A is Avogadro's number, ρ is the density of the material, and M is the molecular weight.

To calculate the Λ_{tot} of a compound, it is more convenient to write the problem the following way, where σ_{tot} should be weighted by the molecular contribution (here X,Y):

$$\Lambda_{tot} = \frac{1}{\sum N_{compound}(X\sigma_{tot,element1} + Y\sigma_{tot,element2} + ...)} \tag{3.6}$$

For example for Si_3N_4:

$$\Lambda_{tot} = \frac{1}{N_{Si3N4}(3\sigma_{tot,Si} + 4\sigma_{tot,N})} = \frac{1}{\frac{N_A \rho_{Si3N4}}{M_{Si3N4}}(3\sigma_{tot,Si} + 4\sigma_{tot,N})} \tag{3.7}$$

It is convenient to use formula 3.7 such that there is no confusion about which densities and molecular weights are appropriate.

To convert the Λ_{tot} to % transmission (T), the thickness (t) must be known.

$$T = e^{-t/\Lambda_{tot}} \tag{3.8}$$

I developed a Python program to perform these calculations for a range of materials where electron scattering cross-section data is provided. The program interpolates/extrapolates Λ_{tot} values using a logarithmic fit to estimate transmission at any electron acceleration voltage, though this estimation will be most accurate below 300 keV (closer to the range of provided data).[54] All the user must provide is material density, a dictionary with the elements in a compound and their stoichiometric ratio, and optionally the molecular weight. The option to provide a molecular weight is useful, as electron scattering cross-section data is missing for some elements, thus the nearest element can be chosen in the dictionary (i.e. Helium as an upper estimate for Hydrogen).

The software is publicly available at https://github.com/UeIL-Waterloo/Electron_transmission.

3.2 Liquid cell calculations

The path of the electron includes both the window material, the water, and the sample. The signal from the sample is competing with the loss of transmission by the water and LC material, thus is it useful to understand what liquid layer thickness, material thickness, and material composition are optimal for retrieving a strong signal from the sample. The calculations above were used to estimate total electron transmission through window materials

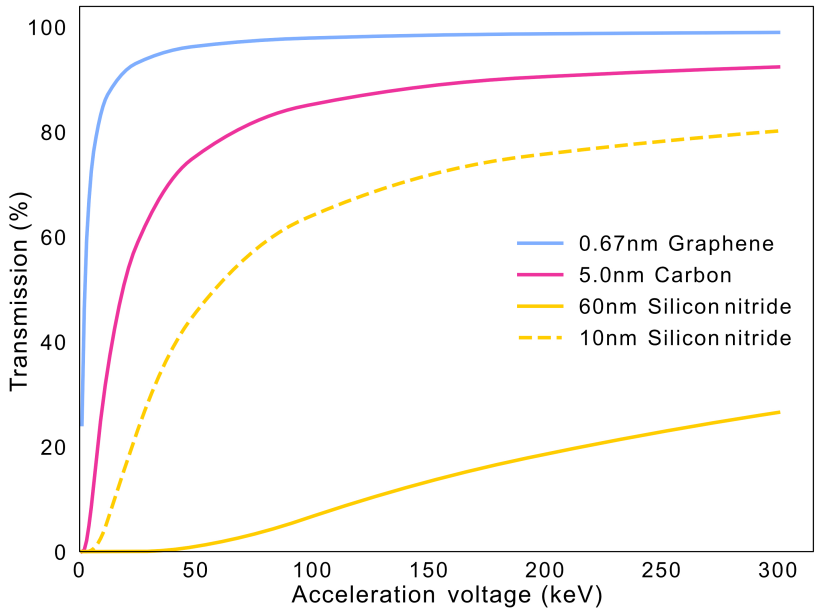


Figure 3.1: Theoretical transmission through LC materials. The transmission of total (inelastic and elastic) electrons through LC materials graphene, amorphous carbon, and SiN_x 10 nm, and 60 nm thick (5nm and 30 nm individual window thickness respectively). Calculations are performed with total scattering data obtained by Riley et al. and fit with an exponential function are shown across nominal acceleration voltages. This figure can be reproduced using the code available at https://github.com/UeIL-Waterloo/Electron_transmission

for different liquid cells: graphene, amorphous carbon, and SiN_x at different thicknesses (Figure 3.1). Figure 3.1 shows that the thinner SiN_x windows begin to approach the transmission achieved by carbon LCs. This data provides motivation for the development of thin SiN_x windows, with the ultimate goal of achieving higher-resolution images with SiN_x LCs.

Though water is lighter than SiN_x, its contribution to scattering is large due to the thick layers often needed for the hydration of liquid samples. The relative contributions

of water and different LC materials to loss of transmission can be clearly seen in the Λ_{tot} values of these compounds, shown in Figure 3.2. At high acceleration voltages, the Λ_{tot} of water is three times the Λ_{tot} of SiN_x at 300 keV.[1] The relationship between Λ_{tot} and transmission depend on the thickness, but we can see that the amount of water equivalent to 10 nm SiN_x is approximately 39 nm, as shown in Figure 3.3. Thus, when imaging samples are suspended in thick liquid layers (i.e. 200 nm), the thickness of the LC membrane contributes little to the overall loss in transmission. However, when the goal is to observe small structures of viruses and proteins ($<$ 30 nm), the thickness of the window material is a large determining factor in the resolution gained. Thus thin windows are imperative to gathering high-resolution structures of viruses and proteins using SiN_x LCs.

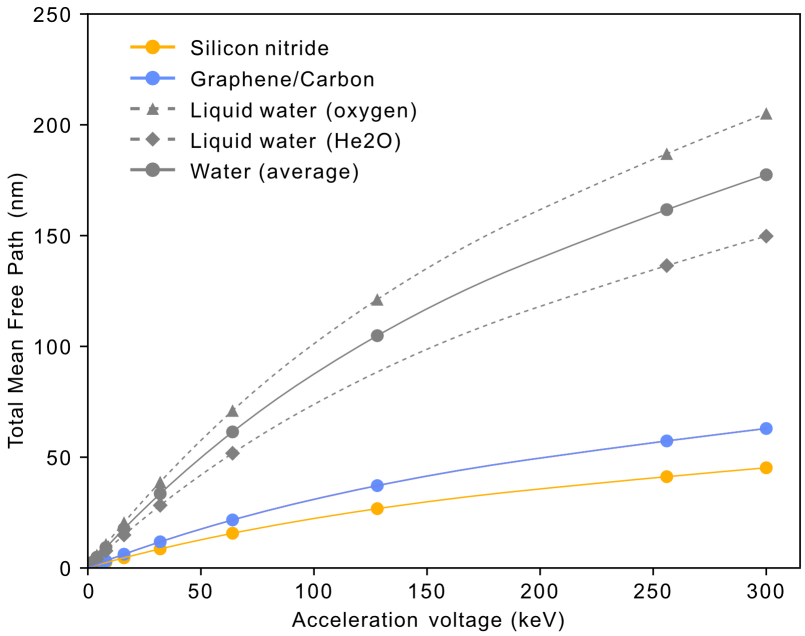


Figure 3.2: Theoretical total mean free paths of LC compounds. The Λ_{tot} of water (estimated by averaging Λ_{tot} of He_2O and O, also shown), SiN_x, and carbon are shown as a function of nominal acceleration voltage. Calculations were performed with total scattering data obtained by Riley et al. This figure can be reproduced using the code available at https://github.com/UeIL-Waterloo/Electron_transmission

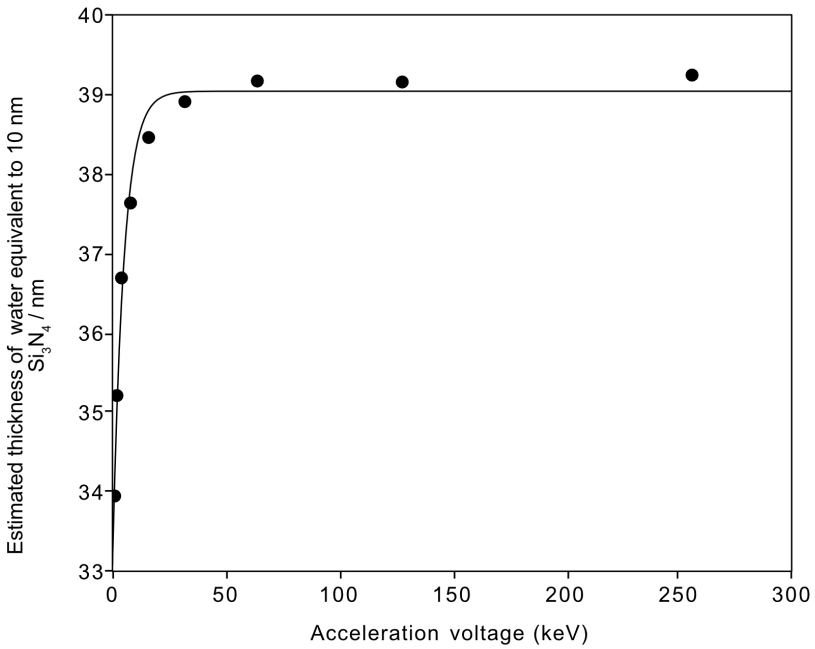


Figure 3.3: Thickness of water equivalent with transmission equivalent to 10 nm SiN_x**.** The plot shows an exponential fit with the equation $y = 39.0(1 - e^{-0.20x-1.88})$ above the calculated data points. Calculations were performed with total scattering data obtained by Riley et al. This figure can be reproduced using the code available at https://github.com/UeIL-Waterloo/Electron_transmission

Chapter 4

Fabrication of thin liquid cell windows

Modelling of electron transmission in chapter 3 showed that thin windows of SiN_x can be used to gain higher transmission. The fabrication of thin windows will improve the resolution of data obtained, especially for biomolecules as they have low contrast. This chapter outlines the journey of the fabrication of 5 nm thin windows.

4.1 Nanofluidic cell design

Critical parts in the design of LCs include spacer regions, window areas, handling regions, and the method of enclosure. The LCs designed in the UeIL at the University of Waterloo employ variations of the design shown in Figure 4.1. The spacer and window areas are

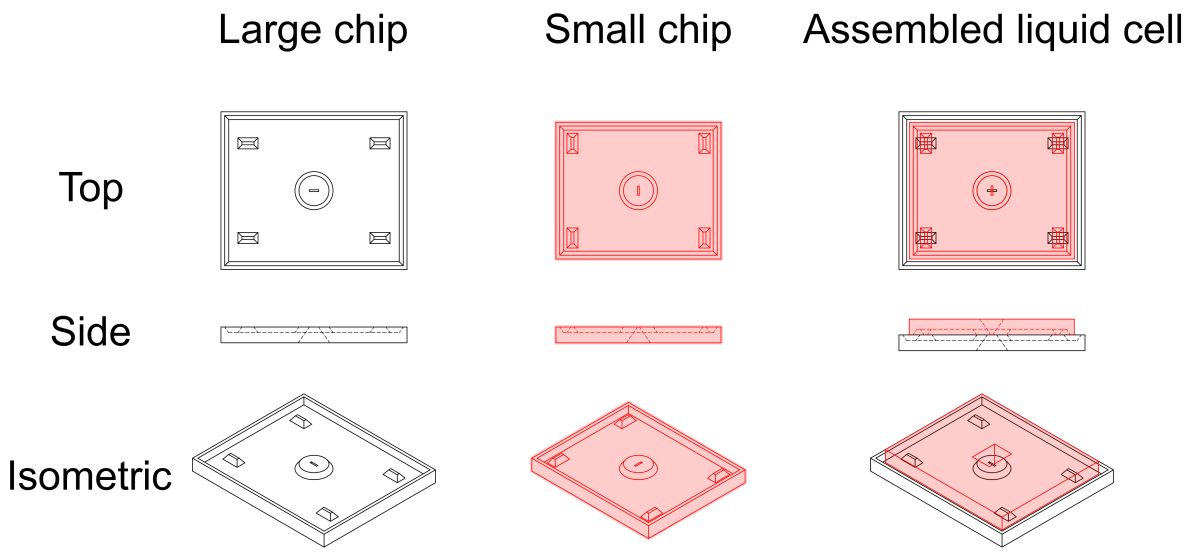


Figure 4.1: Dimensions of the nanofluidic cell chips and assembly. The top, side, and isometric views of each chip are shown, with the small chip shown in red. More design configurations are shown in Figure 5.8.

highlighted in Figure 1.2, where the window is placed on a pillar separate from the spacers such that the liquid sample will not invade the spacer region. The chip is handled at the edges, such that any damage done through handling will not deform or contaminate the spacer or window regions. An o-ring is employed for uniform sealing, placed about the pillar such that when two chips come together (Figure 4.1), the sample region is hermetically sealed. Details of fabrication techniques used to fabricate SiN_x LCs with generic designs are shown elsewhere.[38]

In general, nanofluidic chips are fabricated using photolithography (Appendix A), deposition, and etching techniques, using a silicon wafer substrate. The key steps in this process involve creating the pocket for the o-ring, the pillar and spacers, and finally, the release of

the windows. Window release refers to the process by which the bulk silicon substrate is etched until the SiN_x film is reached through the substrate, creating the freestanding film. The technique used for window release is important to the creation of thin films because the specificity of the silicon etch process determines if the film will be preserved throughout this process.

4.2 Window release methods

Window release refers to the action of etching a patterned silicon wafer, in a way that results in the formation of a freestanding thin film, or window. Potassium hydroxide (KOH) etches silicon at a rate of approximately 0.35 µm/min at 72°C, thus it takes approximately 24 hours to etch a standard 500µm silicon wafer. Reactive ion etching (RIE) etches silicon at a rate of approximately 1 µm/min, thus would only take 8.3 hours, but the cost for machine time is much higher for RIE than the cost for KOH etching. Thus the selectivity of KOH towards all exposed materials must be accounted for during the etching process.

The process of forming a window is outlined in Figure 4.2A, where the purple layer makes up the window material. In order to etch a specific area to define the window size, a mask (black) is patterned using photolithography techniques (see Appendix A). In order to make the windows thin, a thin layer can be deposited, or a thick layer can be deposited and later etched to the desired thickness. This depends on the film material chosen, and what deposition techniques are available for the material. Deposition of the thin film before window release requires an etch process that does not also target the window material.

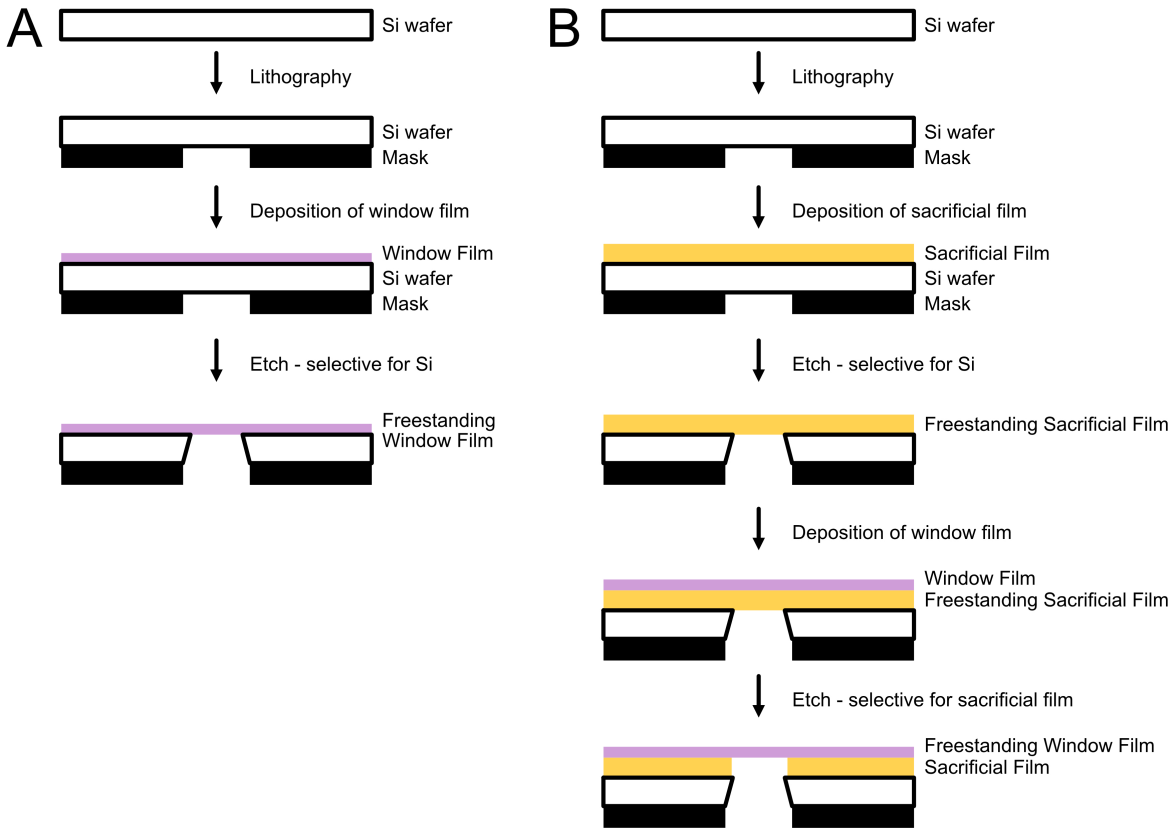


Figure 4.2: Cross sections of wafers showing thin window fabrication processes. Panel A shows a general scheme for the formation of a window film (purple) on a silicon wafer (white box) with a mask (black) defining the window dimensions. The mask is deposited via lithography techniques, the window film material is deposited on the wafer, and the silicon wafer is etched in the area defined by the mask. In panel B another general scheme is shown for the formation of a window film, where a sacrificial film (yellow) is deposited before the silicon etch, and removed after deposition of the window film.

If the window release process that also etches the film material is chosen, then a sacrificial film (orange) can be employed (Figure 4.2B). Here the sacrificial film is deposited, the silicon is etched to create a freestanding sacrificial film, and then the window film is deposited. The second etch releases the window material from the sacrificial film. This method allows for more flexibility in the choice of etch method based on considerations of the sacrificial and window films. Any etch method that targets the sacrificial film but not the window material is appropriate, since the bulk silicon is sufficiently thick that any etching of the silicon is generally not a concern. Each of these techniques is an appropriate approach for fabricating thin windows in theory. In practice, epitaxy, the etch reaction process, and material tensile strength, all contribute to the ability of a material to form a thin freestanding film.

4.3 Materials exploration

SiN_x has been a standard material for LCs developed with nanofabrication methods. However, other materials may offer higher transmission and conductivity. Different materials can change the hydrophobicity of LCs, changing the way samples are deposited on the chip. Other materials can also open doors for the functionalization of window membranes with different compounds. Thus other thin film materials were explored as candidates for the fabrication of LC windows.

Al_2O_3, TiO_2, and HfO_2 materials were available for ALD deposition in the QNFCF, thus their chemistry was explored to determine the selectivity of different fabrication steps. HF and buffered HF (BHF) were used as it is known to etch SiN_x thus is a technique used

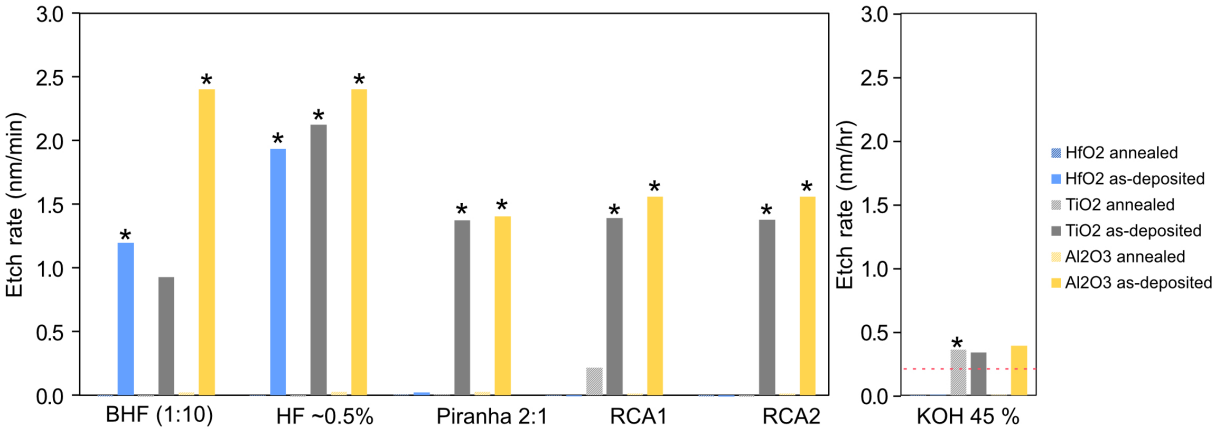


Figure 4.3: Etch rates of Al_2O_3, TiO_2, and HfO_2 films in standard nanofabrication wet process steps. Etch rates were measured in the conditions described on the x-axis, with full details provided in Table 2.2. All etch rates marked with a '*' indicate measurements where the etch rate is an underestimate because the film was less than 10 nm after the etch was performed (where ellipsometry measurements become less accurate). Annealing was performed as described in Table 2.1. The pink dotted line across the KOH etch data indicates the etch rate of SiN_x (0.21 nm/hr).

in some feature fabrication steps. KOH was tested as it is used in window release, and Piranha and RCA1/2 were tested as they are commonly used to clean the wafer before other process steps. Figure 4.3 shows the results of these etch tests, where etch rates were determined by measuring film thickness with ellipsometry before and after etching (chapter 2.1). Films were also tested after annealing in a rapid thermal processor (RTP), as this is known to improve the resistance of materials to etching.[55]

Focusing on the results of KOH etching, HfO_2 and Al_2O_3 after annealing were deemed good candidates for window material, as their etch rates were negligible and thus could withstand the silicon bulk etch (any value below the etch rate of SiN_x, 0.21nm/hr was deemed suitable). HfO_2 was removed as a candidate at this point, because the transmission

through HfO_2 was deemed to be poor due to the high weight of Hafnium. Focusing on annealed Al_2O_3, the practicality of forming a freestanding film was analysed.

SiN_x is deposited with low-pressure chemical vapour deposition (LPCVD), coating both sides of a double-side polished wafer, thus providing convenient dual use of SiN_x as a mask base on one side and window on the other side. ALD deposition occurs on one side which is unfavourable, as placing films flat onto a stage surface for deposition often causes scratches. Thus if Al_2O_3 was deposited via ALD on both sides of the wafer, there would either be damage to the mask or window material. Normally when scratching is an issue, a photoresist can be used to protect the bottom surface of the wafer, but photoresists are a major source of contamination, thus this technique cannot be used in deposition or annealing equipment. In addition, the RTP is only configured to anneal a single surface, not dual-surface films, and also would introduce scratches to the wafer.

In addition, it has been shown previously that annealing increases the stress of Al_2O_3 films.[56] This arises from the shrinking of the films, and an increase in crystallinity of the Al_2O_3 films.[56] To determine how annealing impacts thin Al_2O_3 layers, stress measurements were performed using interferometry to give insight into the film properties. Films were annealed at 900°C and 1000°C for 60, 300, and 600 seconds, in nitrogen gas environments. Though Al_2O_3 etching experiments were performed at 1100°C, the rapid thermal processor cannot be held at 1100°C for an extended time. The results shown in Figure 4.4 show that there is an initial jump in stress after annealing for 30 s, and extended annealing yields a decrease in stress after prolonged heating with a limited return after $\sim$ 10 min. The experiment also showed that there was high non-uniformity in film stress across the wafers after annealing (seen by the large error bars), which is not advantageous to chip

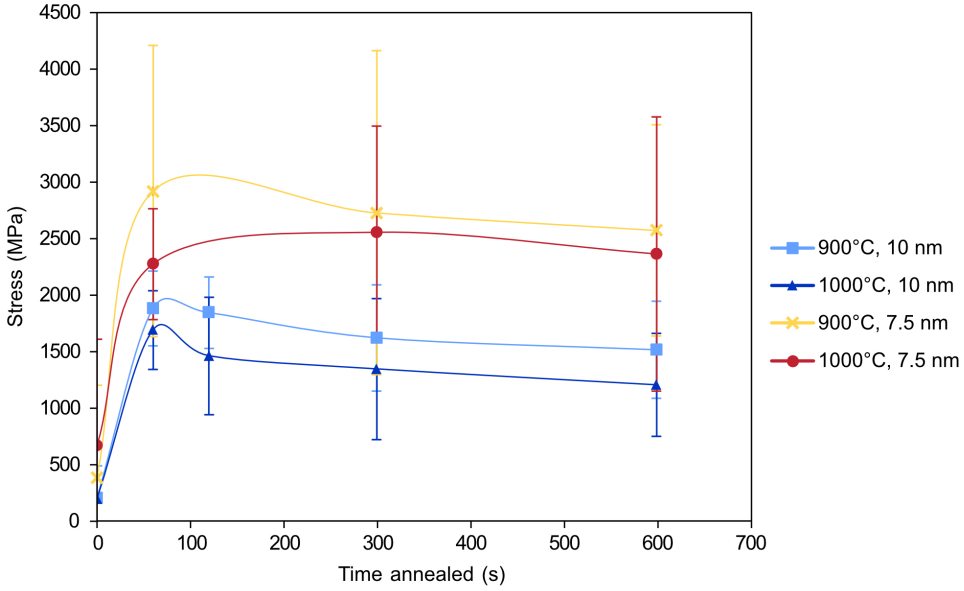


Figure 4.4: Stress measurements of thin Al_2O_3 films. Measurements of Al_2O_3 films were taken before and after ALD deposition of 7.5 nm and 10 nm film thicknesses (time annealed = 0), then after annealing (rapid thermal processing) at 900°C and 1000°C for 60, 300, and 600 seconds, in nitrogen gas. Error bars show the deviation in stress measurements across the wafer surface. These measurements are outlined in chapter 2.1.

manufacturing. In addition, it appears that thinner material is under more stress and that thinner material underwent a larger increase in stress and non-uniformity after annealing.

With procedural optimisation in mind, I investigated the use of SiN_x as a sacrificial film for thin not-annealed Al_2O_3 (Figure 4.2B). This technique provides SiN_x as a mask material, removes the need to anneal the Al_2O_3 film to withstand etching, and provides a different base for the growth of the Al_2O_3 film. Sacrificial thick layers of SiN_x were released from bulk silicon, followed by deposition of Al_2O_3 and no annealing, then HF was used to etch the SiN_x below the Al_2O_3 windows. In this technique, the thickness of the Al_2O_3 and

SiN_x layers are balanced such that etching in HF causes a thin Al_2O_3 layer should remain. This experiment was tested on two wafers, with the final result that 60% of the windows released were intact, and the remaining windows were broken. Such low yield makes Al_2O_3 a poor candidate for LC windows, but another method was developed during this time to create thin SiN_x windows.

The final method used to produce thin SiN_x windows cannot be detailed in this thesis as it is a proprietary method. Further questions regarding this topic should be addressed to Professor German Sciaini. The validation of the fabrication of thin, 5 nm, SiN_x windows is detailed in chapter 5.

Chapter 5

Characterisation of thin nanofluidic cells

The thickness of SiN_x in the nanofluidic cells that constitute LC assemblies is measured throughout the nanofabrication process via ellipsometry. However, measurements of film thickness through ellipsometry can cause wafers to be damaged by handling and scratching on machine stage surfaces. Fewer measurements are taken in the final LC fabrication process to retain high yields of chips from each wafer. Thus the final window thickness must be quantified after the chips have been diced and packaged. The window dimensions are too small for transmission ellipsometry and have no underlying film for regular reflection ellipsometry. Thus to measure window thickness, transmission can be quantified through EELS measurements.

5.1 Thickness determination with EELS

Similar to the calculations performed in chapter 3, a material's inelastic mean free path (λ_{inel}) can be estimated and used to determine the thickness of substrates using EELS.[57–59] Once the λ_{inel} of SiN_x is known, equation 5.1 can be used to estimate the thickness of SiN_x.

Equation 3.8 is similarly shown as the EELS log-ratio model in equation 5.1.[13]

$$\frac{t}{\lambda_{inel}} = ln\left(\frac{I_t}{I_0}\right) \tag{5.1}$$

Where t is the thickness of the material, I_t is the total area under the EELS spectrum, and I_0 is the area under the zero loss peak (ZLP).

The λ_{inel} of material can be estimated by the Malis equations shown in 5.2-5.4.[58]

$$\lambda_{inel} = \frac{106FE_0}{E_m ln\left(2E_0\beta/E_m\right)} \tag{5.2}$$

$$F = \frac{1+\frac{E}{1022}}{1+\left(\frac{E}{511}\right)^2} \tag{5.3}$$

$$E_m = 7.6Z_{eff}^{0.36} \tag{5.4}$$

Where the effective atomic number (Z_{eff}) can be estimated with the Lens model in equation 5.5.[1,58,60]

$$Z_{eff} = \frac{\sum_i f_i Z_i^{1.3}}{\sum_i f_i Z_i^{0.3}} \tag{5.5}$$

Or the λ_{inel} of material can be estimated by the Iakoubovskii equations 5.6&5.7.[57]

$$\lambda_{inel} = \frac{\frac{200FE_0}{11\rho^{0.3}}}{ln\left(\frac{1+\frac{\beta^2}{\theta_E^2}}{1+\frac{\beta^2}{\theta_C^2}}\right)} \tag{5.6}$$

$$\theta_E = 5.5\frac{\rho^{0.3}}{FE_0} \tag{5.7}$$

Where F is given in equation 5.3.

When water is present, equation 5.8 can be used to remove the contribution from a SiN_x membrane of known thickness, in order to visualise the water thickness across the EELS scan.[1]

$$\frac{t_{total}}{\lambda_{total}} = \frac{t_w}{\lambda_w} + \frac{t_{SiNx}}{\lambda_{SiNx}} \tag{5.8}$$

5.2 EElS thickness characterisation

EELS was performed on two dry 5 nm windows assembled with no internal o-ring. This was demonstrated to show that independent of a liquid sample or internal pressure, the 5 nm windows are freestanding with no visible deformations and can withstand electron

beam doses under regular imaging conditions. This EELS measurement is shown in Figure 5.1 where the t/λ was found to be 0.07.

The convergence angle of this measurement was 53.4 mrad, with acceleration voltage (E_0) of 300 keV, SiN_x density (ρ) of 3.2 gcm^3,[61] and a saturation factor (θ_C) of 20 mrad.[13,57] The resulting calculations using each method gave λ_{inel} of SiN_x:

$\lambda_{SiNx} = 123.4$ (Malis et al.[58])

$\lambda_{SiNx} = 167.5$ (Iakoubovskii et al.[57])

The resulting thicknesses of SiN_x are:

$t_{SiNx} = 8.6$ nm (Malis et al.[58])

$t_{SiNx} = 11.7$ nm (Iakoubovskii et al.[57])

Thus the thickness of the two-chip assembly is taken as an average, 10 nm, with each window being approximately 5 nm. These chips were found to have no cracks or deformations and did not degrade over the imaging time. Despite these encouraging results, the error of EELS thickness measurements is roughly 20%.[58] Thus further characterisation was performed with AFM to confirm these findings.

AFM measurements

To further characterise the thickness of the 5 nm windows, windows were broken on two chips using a profilometer probe and the partially severed material was measured with AFM. The AFM measurements yielded very exact measurements of the window material thickness, shown in Figure 5.2. The data show two selected areas with a difference in height

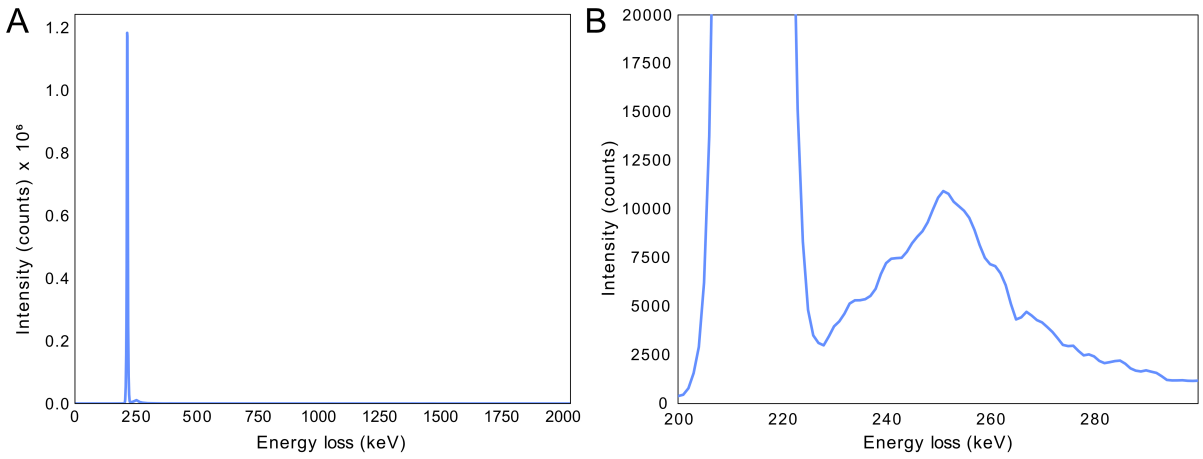


Figure 5.1: EELS spectra of a dry 5 nm SiN_x liquid cell assembly. Panel A shows the full EELS spectrum for two 5 nm SiN_x windows (V07 nanofluidic cells as shown in Figure 5.8) sealed without an internal o-ring (10 nm SiN_x total). Panel B shows the same spectrum on an enlarged scale showing the core loss peak.

(between the severed SiN_x window and the silicon chip) of 5 nm. The results confirmed that thin SiN_x LCs were fabricated successfully, thus the next step in characterisation was to quantify the improved transmission gained in the manufacture of these thin windows.

During this experiment, I discovered that the AFM probe, unlike the profilometry probe, was able to measure the window area without breaking it. A scan across a 5 nm SiN_x window is shown in Figure 5.3, where panel C shows the deformation of the window by the probe. The scan images in panels A and B also showed an interesting finding, that the window was being probed in a way that excited waves that could be measured across the surface of the window (ScanAsyst mode AFM was used, which functions similarly to regular tapping AFM). In Figure 5.4, the window is scanned at different angles, showing that the waves induced by probe tapping are physical, with movement perpendicular to

the shortest window dimension. Because the waves disappear when scanned perpendicular to the shortest window dimension (Figure 5.4A), we cannot attribute the pattern seen to laser interference. This intriguing result opens the door to a new method for future work in thin film characterisation.

Transmission measurements

To experimentally investigate the impact of SiN_x window thickness on electron transmission, I performed a series of EELS experiments to show the transmission relative to the window thickness. These experiments were performed in the absence of liquid, for 5, 10, 17, and 60 nm at 60, 120, and 300 kV.

The data show the area of the ZLP relative to the total area (I_t/I_0), which is a measure of the transmission of inelastic electrons. A higher I_t/I_0 value of 1 would indicate that no electrons interact inelastically with the sample (only a ZLP peak), and 0 would indicate no transmission. The data show the expected trend that the inelastic transmission decreases as the substrate becomes thicker. Thus we can assume (equation 3.3) that total transmission also decreases as the substrate becomes thicker. The experimental data shows that thicker SiN_x (60 nm and 15 nm) is more transmissive than predicted by theoretical calculations but thinner SiN_x (5 nm) is less transmissive than expected. The theoretical and experimental data have a high agreement with 10 nm SiN_x at high acceleration voltages.

The higher-than-expected transmission for 60 nm SiN_x is intriguing and leads to the question if the transmission of thick liquid layers is also better than predicted. Though this would be a very useful study, there is no current way to estimate liquid layers in LCs

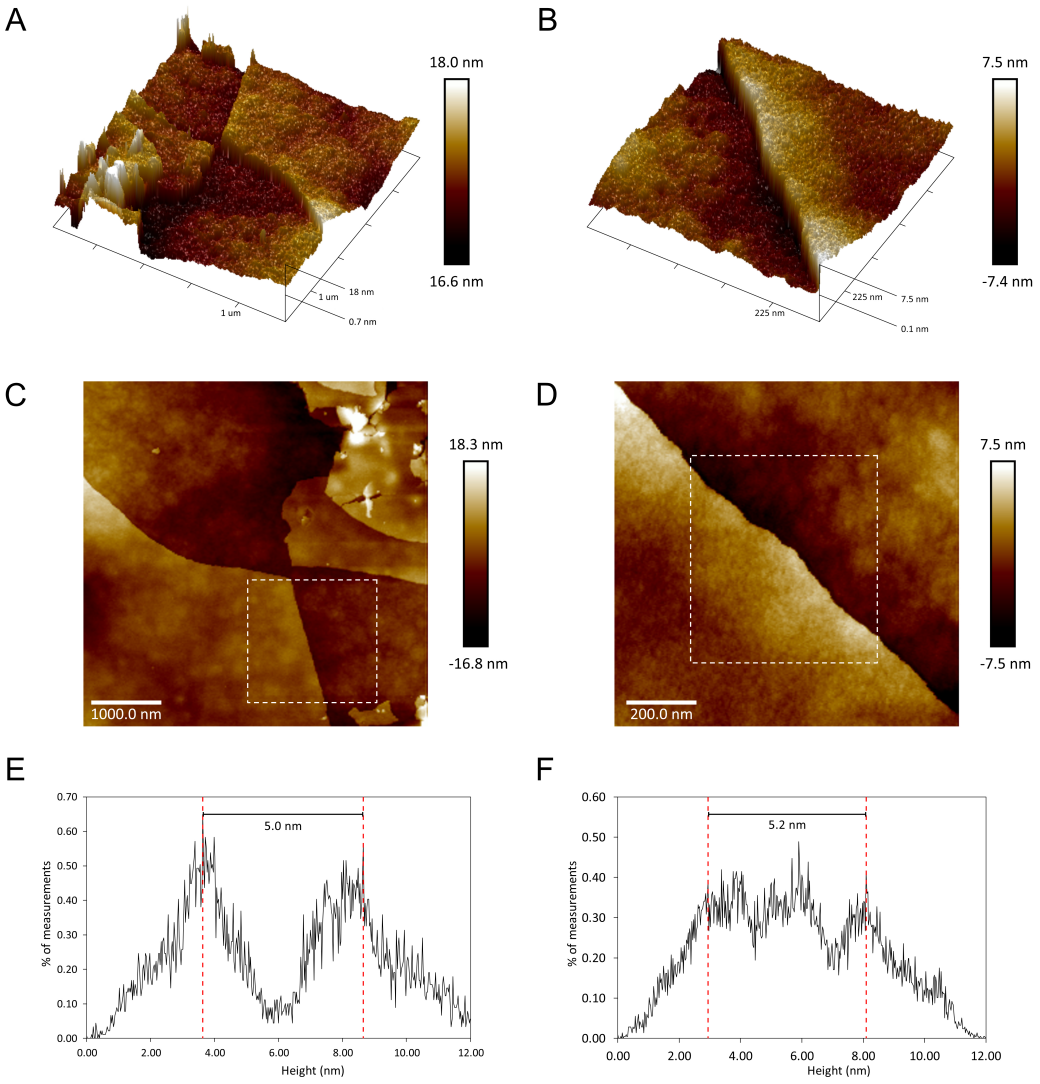


Figure 5.2: AFM measurements of broken 5 nm LCs. Panels A and B show 3D maps of the AFM measurements, where the scale provides dimensions. All colour maps show the height of each point measured. 2D images for the same scans are shown in panels C and D respectively. Panels E and F show histograms for the height measurements from the areas shown in the dashed white boxes in panels C and D respectively. The red lines in panels E and F show the most populated height measurements across the areas with and without a 5 nm window, where the difference in the two populations shows height differences of approximately 5 nm.

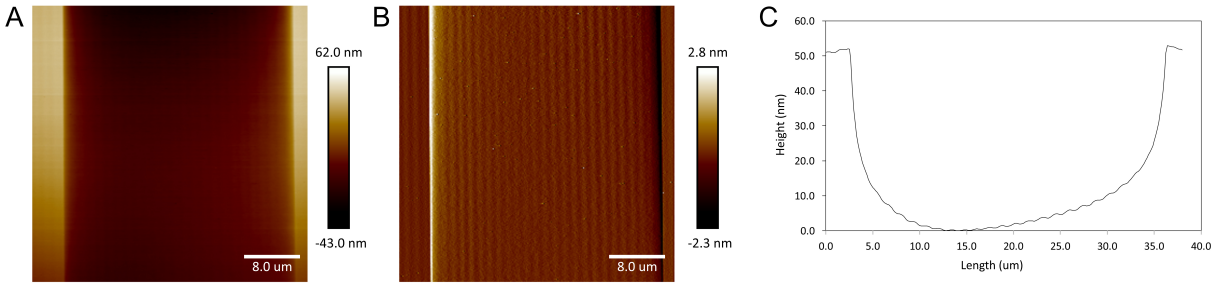


Figure 5.3: AFM measurements of intact 5 nm LCs. Panel A shows the height information for the scan across the window, and panel B shows the peak deflection error for the same contact measurement. The colour bars show the height information. Panel C shows an average height profile across the length of the window, showing the deformation of the 5 nm window caused by the force of the AFM probe.

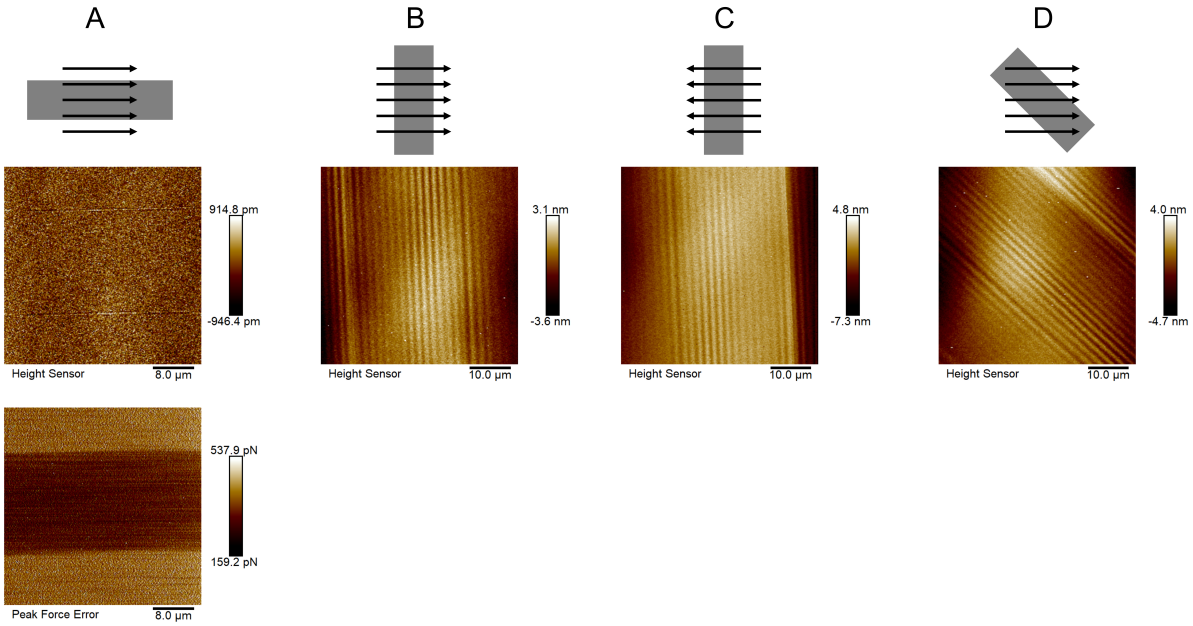


Figure 5.4: AFM scans across 5 nm freestanding SiN_x windows at different angles. Panels A-C show the scan as directed in the graphic on the top of the image(s), where the top images show the height diagram, and the lower image in panel A shows the phase profile. Scale bars are indicated on each image.

other than estimation through EELS itself. It is also unknown if elastic electrons would follow the same trend, and similarly, if equation 3.3 is a valid approximation for thicker materials.

The key takeaway of this analysis is that 5 nm SiN_x windows transmit 89% of electrons at 200 keV, and 91% at 300 keV, relative to inelastically scattered electrons. Though these numbers do not reflect total transmission, the data confirms that 5 nm windows allows more transmission of electrons. Following these results, I investigated the impact that transmission has on image resolution.

Resolution measurements

The goal of more transmissive window substrates is improved resolution during imaging. To show that thinner SiN_x windows confer higher resolution data I performed the following experiment. The TEM was aligned as optimally as possible at 300 keV, and then a series of dry gold nanorod samples with 5, 15, and 60 nm SiN_x total were prepared. Each assembly was loaded into the microscope and images were taken while trying to achieve the highest resolution possible (more details are outlined in chapter 2.3). Figure 5.6 shows the highest resolution images obtained with each assembly. The microscope used was the Spectra Ultra at CCEM, which has a limit of 0.5 Å resolution at 300 keV (ThermoFisher Scientific, Waltham, MA).

This experiment is subject to error, as beam stigmation, nanoparticle density, window charging, drift, and other factors can all contribute to variation in resolution. Thus this data should be taken as qualitative, as the best demonstration possible using experimental

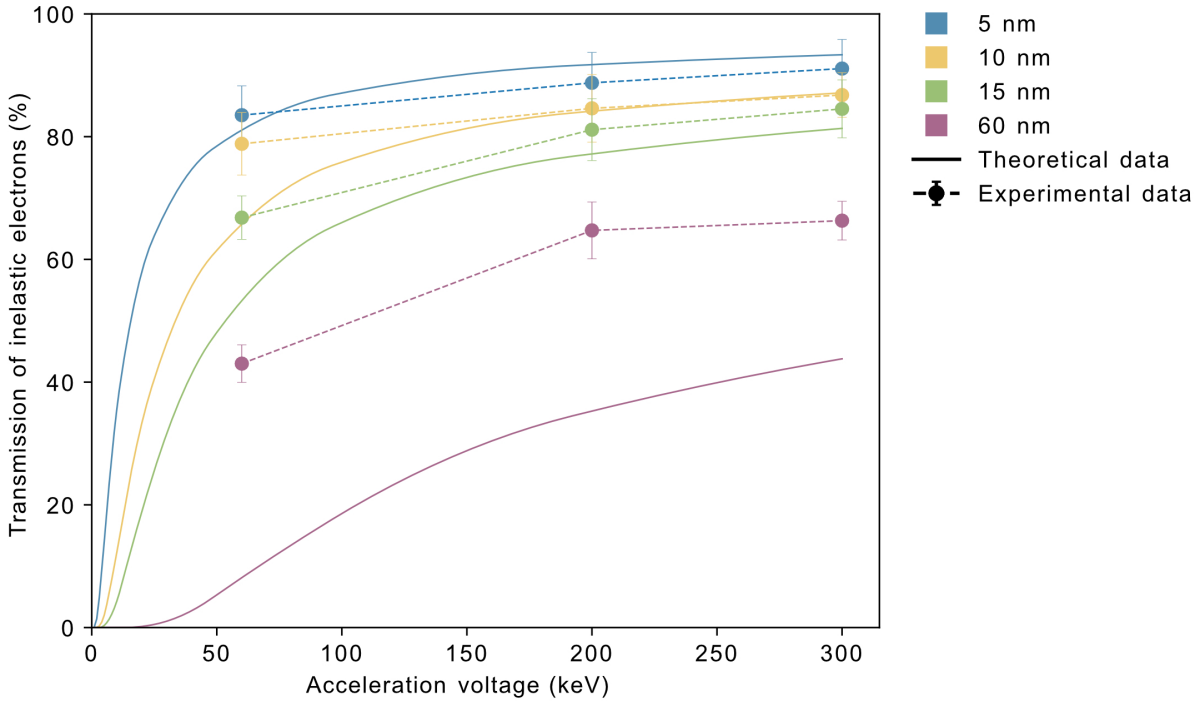


Figure 5.5: Theoretical and experimental transmission of inelastic electrons through SiN_x. Calculations of theoretical transmission of inelastic electrons was performed as described in chapter 3, but the total inelastic scattering cross chapter was used in place of the total scattering cross-section. The experimental transmissions shown by the points joined by dashed lines were measured in the Spectra Ultra microscope with EELS using dry nanofluidic cells (chapter 2.3).

techniques to show resolution with different substrate thicknesses.

Though the results were not linear, the 5 nm window clearly conferred the best resolution at 0.62 Å, which is close to the performance limit of the microscope. However, the 60 nm window also conferred very high resolution, at 0.78 Å. These results exemplify the very small differences in resolution that we hope to gain from thin windows, which are already close to the maximum possible resolution. Imaging of biomolecules in chapter 6 showed high-resolution images despite thick liquid layers with thin SiN_x windows. It is apparent that the goal of improving transmission and resolution in LPEM with thinner windows is achieved with 5 nm SiN_x windows produced in this work.

5.3 Liquid cell characterisation

Though the usefulness of thin window membranes can be seen in increased signal transmission and improved resolution, the ability for 5 nm windows to withstand water containment without excessive bulging is key to using thin windows in LPEM. Assembly of two chips with 5 nm windows with liquid was successfully performed followed by EELS to quantify the liquid layer thickness. Results for four different successful assemblies are shown in Figure 5.7.

The EELS spectra clearly show that the liquid layer is much thicker than the expected $\sim$ 200 nm layer as the core loss peak is larger than the ZLP. One of the thinnest regions measured in sample B gave a t/lambda value of 5.53, putting the liquid layer thickness at approximately 640 nm. As previously discussed, there is a limit to thickness where imaging

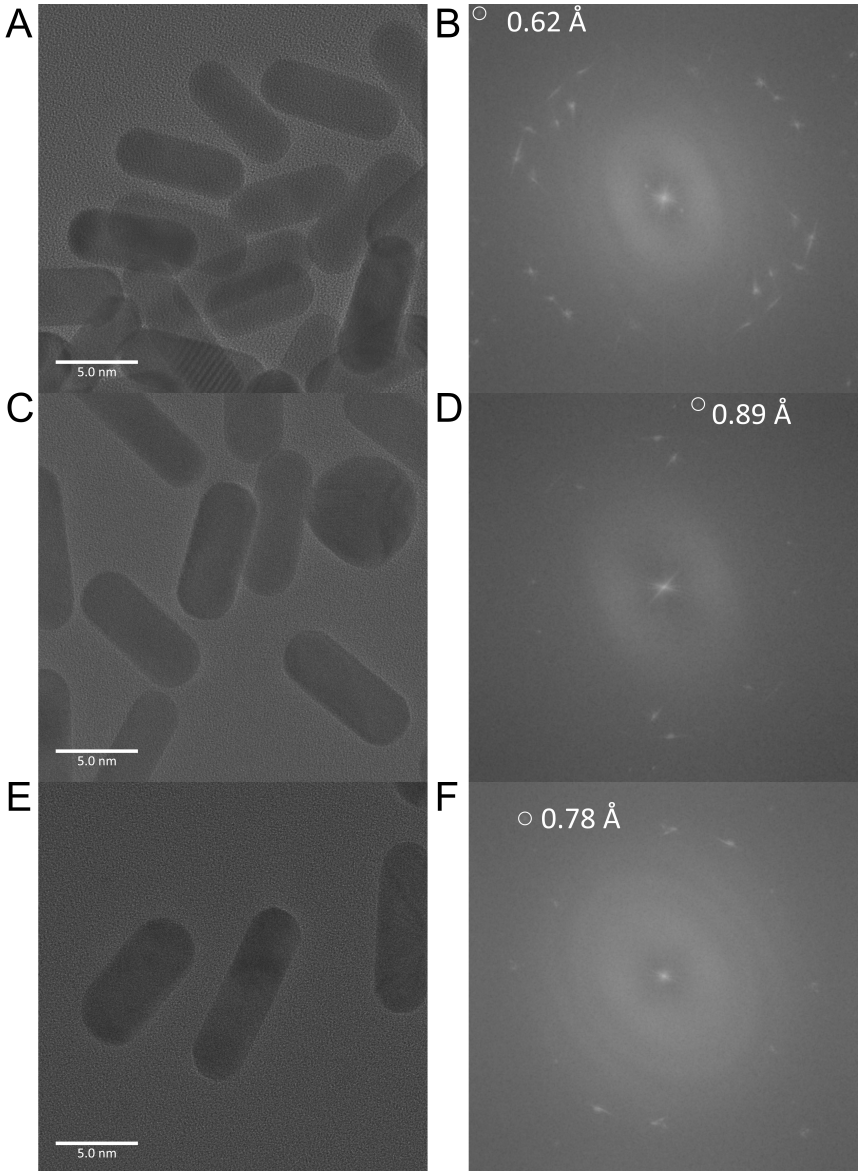


Figure 5.6: Images and FFTs of gold nanorods on dry 5, 15 and 60 nm SiN_x windows. Panels A, C, and E show the images with their scale bars, and panels B, C, and D show the corresponding FFTs where the resolution of the outermost signal is indicated. Image A corresponds to a 5 nm SiN_x window with 0.62 Å resolution, image B corresponds to a 15 nm SiN_x window with 0.89 Å resolution, and image E corresponds to a 60 nm SiN_x window with 0.78 Å resolution.

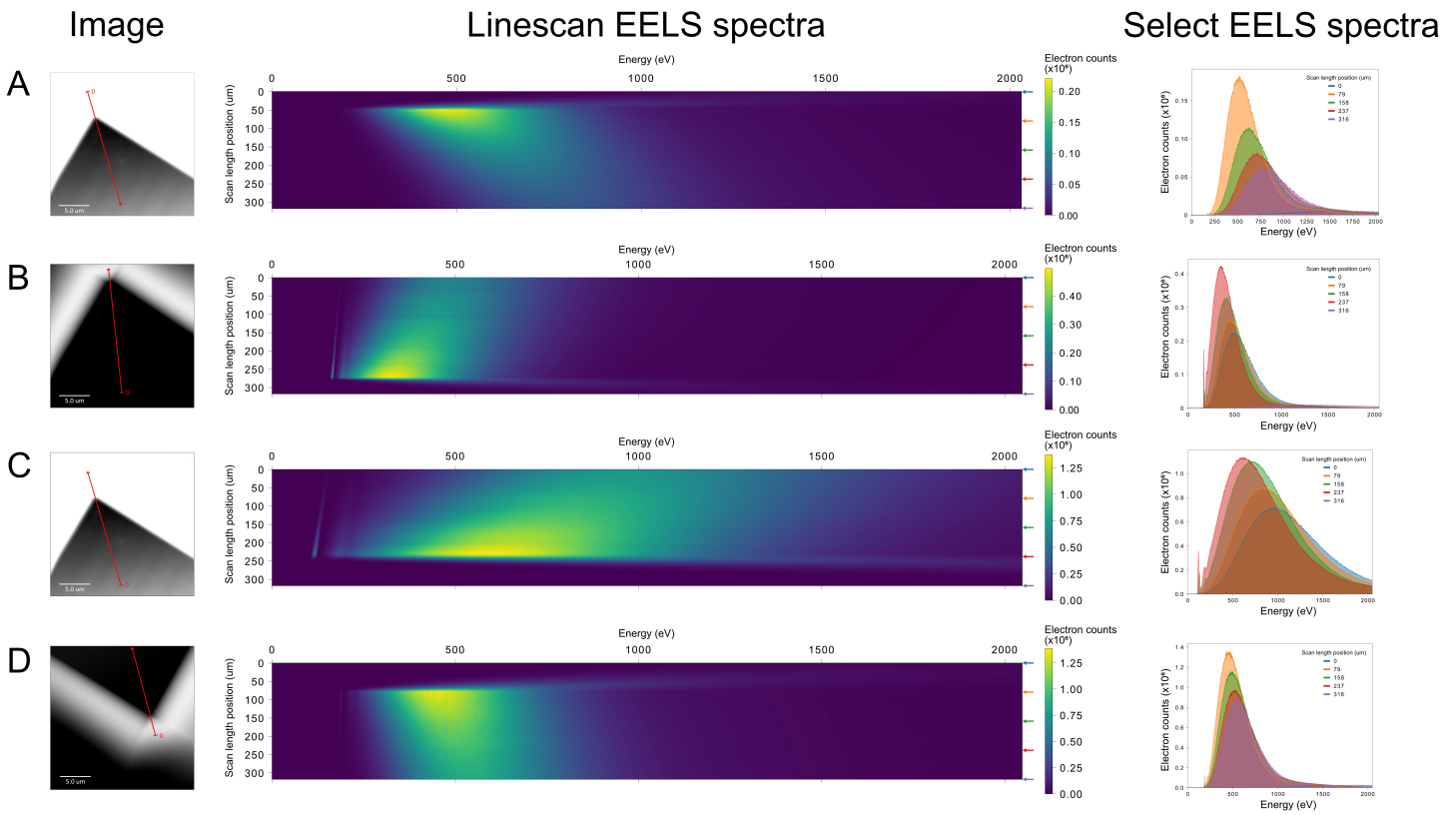


Figure 5.7: EELS line scan data of liquid assemblies made with two 5 nm membrane LCs. Scans A-D show data from four separate assemblies, where the configurations are given in chapter 2.3.4. The images show the window edges where the red lines indicate the location and direction of the scans. The linescan EELS spectra show the spectra as 2D heatmaps, where the x-axis is the position of the scan on the linescan, and the y-axis is energy. Select EELS spectra are shown on the far right, where the colour indicates the position matching the area selected from the 2D heatmap. Samples A and B were assembled with V09 chips and samples C and D were assembled with V07 chips, all assemblies had two 5 nm window chips with a total 200 nm spacer.

will provide useful information. With 570 nm of water, the transmission of electrons is reduced to 5% at 200 keV and 10% at 300 keV (using the average Λ_{tot} of water in Figure 3.2). Thus the assemblies shown in Figure 5.8 have water layers that are almost too thick to yield useful images.

Importantly, the spectra shown in Figure 5.8 are very thick even at the very edge of the window. This finding indicates that bulging was not an issue, thus there was an issue in the fabrication of the nanofluidic cells that caused the chips to bow in a manner that resulted in thicker water layers across the pillar area. In the initial experiments with thin windows, V07 LCs were used (Figure 5.8). The original chip design in Lott et al.[1] (Figure 5.8) was altered in the fabrication of new chips with thin windows. One alteration made was to make both the top and bottom chip pillars round, due to strange etch rates observed in the fabrication of the bottom Lott, 2023 chips. Thus it is likely that the large contact surface area between the top and bottom pillars in V07 caused the chips to produce thicker liquid layers than expected. The high contact area is also believed to have caused many of these LC assemblies to break.

The chips shown in Figure 5.8 labelled V08 and V09 were fabricated with the pillar contact area issue consideration. Initially, the new V08 and V09 chip assemblies were breaking, which was discovered to be caused by direct contact between the two pillars during assembly. This was deduced from optical microscopy of chips after TEM and disassembly of the chips, the window of the top chips is seen to be deposited onto the bottom chip (see Figure 5.9). This was likely because the lid of the new loading station was designed for thinner chips fabricated with 500 μm silicon wafers, the additional compression likely caused hard contact between the chips, causing top windows to snap onto the bottom

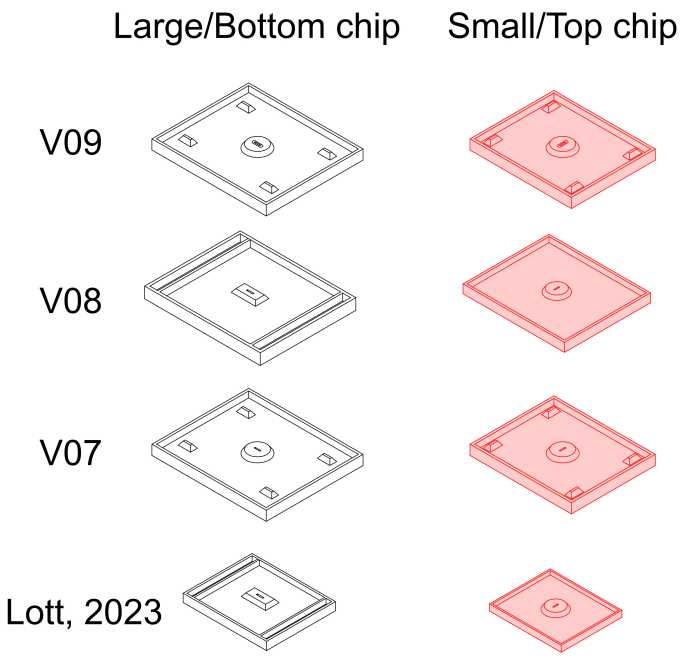


Figure 5.8: LC chip design versions. The leftmost column displays the bottom (or large) chips, which are assembled in the holder, while the rightmost column displays the top (or small) chips in red, which are assembled on the loading station piston. Each version of chips fabricated is labelled on the left, from Lott, 2023 depicting the chip style used in Lott et al..[1] V07 chips were fabricated with 500 μm silicon wafers, and all other chips were fabricated on 525 μm silicon wafers. The scale of these designs is not exact.

chips. Once the lid was corrected, the assemblies were successful without breaking, allowing for the acquisition of more liquid assembly data (Figure 5.7A&B), and some biological data (see chapter 6). The liquid layers achieved at this point were still very thick (Figure 5.7A&B), thus work that remains includes performing some corrections between the target and achieved spacer sizes before the LCs are fully functional with thin windows.

Though work still remains to retain the reproducible thin liquid layers achieved in

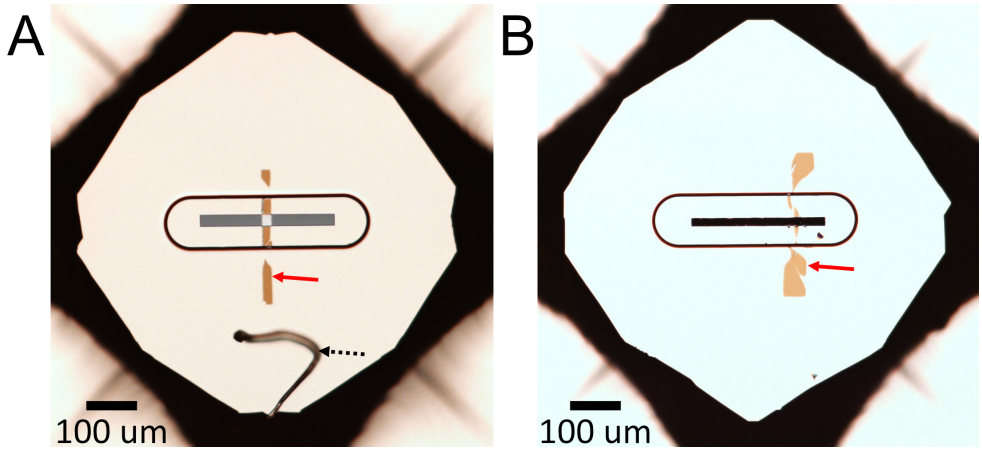


Figure 5.9: Two V09 chips after TEM, showing broken windows. Panels A and B show two different bottom nanofluidic chips after disassembly, where the window from the top chip (red arrows) is seen to be discharged onto the area of the bottom window. Some contamination (black dashed arrow) is also present from handling after disassembly.

previous chip versions,[4] the characterisation discussed in this chapter demonstrates the successful fabrication of 5 nm SiN_x windows. I successfully showed that 5 nm SiN_x windows confer higher transmission, comparable to carbon-based LCs. I also showed that 5 nm SiN_x windows yield high-resolution data when used as dry substrates, another possible use of the technology developed. I further showed that 5 nm SiN_x windows can contain thick liquid layers, though bulging remains to be characterised in thin LCs.

Chapter 6

LPEM biomolecule imaging

Though the silicon nitride liquid assemblies have until recently yielded thick liquid layers, I collected promising results showing biomolecules in the liquid phase. To study an array of biomolecules: viruses, proteins, vesicles, and DNA were all successfully imaged. An attempt to image live cells was made, and though unsuccessful, yielded some data of interest.

6.1 Adeno-associated virus

Ground-breaking results from Jonaid et al.[22] demonstrated structures of AAV reconstructed at 3.22 Å resolution from 3737 particle images. In this work, particles were imaged at 200 keV, with a DE-12 direct detector camera in approximately 52-105 nm liquid layers, using the microwell LC format with a total of 60 nm SiN_x.[22] In order to complement this work, AAV was imaged with a Ceta M CMOS camera at 200 keV using a total 25 nm SiN_x LC

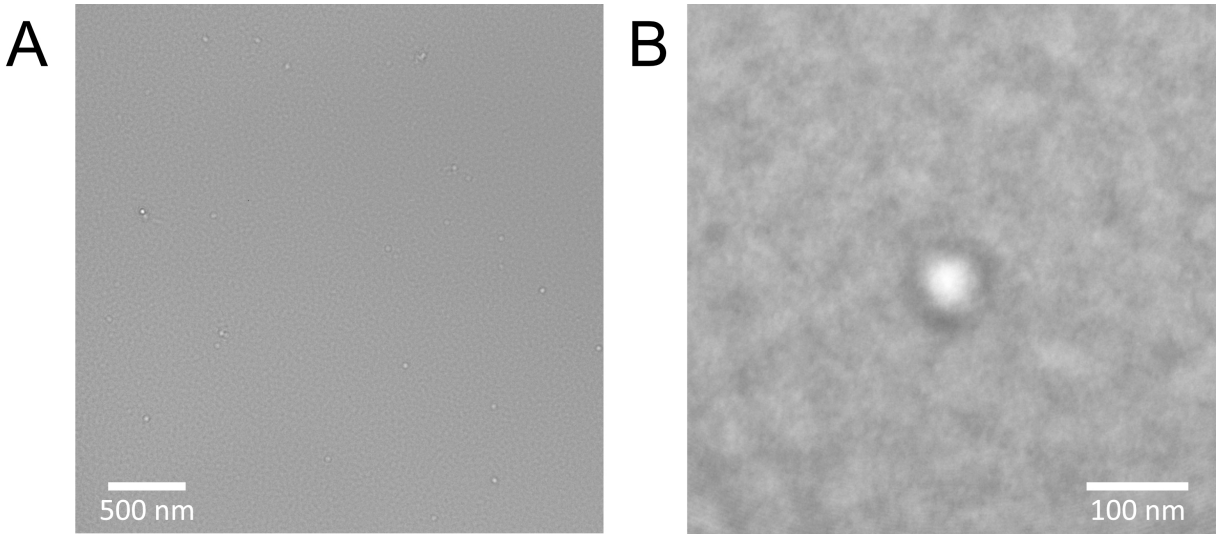


Figure 6.1: LPEM images of AAV. Panel A shows a lower-magnification view of multiple AAV particles, and panel B shows a higher magnification image of a single AAV particle taken from the same liquid cell assembly. Scale bars are indicated in each image. Assembly data can be found in Table 2.4.

with a target 200 nm spacer. Due to issues in the LC designs at this point (see chapter 5.3), the liquid layer was much thicker than expected. Analysis of EELS spectra obtained across two liquid window edges gave liquid layer thickness measurements of 602 nm of water at the window edge and 756 nm at the centre (calculations described in chapter 5.1). For comparison, AAV was imaged with a t/λ_{total} value of 0.7-1 in Jonaid et al.,[22] and the t/λ_{total} in Figure 6.1 is 4.1-5.1. The fact that the AAV particles are visible with decent resolution in Figure 6.1, where transmission is greatly reduced, and images were taken with a lower quality camera, suggests that once issues with liquid layer thicknesses are resolved, the LC technology developed in UeIL may rival these results.

6.2 Ferritin and apoferritin

Proteins are the foundation of many biological molecules' functions and are key to understanding biological systems. Ferritin is a 474 kDa protein, which is much larger than the average protein found in prokaryotes (30 kDa) and eukaryotes (40 kDa).[62] However, ferritin has been used abundantly in LPEM research as a standard to demonstrate the resolution of proteins.[63–65] Ferritin has a heavy iron core, which yields high contrast and makes observation with TEM easy compared to many smaller, lighter proteins.

Previous research by the UeIL group has demonstrated high contrast of ferritin in LCs with 60 nm total SiN_x taken with 200 keV electrons and a Ceta M CMOS camera (Figure 6.3, courtesy of Tyler Lott and Ariel Petruk). A pre-print article shows images of ferritin taken with 100 nm SiN_x layers using a K2 camera.[63] Comparison between the images shows comparable resolution. In Marchello et al.,[63] a 50-frame video of ferritin yielded over 5000 particle images, used to reconstruct a 4.74 Å density map of ferritin.

The next challenge in LPEM protein imaging is to visualise smaller proteins without metal centres. Apoferritin, which is ferritin without an iron core, is presented as an ideal candidate for demonstrating the resolution of metal-free proteins. I aquired images of apoferritin, shown in Figure 6.2. These images were taken at 300 keV with a Ceta S CMOS camera, with 15 nm total SiN_x layers, and V07 chips with a 200 nm spacer target. Surprisingly, the resolution of apoferritin in Figure 6.2 shows the protein structure: a core of $\sim$ 8 nm diameter and a shell of $\sim$ 12 nm diameter.[63] Images of ferritin clearly show more contrast due to the iron core, but the ability to view $\sim$ 12 nm proteins without heavy elements is exciting for the development of LPEM. Reconstruction of apoferritin images

is a key area suggested for future work in this area. In addition, the exploration of the resolution of smaller proteins with LPEM is an area of great interest.

6.3 Vesicles

The apoferritin sample previously described was prepared using a proprietary method, modified based on published literature. Based on the literature, the method employed is likely differential centrifugation.[66,67] The sample is thus not expected to be free of other cellular material.[68] During the LPEM experiment for the apoferritin sample, what is strongly believed to be vesicles, were seen in the sample (Figure 6.4). The samples degraded on the same timescale as liposomes imaged in previous experiments,[1] and showed a visible membrane bilayer of $\sim$ 5 nm.[68] Vesicles are abundant in equine spleen, as are multi-vesicular complexes.[69] However, it is also possible that these vesicles are microsomes (vesicle-like particles formed from disruption of the endoplasmic reticulum) which are often formed during homogenization of eukaryote cells.[68] Where vesicles are typically 20-150 nm (though can be larger), microsomes are typically 20-200 nm.[68] Figure 6.4 shows images of these vesicles, and their degradation over $\sim$ 2 minutes of imaging.

6.4 Plasmid DNA

Another key biomolecule I analysed is DNA (Figure 6.5). This is the first time DNA has been observed with LPEM experiments. I chose plasmid DNA as I was interested in observing the supercoiled structure. Figure 6.5 shows clearly the supercoiled structure of

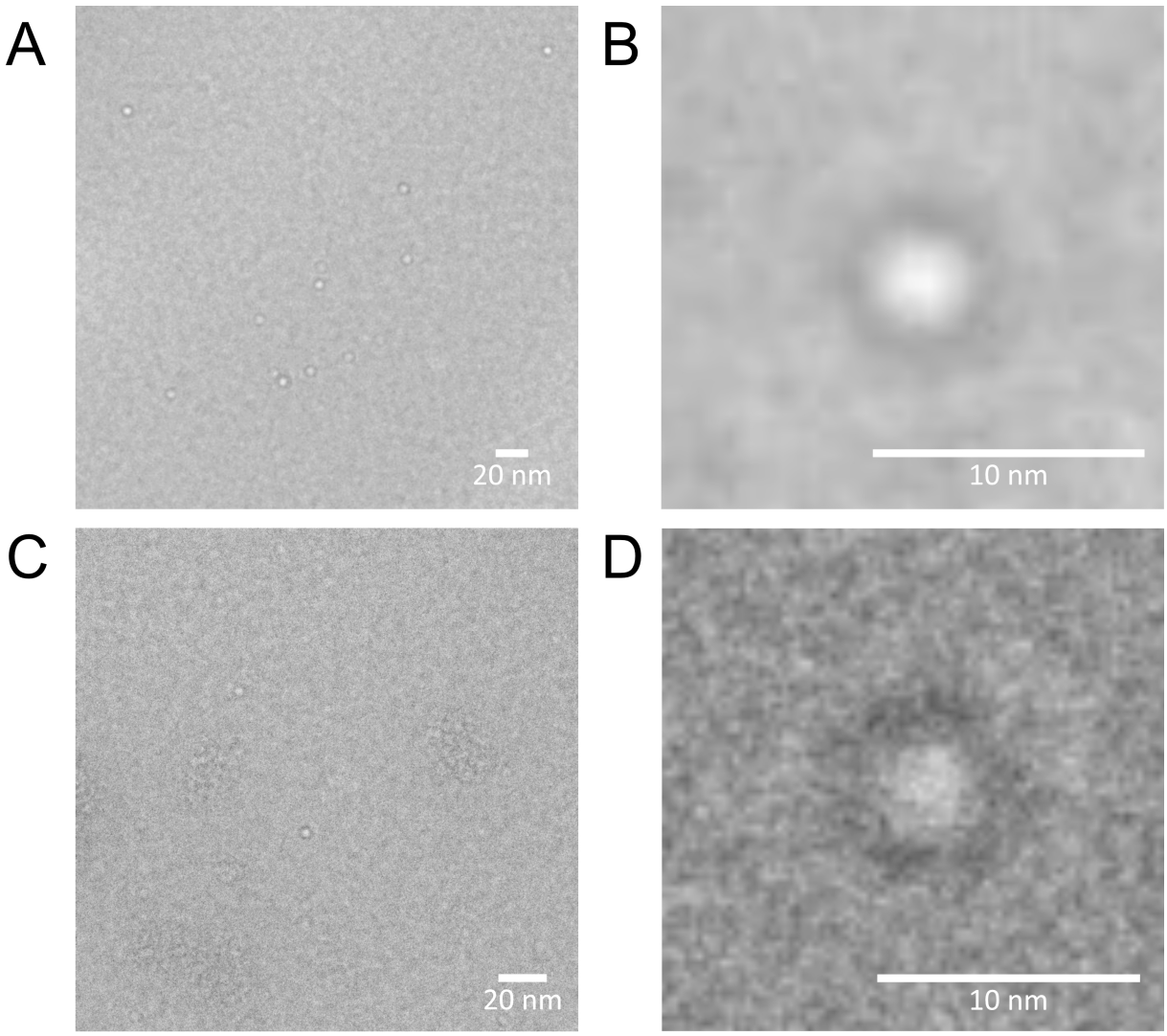


Figure 6.2: LPEM images of apoferritin protein from equine spleen sample. Panels A and C show the lower-magnification view of multiple apoferritin particles. Panels B and C show zoomed-in images of single apoferritin particles from panels A and C respectively. Scale bars are indicated in each image. Assembly data can be found in Table 2.4.

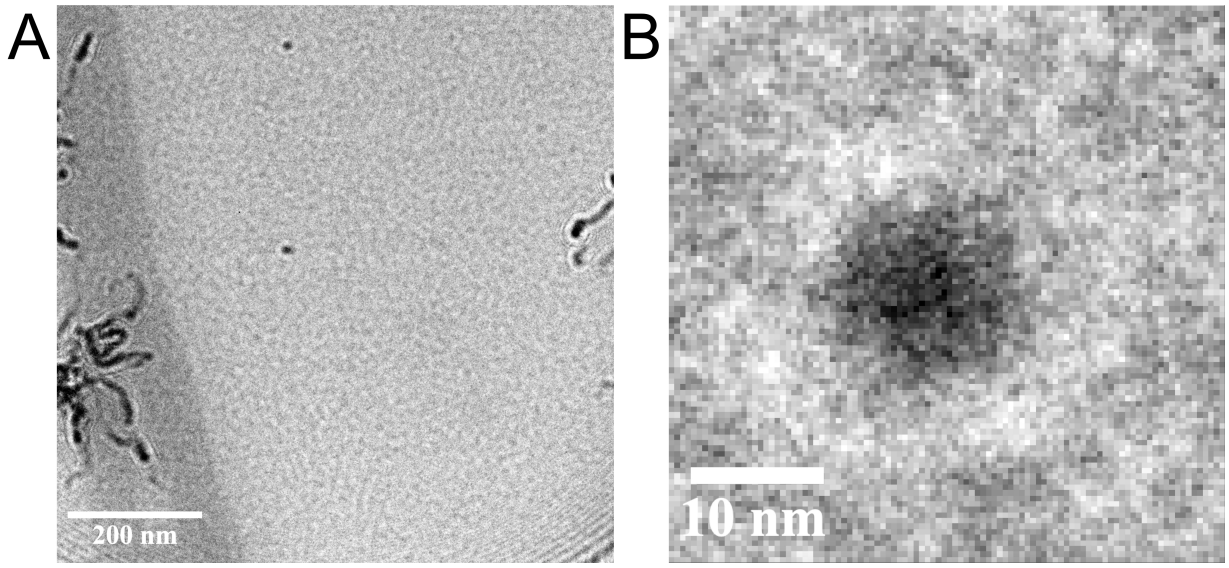


Figure 6.3: LPEM images of ferritin protein in liquid. Panel A shows a lower-magnification view of ferritin particles, and panel B shows a higher-magnification view of one ferritin particle. The scale bars are indicated in each image. These images are courtesy of Tyler Lott and Dr. Ariel Petruk.

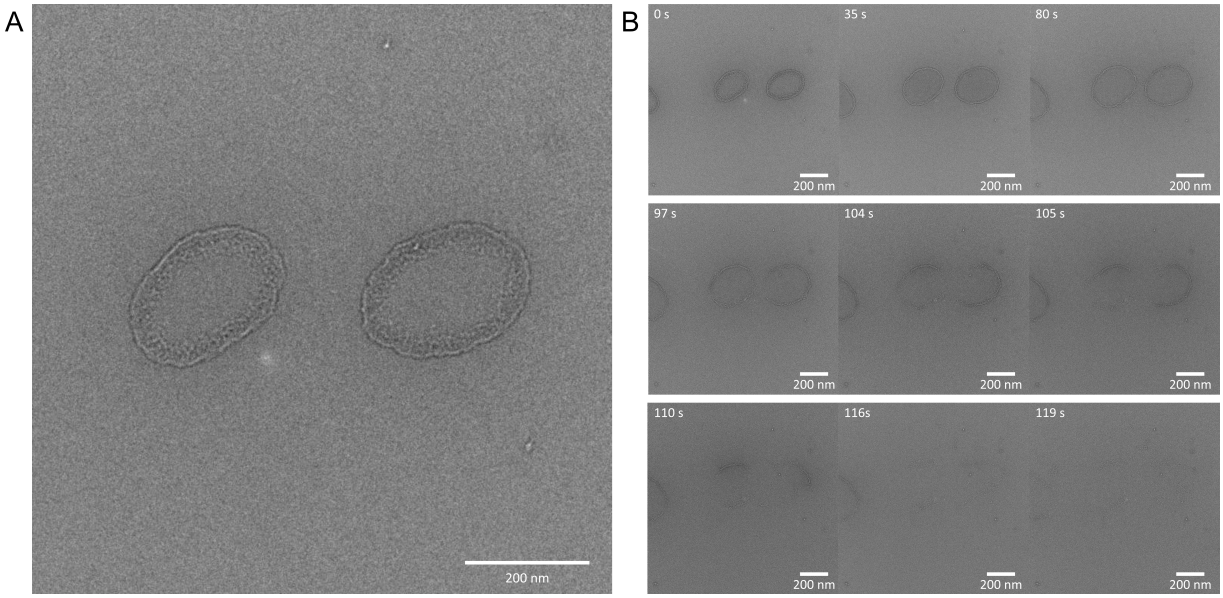


Figure 6.4: LPEM images of vesicles in equine spleen sample. Panel A is an image at time = 0, and panel B shows a time series from time 0 to 119 seconds (at select times) where the vesicles eventually disintegrate from irradiation of the electron beam. The scale bars are indicated in each image. Assembly data can be found in Table 2.4.

plasmid DNA, which mimics the coiled structure observed in AFM of a plasmid in liquid, and dry plasmid.[70,71] Analysis of EELS spectra obtained across two liquid window edges gave t/lambda measurements of 3.6 at the window edge, and 4.1 at the centre of the cell. This translates to an average of 524 nm of water at the window edge and 602 nm at the centre (calculations described in chapter 5). The finding that DNA was clearly visible in such a thick layer, with 25 nm silicon nitride total window, is very promising for future study of DNA in LPEM.

Though it was clear that the cell contained bulk water, with no visible cracks or aberrations in liquid thickness, the DNA showed no motion. A likely explanation for this behaviour is the charging of the insulating SiN_x windows. Bultema et al.[72] described a model where SiN_x LCs with no external bias experience positive window charging in the active viewing area due to secondary electron emission. The positive charge of the window will attract the negatively charged backbone of the DNA, holding the particles still on the membrane.

Electrostatic attraction of DNA to the LC window presents an interesting obstacle to observing DNA dynamics, which may be better observed when viewed in conductive material such as carbon-based LCs. With conductive membranes, the area outside the viewing region experiences a negative charge from secondary electron return flux through radial current in the conducting windows.[72] Thus in a conductive LC, DNA can be suspended in bulk liquid to undergo some dynamics when not being viewed, and conveniently viewed attached to the window when illuminated. Plasmid DNA dynamics should be examined further in a future study, as a suspension in alcohol can give insight into dynamics used in DNA extraction protocols (alcohol precipitation), and the processes used to perform molec-

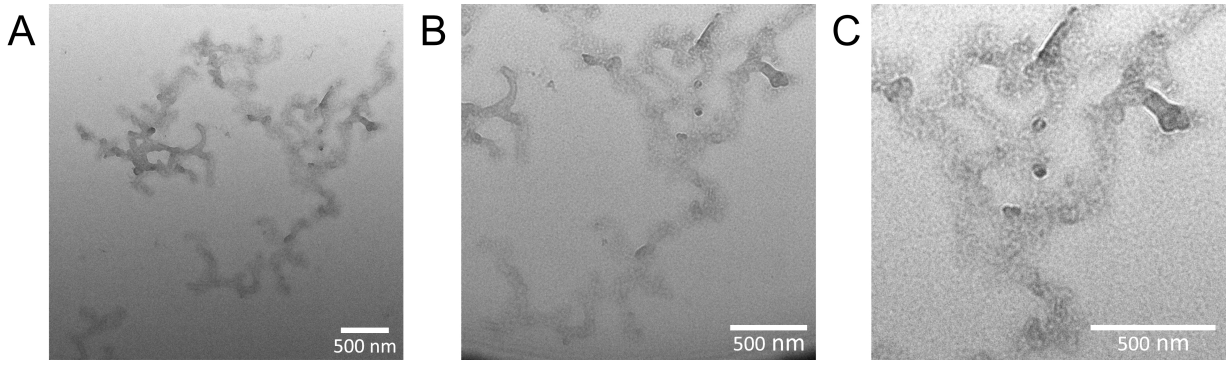


Figure 6.5: LPEM images of pAAV plasmid DNA. Panels A, B and C show different images from the same liquid cell assembly at different magnifications. The scale bars are indicated in each image. Assembly data can be found in Table 2.4.

ular cloning. This experiment showing plasmid DNA is the first examination of DNA with LPEM, and provides a benchmark for the quality of data that can be obtained from DNA in liquid environments.

6.5 Live cells

Ideally, live cells would be imaged as a final complement to the study of biomolecules. The bacterium *Pelagibacter communis* was chosen, as it is the smallest bacteria discovered to date. The small size of this bacteria would have been ideal for obtaining high-resolution images of cell ultrastructure using thin liquid layers. The dimensions of these cells are 400-1,300 nm long and 190-280 nm wide.[73] Best efforts to visualise this bacteria were unsuccessful. Initially, the cell density was determined to be a major barrier, as the cells do not grow abundant enough to have a decent probability to be viewed within the viewing area. The concentration of the cells to a pellet using ultracentrifugation was attempted,[73]

but no pellet was obtained. Despite this, every effort made to visualise the cultures (concentrated or not) resulted in the crashing of salt out of the solution. The salt concentration of the media required to grow this oceanic bacterium (i.e. seawater salt concentration) was so high, that any evaporation of the liquid droplet, in the brief time taken to assemble the liquid cells, resulted in the crashing of salt out of solution and likely plasmolysis, creation, and death of the bacteria.

The ability to observe other live cultures of bacteria in this system is yet to be explored further. Another good candidate would be the observation of Magnetospirillum magneticum, which has been studied with correlative electron and fluorescence microscopy with LPEM.[74] *Escherichia coli* would be another candidate, as it can be grown and pelleted reproducibly with standard centrifugation.

Though no live cells were seen, the salt crystal from the cell media was seen. The formation of salt crystals caused small cracks to form in the silicon nitride windows. Similar to carbon LCs, silicon nitride can be seen to seal pockets of water when broken. In Figure 6.6 the slow evaporation or freezing of water from a liquid pocket made the observation of salt crystal growth possible.

In summary, even with thick liquid layers, a wide array of biomolecules were visible at high resolution. I successfully images AAV, apoferritin, vesicles, and plasmid DNA in the liquid phase using thin SiN_x LCs I fabricated. Issues with LC design meant that these images were not obtained with the target 10 nm total SiN_x windows. However, future improvements to UeIL LC technology will be able to realise this and generate even higher quality images of biomolecules.

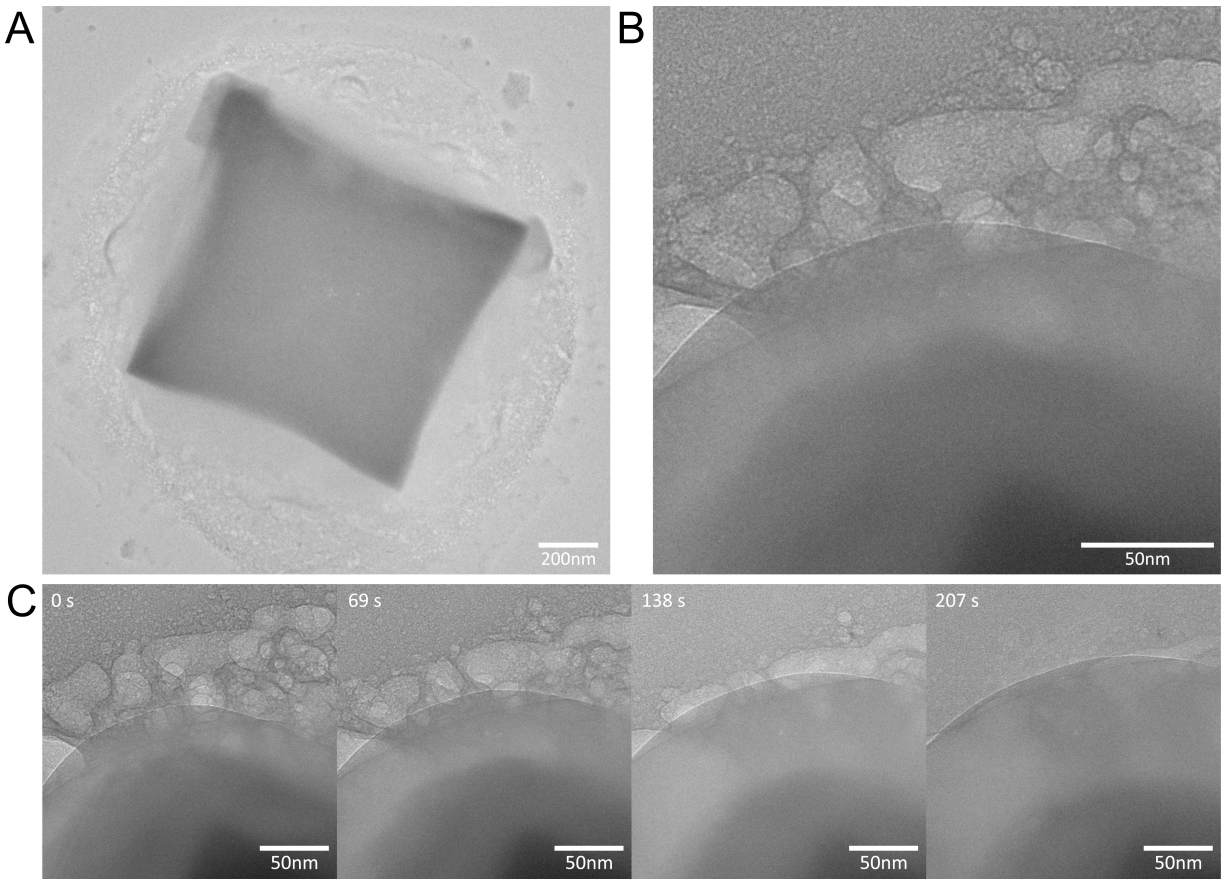


Figure 6.6: LPEM images of salt crystal formation in *Pelagibacter communis* sample. Panel A shows a lower-magnification view of a salt crystal formed in a liquid pocket. Panel B shows a higher-magnification view of the top left corner of the crystal, and panel C shows a time series of salt crystal growth with the time indicated in the top left corner. Panel B shows an enlarged image at 42 seconds into the time series. The scale bars are indicated in each image. Assembly data can be found in Table 2.4.

Chapter 7

Data analysis tools

Microscopy data is often stored in complex file types, in order to preserve a large amount of image data and corresponding metadata. Software currently available to view and manipulate some of these file types is unavailable or inaccessible, outdated, and/or does not come equipped with tools that are useful to most microscopists.

7.1 Image data and metadata analysis

Images generated during microscopy are commonly very large and difficult to manage, as they contain a lot of data in the form of high-resolution images and extensive metadata. Though the storage of metadata directly in the image files is critical in data management, there is no standard image format used in microscopy, thus there exist many different file types generated by different software. A popular data type is EMD, generated by the Velox software used in Thermo Fisher Scientific microscopes.

Velox acquires TEM and STEM images and videos in the EMD file format. The files contain metadata corresponding to each video frame, but the Velox software only shows the metadata of the first frame. Currently, the only way to view EMD files is through purchasing the Velox license, or use of the openNCEM Python package[75] developed by the National Center for Electron Microscopy (NCEM) at Lawrence Berkeley National Labs. In addition, the HyperSpy software, commonly used in analysis of EELS data, employs the NCEM framework to view EMD files.[76] Velox requires a software license, thus the NCEM package provides an open-source option for users familiar with Python. Implementation in HyperSpy allows for further accessibility to users not familiar with Python. However, neither GUI option allows for the visualisation of EMD metadata for each frame.

In-situ EM focuses on dynamic experiments and requires the flexibility of changing parameters on the fly - especially in an effort to capture images of elusive samples like biomolecules. Thus the ability to view metadata across all frames of acquired video is imperative. I developed a software plugin for Napari, an open-source software suite for microscope image processing, that allows the visualization and navigation of the EMD file type including access to the metadata for each individual frame. Development in the Napari software also provides users with convenient tools to annotate, analyse, and export data in convenient file formats.

The framework for this plugin was generated with the naperi-cookiecutter plugin, with functionality as a reader and widget. The reader makes use of the h5py[77] library to read the file, and custom software was developed to convert ASCII data coded in JSON format into a metadata library, for each frame. The widget was equipped with event captures to automatically update the metadata being viewed when new files or frames are selected, to

remove any possibility of confusing the metadata being observed by the user. The plugin is published in the Github repository: https://github.com/NickiShaw/napari-EMD.

An example is shown in 7.1, where the defocus is changed in a video of the edge of a silicon nitride window. The two images show the edge of the silicon nitride window, where the 'ghost' features indicate the change in focus, both in the sample and on the window edge. This demonstrates the successful update of metadata values, which update automatically when the frame is changed in the software.

ImageJ (also known as Fiji) is another popular image analysis software developed by the National Institutes of Health (NIH). ImageJ was created in 1997 and provides a larger library of plugins and tools for image analysis than Napari, which began development in 2018.[78] Thus a standalone Python script was developed to convert EMD files into JPG/PNG images while storing metadata in CSV format. This allows users the flexibility to import image stacks into ImageJ or other image editing software without EMD compatibility, while still maintaining a record of the metadata for each frame. The code for this is available at https://github.com/NickiShaw/microscopeFileProcessing.

7.2 EELS data analysis

EELS data can be viewed in the Digital Micrograph software provided by Gatan, though some analysis options require the purchase of a software license. Digital Micrograph is able to analyze EELS spectra, but the tools needed for the determination of liquid layer thickness suffer from errors in the integration, especially if the core loss peak is very large or

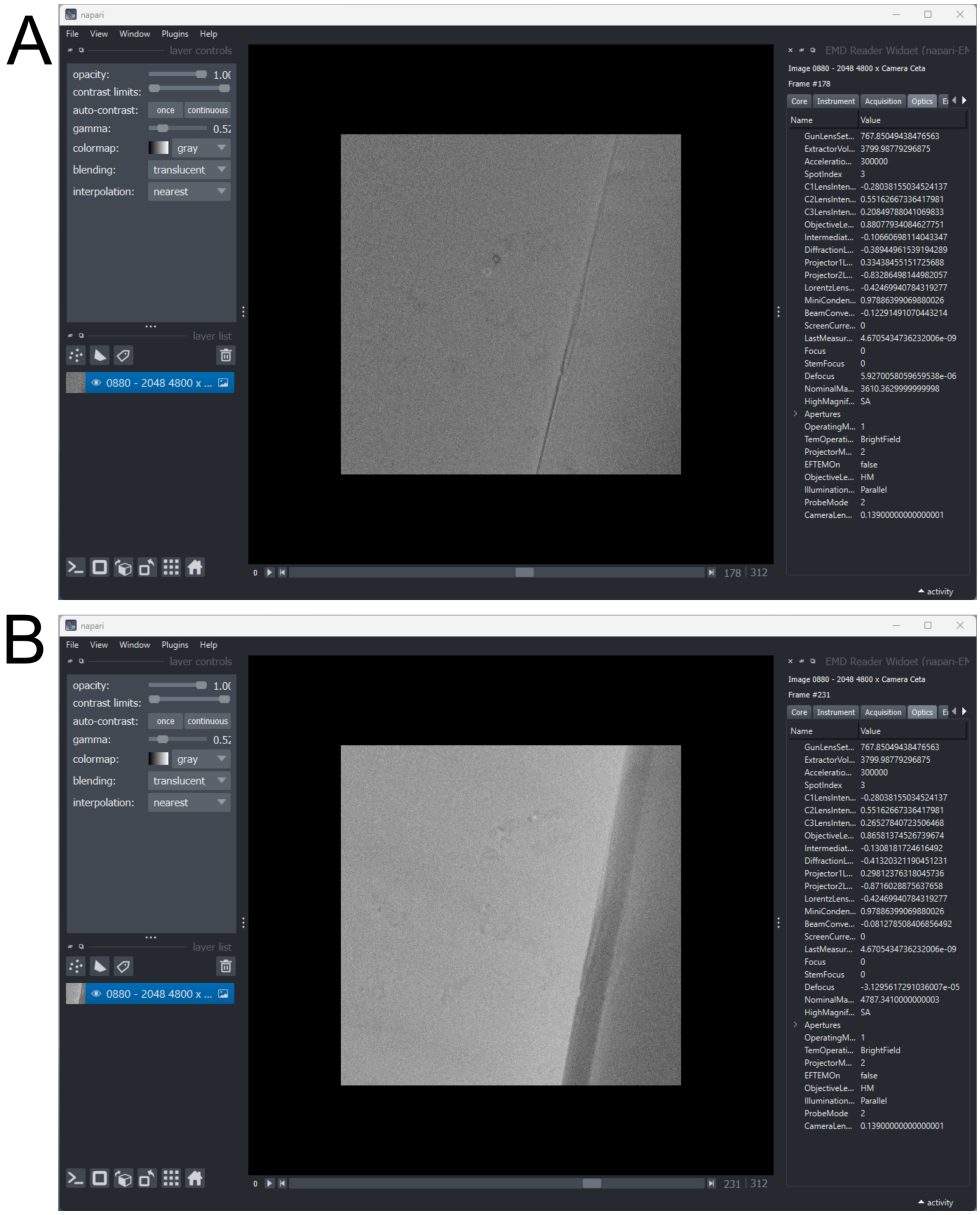


Figure 7.1: Napari-EMD plugin for visualisation of EMD images, videos, and metadata. Panel A shows frame number 178, where the defocus is 5.92e-06, in panel 2 the frame has changed to number 231 where the defocus is -3.12e-05.

small relative to the ZLP, which is the case with thick liquid layers or dry thin substrates. Digital micrograph also does not have the option to separate contributions from different materials, such as water and silicon nitride in the LC assembly.

The analysis of this data was thus streamlined through the development of a lightweight Python module. Users have the ability to manipulate data such as remove parts of line or area spectra that are outside of the viewing area (i.e. crop to the edge of the silicon chip substrate), as well as perform automatic or semi-automatic calculation of mean free path values, and thicknesses when transmission occurs through multiple materials. Estimation of the position of the window edge is done by plotting the total electron counts, and manually choosing a cutoff point. This was the best method determined to truncate datasets. Another option would have been to search for the silicon plasmon peak pattern (peaks at multiples of the silicon plasmon energy),[79] but these peaks were often obscured by the water present behind the thin silicon edge.

The three methods used to calculate the area of the ZLP: cutoff, reflect, and gauss are available for comparison. The cutoff method cuts the spectra between the ZLP and core loss peaks and computes the ZLP as the area before the cutoff. The reflect method employs the reflected tail method (the default used in Digital Micrograph), where the area before the ZLP apex is computed and doubled. The gauss method fits a Gaussian fit to the ZLP with limits set by the cutoff method unless otherwise specified, and the area is computed with the analytical solution to the Gaussian equation. With all the above options, the implementation of Python modules allows more flexibility for data analysis, such as manual selection of fitting limits, which avoids the fitting issues sometimes experienced in Digital Micrograph.

Easy visualisation of EELS data is available in the HyperSpy package.[76] Thus, the estimation of liquid layer thickness after the subtraction of LC material was the key motivation for the development of this software. Code to perform these calculations is also available at https://github.com/NickiShaw/microscopeFileProcessing.

Chapter 8

Mitigation of sample damage

Thin SiN_x windows are a huge leap for imaging of all samples, especially biosamples. However, to image biomolecules, another hurdle remains. Electron-induced sample damage caused through radiolysis causes swift damage to biomolecule samples, limiting our ability to observe particle dynamics.[22,24] In this chapter, electron dose and techniques to reduce electron dose are discussed. In addition, my *in silico* work analysing the effect of reduced-dose imaging techniques is presented.

8.1 Dose

Two values can be used to quantify the rate of sample damage: critical dose ($e^- A^{-2}$, where A is area), and dose rate also called electron flux ($e^- A^{-2} s^{-1}$).[47] Dose rate can affect the critical dose , and multiple factors can affect the localisation, flux, and diffusion of

radiolytic species.[32] For example, LC material can affect charging differently,[72] and liquid layer thickness, composition, and movement can affect the diffusion of radiolytic species.[32]

Importantly, LPEM has been shown to confer reduced electron damage in comparison to cryo EM experiments. This has been attributed to higher diffusion of radiolytic species in liquid phase.[32] Where cryo EM experiments have measured critical dose s of 60 $e^{-}A^{-2}$ for microtubules, LPEM experiments have measured critical dose of 720 $e^{-}A^{-2}$ for microtubules.[27] In LPEM, DNA dynamics have been observed at as little as 110 $e^{-}A^{-2}s^{-1}$ with conventional SiN_x LCs.[80]

The advantage of thin bulgeless LCs developed in this work is that images have less noise, thus less dose is required to view detailed structures of biomolecules (chapter 6). Previously, high-resolution imaging in LPEM required dose rates on the order of 1000 $e^{-}A^{-2}s^{-1}$ or higher.[47] However, dose rates that I have estimated to be approximately 0.13 or 7.3 $e^{-}A^{-2}s^{-1}$ were sufficient to view vesicles for up to 2 minutes with our updated LPEM technology (see calculations in chapter C). Reducing the dose during imaging further aims to increase acquisition times for the study of biomolecules.

8.2 Reducing electron dose

The energy transfer from electrons to the sample is described generally by Bethe's formula.[81] In equation 8.1 $\frac{-dE}{dx}$ is the rate of energy loss by the beam electrons, v is the velocity, e is the electric charge, m is the electron mass, N is the number of atoms per cm^3 in the sample, Z is the number of electrons per absorbing atom, $\bar{I}$ is the mean excitation

potential, and ϵ is the natural log base.[81]

$$\frac{-dE}{dx} = \frac{4\pi e^4 NZ}{mv^2} ln\left[\frac{mv^2}{2\bar{I}}\left(\frac{\epsilon}{2}\right)^2\right] \tag{8.1}$$

As discussed in Stenn and Bahr,[46] the Bethe formula[81] highlights that the electron energy imparted on the sample (electron dose) is dependent on the inverse square of electron velocity, and the thickness and density of the sample (the path length). Thus, low-dose imaging can be achieved by lowering acceleration voltages to $\leq$ 100keV. Unfortunately, lowering the dose of the collimated beam results in increased noise in images. Denoising techniques can be used to recover noisy images acquired at low doses.[82] This is done by representing the noise through analytical expressions such as Gaussian or Poisson noise and then removing them from the image.[82] Alternatively, deep learning models can be used to remove the noise from images, if a sufficient training dataset is acquired.[82]

Another approach referred to as sparse sampling (or subsampling) can be used to acquire a sparse representation of the image, which would result in an image with missing pixels.[83] With this technique, inpainting methods can be used to fill in the gaps.[84] The difference in denoising and inpainting techniques is outlined in Figure 8.1.

Similarly to denoising, inpainting can be performed through algorithmic approaches or deep learning.[83–85] Sparse sampling in STEM mode requires scan control of the microscope, which requires a scan control unit which is not provided with most microscopes. This presents a challenge in performing sparse acquisitions, whereas reducing the acceleration voltage for low-dose imaging and denoising is a more accessible technique. In contrast, it is easier to implement an inpainting algorithm, since the defect is known (i.e. which pixels

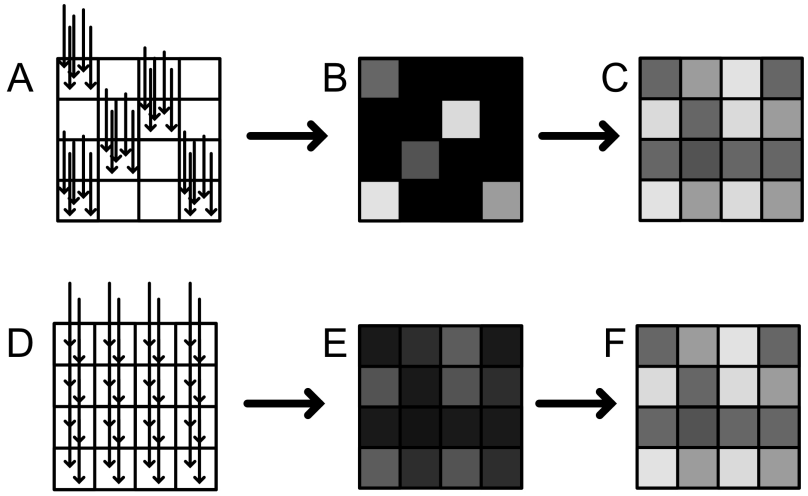


Figure 8.1: Low dose imaging techniques. Panels A-C show the inpainting process, and panels D-F show the denoising process. Panels A and D depict a simple representation of how dose is distributed across the pixels in an image to perform reduced dose imaging. Panels D and E show the data that would be acquired from A and D respectively, where D shows sparse bright pixels, and E shows complete but dark/noisy pixels. Panels C and F show the final image that would ideally be the same as normal higher dose imaging, where B to C is inpainting, and E to F is denoising.

are missing), but denoising is harder to implement because assumptions must be made on the type of noise present.

Sanders and Dwyer,[86] showed importantly, that at high doses, inpainting performed worse than denoising, but at low doses inpainting performed better than denoising. However, the cutoff defined for low-dose imaging where inpainting becomes preferable to denoising was supposedly low, but not defined in terms of dose.[86] What this study does not account for is an implementation in the liquid phase, where the improved diffusion of radiolytic species can reduce sample damage.[27] The implementation of STEM imaging may offer beneficial dispersion of dose during imaging that could not be achieved with a

collimated beam. Analysis of the imaging speed, sparse sampling, and reduction of sample damage in STEM mode is a key area for future study.

8.3 Sparse sampling techniques

Inpainting requires a sparse scan of the image, and sparser signals (random, evenly distributed signals) are expected to perform better during inpainting.[87] Though it is possible to configure the scan coils of a microscope to acquire a truly sparse image in STEM mode, this type of scan (a Bernoulli scan) creates a lot of uncertainty in the beam position.[88] This uncertainty of the beam position is called beam rise, and research by Kovarik et al.,[87] showed that sparser scans have higher beam rise. The result of Bernoulli scans is a distorted image, because the pixels are mapped to incorrect locations.[87]

Sparse scans with more uniform movements of the electron beam have been investigated, such as line-hopping,[87] block-based scans,[89] and spiral scans.[88] Spiral scans are the most promising technique for reduced dose imaging because they have the added benefit of conferring uniform dose across the scans, when performed at a constant linear velocity (CLV scan).[88] Regular raster scans in STEM mode, suffer from uneven distribution of dose, originating from the fly-back time.[90] The fly-back time is normally set to longer than the scan speed, to account for beam rise when the scan changes direction. Though some distortions will be present in a CLV scan as the beam changes angular velocity, these distortions can be easily characterised and removed from images.[90] With this in mind, my implementation of inpainting employed random masks and spiral masks in parallel, to study the potential effect of Bernoulli and CLV scans on inpainting performance.

8.4 Inpainting methods

Inpainting can be performed through algorithmic methods,[50,52] dictionary learning,[83] or deep learning.[85] I focused on algorithmic approaches, as they are simple implementations of inpainting and are readily available.[51,53] Algorithms rely on the same principles that artists would use to restore paintings: the surrounding area dictates the features to be inpainted, and the surrounding texture should be preserved.[84] Mathematically, these conditions translate to observation of isophotes (gradient lines, Figure 8.2A), and neighbour-based decision making.[50,52] The general scheme for inpainting (shown in Figure 8.2) is to fill the missing region Ω by solving for each point p, using the neighbourhood ϵ of the known region Φ, then advancing the point p until inpainting is complete.[50,52] The Telea fast marching method, and biharmonic function inpainting were selected to perform inpainting, as they are implemented in robust and peer-reviewed software.[51,53] The weights of the neighbourhood, and methods used to calculate p values are described elsewhere.[50,52]

To generate mock subsampled images, random and spiral masks were used to remove pixels from existing TEM images. The spiral mask was generated following the equations outlined by Sang et al.[88] for CLV scans, shown in equations 8.2 and 8.3. Because the generation of the spirals produced many overlapping points in the mask, the parameters were adjusted such that the inpainting value reflected the total number of pixels removed (removing contribution from duplicates). In equations 8.2 and 8.3, x and y are the co-ordinates of each pixel in 2D space, ω is the frequency, and t is time (progression of the scan). For *in silico* study, both ω and t are arbitrary, because the spiral can be made to any size and mapped to the size of the image to be masked. The random mask is made

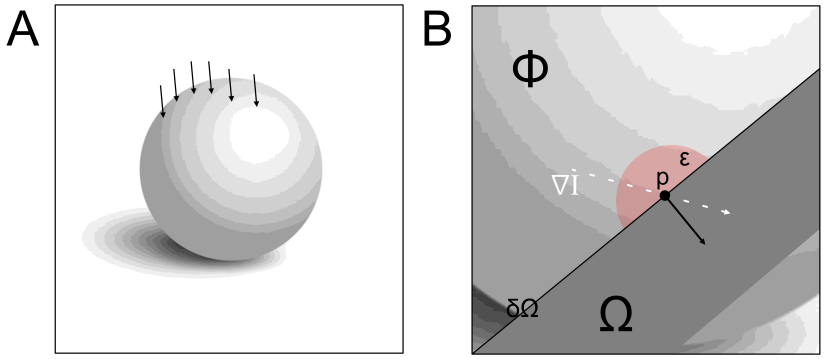


Figure 8.2: Basic rationale for algorithmic inpainting. Panel A shows a posterized shaded sphere, where the black arrows highlight isophote lines. Panel B shows an isophote line in the direction of the white dashed arrow marked ∇I, where the grey area marked Ω is the area to be inpainted, and the rest of the image Φ contains known image information. The red region marked ϵ is the neighbourhood that will be used to calculate the value filled at point p, where the direction of inpainting (marked by the black arrow) is perpendicular to the boundary of the missing region $\delta\Omega$.

simply through the available (pseudo-)randomization code. Code to generate these masks is available at https://github.com/UeIL-Waterloo/InpaintingEMdata.

$$x = \sqrt{t}\cos\left(\omega\sqrt{t}\right) \tag{8.2}$$

$$y = \sqrt{t}\sin\left(\omega\sqrt{t}\right) \tag{8.3}$$

8.5 Implementation of inpainting

My work focused on implementing basic algorithmic approaches to inpainting biomolecule data *in silico*. This analysis is the first known that addresses the inpainting of LPEM data. I implemented two algorithms in Python modules to perform inpainting: the Telea,[50,51]

and Biharmonic[52,53] algorithms. In addition, given that implementation of sparse sampling would be best performed with spiral scans,[88] I implemented spiral, and random masks, and compared their relative inpainting performance. Code to perform these calculations is available at https://github.com/UeIL-Waterloo/InpaintingEMdata.

Ground truth and inpainted images were compared using RMSE calculations, a method used in previous studies.[85,89] In equation 8.4, n is the number of pixels, x_i is the ground truth, and y_i is the inpainted result for each pixel, i.

$$RMSE = \sqrt{\frac{1}{n}\sum_{i=1}^{n}(x_i - y_i)^2} \tag{8.4}$$

The r was also used to determine the similarity between the images. In equation 8.5 the x_i is the ground truth, and y_i is the inpainted result for each pixel, i, where $\bar{y_i}$ and $\bar{x_i}$ are the average pixel values in each image.

$$P_{x,y} = \frac{\sum (x_i - \bar{x_i})(y_i - \bar{y_i})}{\sqrt{\sum (x_i - \bar{x_i})^2 \sum (y_i - \bar{y_i})^2}} \tag{8.5}$$

Inpainted images were found, qualitatively, to have high degrees of similarity (Figure 8.3). Though RMSE and the r do not account for structure, they are useful in determining the slight differences between inpainted and original images. The higher RMSE values, and lower r values, indicate the higher the mismatch between two images, and the lower the performance of the inpainting algorithm.

Figure 8.4 show the RMSE and r values for between original and inpainted images,

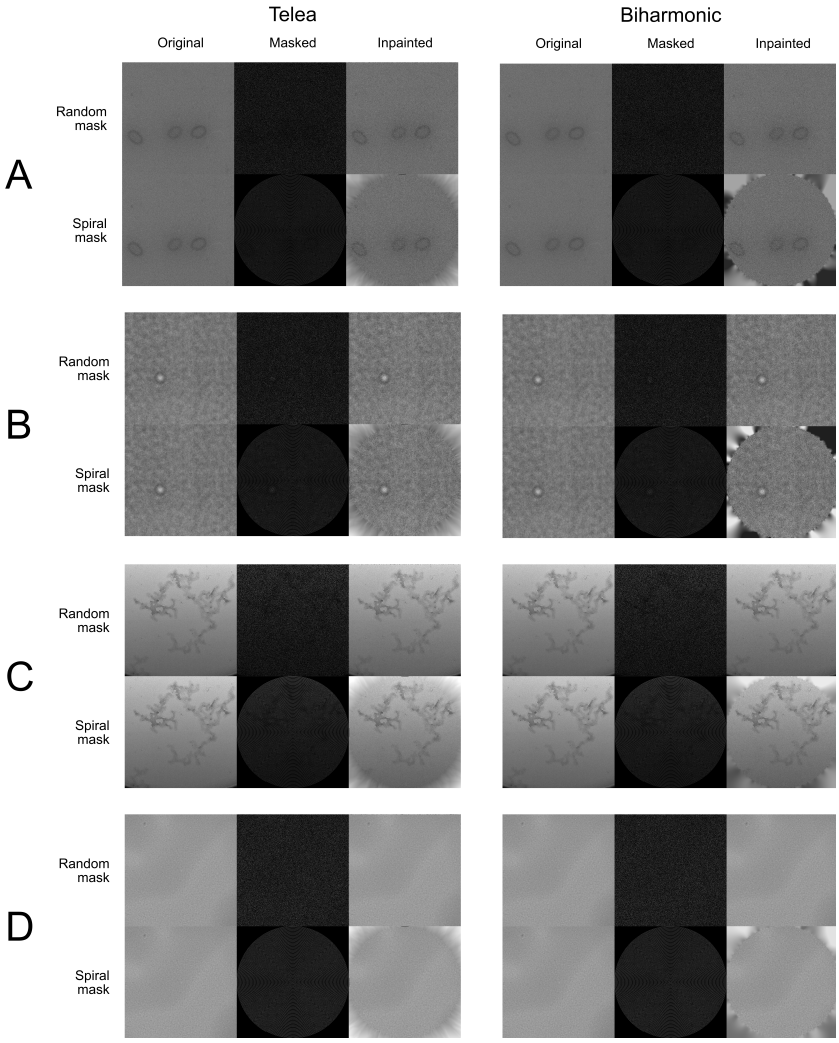


Figure 8.3: Inpainting results for biomolecule images at 80%. Set A shows the image of vesicles, panel B shows the image of AAV, panel C shows the image of pAAV (plasmid) and panel D shows the image of apoferritin. Panels on the left show results from the Telea algorithm, while panels n the right show results from the Biharmonic algorithm. Panels labelled 'random mask' show data where random masks were used to artificially subsample image pixels, and panels labelled 'spiral mask' show data where spiral masks were used to artificially subsample image pixels. All images were inpainted at 80% (20% of the original data).

where raw data for these inpainting tests is provided in Appendix B. The data show that the biharmonic algorithm performed inpainting more successfully than the Telea algorithm. Both algorithms produced the expected trend, where inpainted images become less similar as the level of masking is increased.[87] Notably, the performance of either algorithm depends largely on the image, with each algorithm exhibiting similar trends across the dataset.

The use of spiral masks was performed to analyse the impact of using a physically achievable scan, as opposed to random masking which is ideal for inpainting. RMSE data from spiral and random masks using the biharmonic algorithm were analysed. The random mask results were cropped to the circular boundary applied to the spiral-masked images before the RMSE was calculated, to prevent the corner data from impacting the comparison, seen in Figure 8.5. The random masks are expected to achieve better inpainting results (lower RMSE values) than the spiral scans.[87] However, the trend shows that the spiral scan achieves very similar quality inpainting at 50%. Even at 80% inpainting, the difference between random and spiral scans has less impact on the quality of the inpainting than the image used. This is very promising towards the implementation of inpainting to reduce electron dose. It is estimated from this data, and the images shown in Appendix B, that 80% sampling with spiral scans is achievable without the loss of key data.

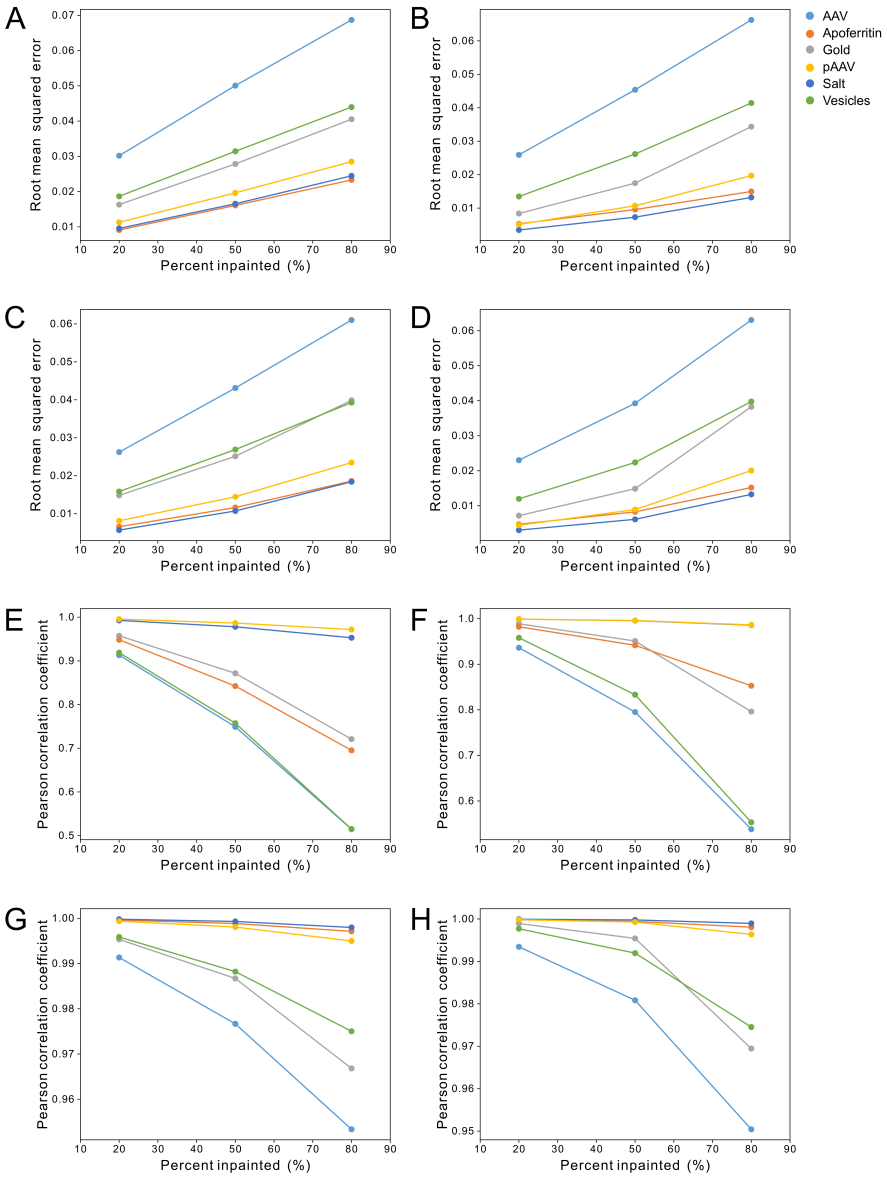


Figure 8.4: Inpainting quality assessments. Panels A-D show quality assessed with RMSE calculations and panels E-H show quality assessed with r calculations. Panels A, C, E, and G show results from the Telea algorithm, while panels B, D, F, and H show results from the Biharmonic algorithm. Panels A&B, and E&F show data where random masks were used to artificially subsample image pixels, and panels C&D, and G&H show data where spiral masks were used to artificially subsample image pixels. Extended data can be seen in Appendix B.

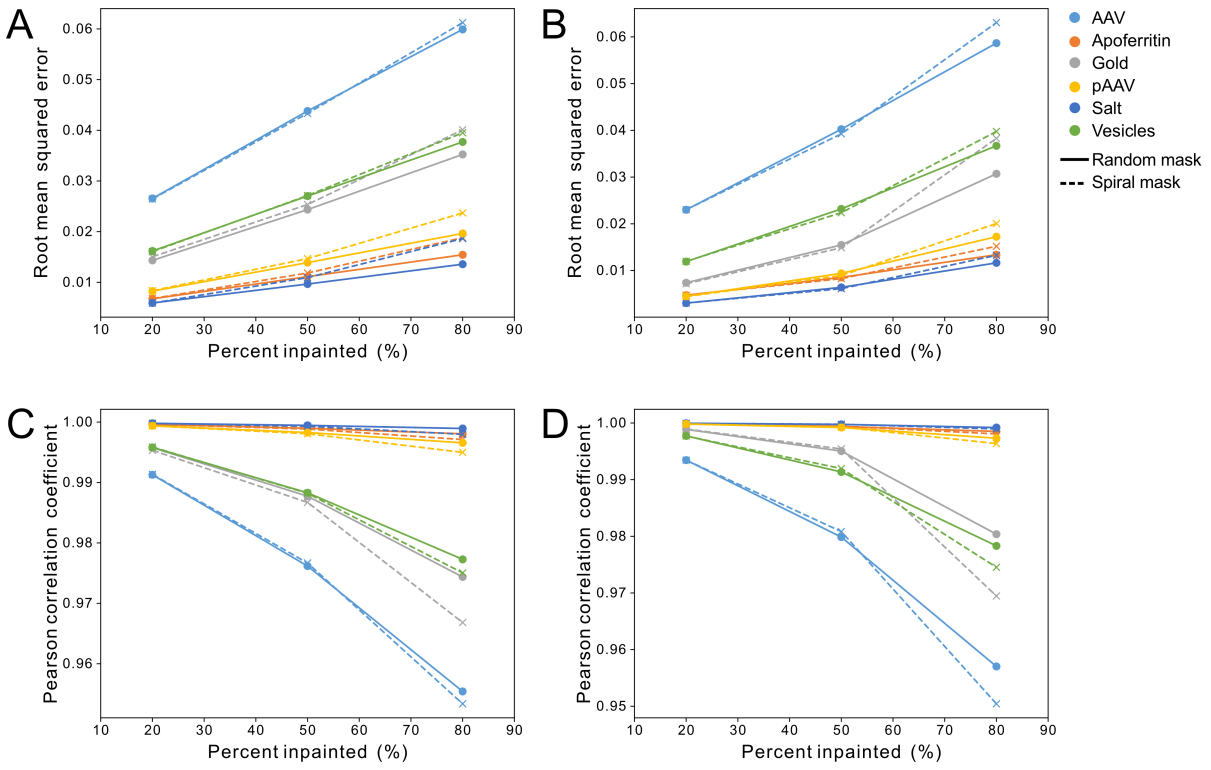


Figure 8.5: Inpainting quality assessments comparing spiral and random masks. Panels A&B show quality assessed with RMSE calculations and panels C&D show quality assessed with r calculations. Panels A&C show results from the Telea algorithm, while panels B&D show results from the Biharmonic algorithm. In all plots solid lines with 'o' markers depict data obtained where random masks were used to artificially subsample image pixels, and dotted lines with 'x' markers depict data obtained where spiral masks were used to artificially subsample image pixels. The random masks were masked with the circular edges seen in the spiral masks for these calculations. The legend is the same for all graphs, where the raw images can be seen in Appendix B.

Chapter 9

Conclusions and future outlook

In summary, I have demonstrated the fabrication of 5 nm SiN_x windows in improved LC technology which confers reduced bulging, higher transmission, and higher resolution imaging in the liquid phase than was previously possible. I verified the thickness of these thin windows through EELS, and AFM, and characterised the transmission of these windows with EELS, and resolution using CTEM imaging of gold nanorods. Experiments investigating transmission through 5 nm windows showed transmission comparable with carbon-based LCs. Dry 5 nm windows also conferred 0.62 Å resolution, and thus would also be suitable as a substrate for dry TEM experiments. I was also able to show that these 5 nm SiN_x windows can successfully contain water in LC assemblies using EELS.

Future work on LC technology includes fabrication of calibrated LCs with correct spacer sizes. This will hopefully enable the robust and reproducible use of the UeIL LC technology that was previously demonstrated with 30 nm SiN_x windows.[4] However, in collaboration

with other members of the UeIL I was able to troubleshoot initial issues in the design of these LCs.

Future work for LC window development includes testing alternative window materials. Al_2O_3 presents an ideal candidate, and in my work, the fabrication of these windows was performed successfully. However, more research should be done to improve the yield of Al_2O_3 windows before it can be used in LCs. In addition, the deposition of thin materials onto supportive 5 nm SiN_x membranes should be investigated.

In this thesis, I demonstrate the use of thin SiN_x windows to image biomolecules in the liquid phase. The biosamples I analysed include apoferritin, AAV, pAAV, and vesicles, all demonstrated at high resolution. The results showing pAAV are the first demonstration of DNA imaging in LPEM. The biomolecule data shown here represent exciting new heights for bioimaging in native environments, using thin windows and advanced loading technology I helped develop in the UeIL.

In addition, I have shown that spiral inpainting does not significantly reduce the performance of inpainting up to 80% of images of biomolecules taken in liquid phase experiments. My analysis also showed that inpainting spiral-masked images has no significant reduction in quality in comparison to using a random mask. This indicates that spiral imaging can be used to perform low-dose imaging, as long as the spiral distortion is corrected.[90] The success of the algorithmic approaches to inpainting indicates that more complex methods such as dictionary and deep learning may not be pertinent to pursue. Though, these methods may be more appropriate if the image sampling is reduced to $\geq$20% ($\leq$80% inpainting).

The next steps in inpainting analysis would include testing larger datasets, to deter-

mine what properties give data better performance (i.e. noise, contrast). To analyse more inpainting algorithms, especially with respect to computational performance. These algorithms are quite time-consuming and implementation of inpainting in LPEM would ideally be real-time, requiring < 500 ms processing for each frame as a video is acquired. In addition, the images in this analysis are TEM images, thus would only be comparable to bright field TEM. Thus inpainting of darkfield images should be investigated.

Throughout my work, I have developed four key pieces of software available to the scientific community. The first is a program that estimates the electron transmission of different materials at different acceleration voltages from theoretical electron scattering data. The second is a plugin for the Napari image analysis software suite that enables the processing of EMD image data and metadata in a frame-wise manner, which was not previously accessible. The third enables standalone processing of EMD data independent of Napari, and enables EELS data analysis, including estimation of thick liquid layers. Finally, I developed software to perform random and spiral masking of images and inpainting using algorithmic methods.

In addition to low-dose imaging, phase contrast imaging is emerging as an invaluable tool for biosample imaging in TEM. Though this technology has yet to reach implementation in LPEM, preliminary results in cryo EM experiments have shown a massive increase in sample contrast with this technique.[91] A phase plate is used to shift the relative phase between the scattered and unscattered electrons.[91] With phase plates imaging can be performed on light samples such as biomolecules without defocus, which causes a loss of resolution in the images.[91] I believe that implementation of the UeIL loading station technology and thin SiN_x window LCs developed in this work, in conjunction with phase

plate imaging, will allow for imaging of biomolecule dynamics in a way never before witnessed. Also, that groundbreaking work in LPEM will revolutionise biomolecule research, healthcare, and nanotechnology.

Bibliography

(1) Lott, T. S.; Petruk, A. A.; Shaw, N. A.; Hamada, N.; Andrei, C. M.; Liu, Y.; Liu, J.; Sciaini, G. Robust fully controlled nanometer liquid layers for high resolution liquid-cell electron microscopy. *Lab on a Chip* **2023**, DOI: 10.1039/D3LC00190C.

(2) Wessner, D.; Dupont, C.; Charles, T.; Neufeld, J., *Microbiology*; John Wiley & Sons: 2017.

(3) Hartley, H. Origin of the Word 'Protein'. *Nature* **1951**, *168*, 244–244, DOI: 10.1038/168244a0.

(4) Robinson, A. L. Electron Microscope Inventors Share Nobel Physics Prize. *Science* **1986**, *234*, 821–822, DOI: 10.1126/science.234.4778.821.

(5) Callaway, E. Revolutionary cryo-EM is taking over structural biology. *Nature* **2020**, *578*, 201–201, DOI: 10.1038/d41586-020-00341-9.

(6) Abbe, E. Beiträge zur Theorie des Mikroskops und der mikroskopischen Wahrnehmung. *Archiv für Mikroskopische Anatomie* **1873**, *9*, 413–468, DOI: 10.1007/BF02956173.

(7) F.R.S, L. R. XXXI. Investigations in optics, with special reference to the spectroscope. *The London, Edinburgh, and Dublin Philosophical Magazine and Journal of Science* **2009**, DOI: 10.1080/14786447908639684.

(8) Kruger, D.; Schneck, P.; Gelderblom, H. Helmut Ruska and the visualisation of viruses. *The Lancet* **2000**, *355*, 1713–1717, DOI: 10.1016/S0140-6736(00)02250-9.

(9) Broglie, L. D. Recherches sur la théorie des Quanta. *Annales de Physique* **1925**, *10*, 22–128, DOI: 10.1051/anphys/192510030022.

(10) Von Borries, B.; Ruska, E.; Ruska, H. Bakterien und Virus in Übermikroskopischer Aufnahme. *Klinische Wochenschrift* **1938**, *17*, 921–925, DOI: 10.1007/BF01775798.

(11) Williams, D. B.; Carter, C. B., *Transmission Electron Microscopy*; Springer US: Boston, MA, 2009, DOI: 10.1007/978-0-387-76501-3.

(12) Egerton, R. F., *Electron energy-loss spectroscopy in the electron microscope*, Third edition; The language of science; Springer: New York, 2011.

(13) Egerton, R. In *Electron Energy-Loss Spectroscopy in the Electron Microscope*, Egerton, R., Ed.; Springer US: Boston, MA, 2011, pp 29–109, DOI: 10.1007/978-1-4419-9583-4_2.

(14) Wu, H.; Su, H.; Joosten, R. R. M.; Keizer, A. D. A.; van Hazendonk, L. S.; Wirix, M. J. M.; Patterson, J. P.; Laven, J.; de With, G.; Friedrich, H. Mapping and Controlling Liquid Layer Thickness in Liquid-Phase (Scanning) Transmission Electron Microscopy. *Small Methods* **2021**, *5*, 2001287, DOI: 10.1002/smtd.202001287.

(15) Liao, Y. Practical electron microscopy and database. *An Online Book* **2006**.

(16) Wu, H.; Friedrich, H.; Patterson, J. P.; Sommerdijk, N. A. J. M.; de Jonge, N. Liquid-Phase Electron Microscopy for Soft Matter Science and Biology. *Advanced Materials* **2020**, *32*, 2001582, DOI: 10.1002/adma.202001582.

(17) Schuh, T.; de Jonge, N. Liquid scanning transmission electron microscopy: Nanoscale imaging in micrometers-thick liquids. *Comptes Rendus Physique* **2014**, *15*, 214–223, DOI: 10.1016/j.crhy.2013.11.004.

(18) Glaeser, R. M. Invited Review Article: Methods for imaging weak-phase objects in electron microscopy. *Review of Scientific Instruments* **2013**, *84*, 111101, DOI: 10.1063/1.4830355.

(19) Renaud, J.-P.; Chari, A.; Ciferri, C.; Liu, W.-t.; Rémigy, H.-W.; Stark, H.; Wiesmann, C. Cryo-EM in drug discovery: achievements, limitations and prospects. *Nature Reviews Drug Discovery* **2018**, *17*, 471–492, DOI: 10.1038/nrd.2018.77.

(20) Matadeen, R.; Patwardhan, A.; Gowen, B.; Orlova, E. V.; Pape, T.; Cuff, M.; Mueller, F.; Brimacombe, R.; van Heel, M. The Escherichia coli large ribosomal subunit at 7.5 Å resolution. *Structure* **1999**, *7*, 1575–1583, DOI: 10.1016/S0969-2126(00)88348-3.

(21) Yip, K. M.; Fischer, N.; Paknia, E.; Chari, A.; Stark, H. Atomic-resolution protein structure determination by cryo-EM. *Nature* **2020**, *587*, 157–161, DOI: 10.1038/s41586-020-2833-4.

(22) Jonaid, G.; Dearnaley, W. J.; Casasanta, M. A.; Kaylor, L.; Berry, S.; Dukes, M. J.; Spilman, M. S.; Gray, J. L.; Kelly, D. F. High-Resolution Imaging of Human Viruses

in Liquid Droplets. *Advanced Materials* **2021**, *33*, 2103221, DOI: 10.1002/adma.202103221.

(23) Kelly, D. F.; DiCecco, L.-A.; Jonaid, G. M.; Dearnaley, W. J.; Spilman, M. S.; Gray, J. L.; Dressel-Dukes, M. J. Liquid-EM goes viral – visualizing structure and dynamics. *Current Opinion in Structural Biology* **2022**, *75*, 102426, DOI: 10.1016/j.sbi.2022.102426.

(24) Ross, F. M. Opportunities and challenges in liquid cell electron microscopy. *Science* **2015**, *350*, aaa9886, DOI: 10.1126/science.aaa9886.

(25) Ruska, E. Beitrag zur übermikroskopischen Abbildung bei höheren Drucken. *Kolloid-Zeitschrift* **1942**, *100*, DOI: 10.1007/BF01519549.

(26) Williamson, M. J.; Tromp, R. M.; Vereecken, P. M.; Hull, R.; Ross, F. M. Dynamic microscopy of nanoscale cluster growth at the solid–liquid interface. *Nature Materials* **2003**, *2*, 532–536, DOI: 10.1038/nmat944.

(27) Keskin, S.; Kunnas, P.; de Jonge, N. Liquid-Phase Electron Microscopy with Controllable Liquid Thickness. *Nano Letters* **2019**, *19*, 4608–4613, DOI: 10.1021/acs.nanolett.9b01576.

(28) Hauwiller, M. R.; Ondry, J. C.; Alivisatos, A. P. Using Graphene Liquid Cell Transmission Electron Microscopy to Study in Situ Nanocrystal Etching. *JoVE* **2018**, e57665, DOI: 10.3791/57665.

(29) Textor, M.; de Jonge, N. Strategies for Preparing Graphene Liquid Cells for Transmission Electron Microscopy. *Nano Letters* **2018**, *18*, 3313–3321, DOI: 10.1021/acs.nanolett.8b01366.

(30) Dwyer, J. R.; Harb, M. Through a Window, Brightly: A Review of Selected Nanofabricated Thin-Film Platforms for Spectroscopy, Imaging, and Detection. *Applied Spectroscopy* **2017**, *71*, 2051–2075, DOI: 10.1177/0003702817715496.

(31) Yuk, J. M.; Park, J.; Ercius, P.; Kim, K.; Hellebusch, D. J.; Crommie, M. F.; Lee, J. Y.; Zettl, A.; Alivisatos, A. P. High-Resolution EM of Colloidal Nanocrystal Growth Using Graphene Liquid Cells. *Science* **2012**, *336*, 61–64, DOI: 10.1126/science.1217654.

(32) Keskin, S.; de Jonge, N. Reduced Radiation Damage in Transmission Electron Microscopy of Proteins in Graphene Liquid Cells. *Nano Letters* **2018**, *18*, 7435–7440, DOI: 10.1021/acs.nanolett.8b02490.

(33) Cho, H.; Jones, M. R.; Nguyen, S. C.; Hauwiller, M. R.; Zettl, A.; Alivisatos, A. P. The Use of Graphene and Its Derivatives for Liquid-Phase Transmission Electron Microscopy of Radiation-Sensitive Specimens. *Nano Letters* **2017**, *17*, 414–420, DOI: 10.1021/acs.nanolett.6b04383.

(34) Azim, S.; Bultema, L. A.; Kock, M. B. d.; Osorio-Blanco, E. R.; Calderón, M.; Gonschior, J.; Leimkohl, J.-P.; Tellkamp, F.; Bücker, R.; Schulz, E. C.; Keskin, S.; Jonge, N. d.; Kassier, G. H.; Miller, R. J. D. Environmental Liquid Cell Technique for Improved Electron Microscopic Imaging of Soft Matter in Solution. *Microscopy and Microanalysis* **2021**, *27*, 44–53, DOI: 10.1017/S1431927620024654.

(35) Peckys, D.; Veith, G.; Joy, D.; Jonge, N. Nanoscale Imaging of Whole Cells Using a Liquid Enclosure and a Scanning Transmission Electron Microscope. *PloS one* **2009**, *4*, e8214, DOI: 10.1371/journal.pone.0008214.

(36) Leenheer, A. J.; Sullivan, J. P.; Shaw, M. J.; Harris, C. T. A Sealed Liquid Cell for In Situ Transmission Electron Microscopy of Controlled Electrochemical Processes. *Journal of Microelectromechanical Systems* **2015**, *24*, 1061–1068, DOI: 10.1109/JMEMS.2014.2380771.

(37) Huang, T.-W.; Liu, S.; Yun-Ju, C.; Hsieh, H.-Y.; Tsai, C.-Y.; Huang, Y.-T.; Mirsaidov, U.; Matsudaira, P.; Tseng, F.-G.; Chang, C.-S.; Chen, F.-R. Self-aligned wet-cell for hydrated microbiology observation in TEM. *Lab on a chip* **2011**, *12*, 340–7, DOI: 10.1039/c1lc20647h.

(38) Yang, R.; Mei, L.; Fan, Y.; Zhang, Q.; Liao, H.-G.; Yang, J.; Li, J.; Zeng, Z. Fabrication of liquid cell for in situ transmission electron microscopy of electrochemical processes. *Nature Protocols* **2022**, DOI: 10.1038/s41596-022-00762-y.

(39) Petruk, A. A.; Allen, C.; Rivas, N.; Pichugin, K.; Sciaini, G. High flow rate nanofluidics for in-liquid electron microscopy and diffraction. *Nanotechnology* **2019**, *30*, 395703, DOI: 10.1088/1361-6528/ab2cf2.

(40) De Jonge, N. Theory of the spatial resolution of (scanning) transmission electron microscopy in liquid water or ice layers. *Ultramicroscopy* **2018**, *187*, 113–125, DOI: 10.1016/j.ultramic.2018.01.007.

(41) Dukes, M. J.; Thomas, R.; Damiano, J.; Klein, K. L.; Balasubramaniam, S.; Kayandan, S.; Riffle, J. S.; Davis, R. M.; McDonald, S. M.; Kelly, D. F. Improved Microchip Design and Application for In Situ Transmission Electron Microscopy of Macromolecules. *Microscopy and Microanalysis* **2014**, *20*, 338–345, DOI: 10.1017/S1431927613013858.

(42) Kennedy, E.; Nelson, E. M.; Tanaka, T.; Damiano, J.; Timp, G. Live Bacterial Physiology Visualized with 5 nm Resolution Using Scanning Transmission Electron Microscopy. *ACS Nano* **2016**, *10*, 2669–2677, DOI: 10.1021/acsnano.5b07697.

(43) Sugihara, A.; Ishida, T. Microfluidic Liquid Cell with Silicon Nitride Super-Thin Membrane for Electron Microscopy of Samples in Liquid. *Biosensors* **2022**, *12*, 1138, DOI: 10.3390/bios12121138.

(44) Mirsaidov, U. M.; Zheng, H.; Casana, Y.; Matsudaira, P. Imaging Protein Structure in Water at 2.7 nm Resolution by Transmission Electron Microscopy. *Biophysical Journal* **2012**, *102*, L15–L17, DOI: 10.1016/j.bpj.2012.01.009.

(45) Egerton, R. F. Radiation damage to organic and inorganic specimens in the TEM. *Micron* **2019**, *119*, 72–87, DOI: 10.1016/j.micron.2019.01.005.

(46) Stenn, K.; Bahr, G. Specimen damage caused by the beam of the transmission electron microscope, a correlative reconsideration. *Journal of Ultrasructure Research* **1970**, *31*, 526–550, DOI: 10.1016/S0022-5320(70)90167-X.

(47) De Jonge, N.; Houben, L.; Dunin-Borkowski, R. E.; Ross, F. M. Resolution and aberration correction in liquid cell transmission electron microscopy. *Nature Reviews Materials* **2019**, *4*, 61–78, DOI: 10.1038/s41578-018-0071-2.

(48) Radisic, A.; Vereecken, P. M.; Hannon, J. B.; Searson, P. C.; Ross, F. M. Quantifying Electrochemical Nucleation and Growth of Nanoscale Clusters Using Real-Time Kinetic Data. *Nano Letters* **2006**, *6*, 238–242, DOI: 10.1021/nl052175i.

(49) Carini, P.; Steindler, L.; Beszteri, S.; Giovannoni, S. J. Nutrient requirements for growth of the extreme oligotroph 'Candidatus Pelagibacter ubique' HTCC1062 on a defined medium. *The ISME Journal* **2013**, *7*, 592–602, DOI: 10.1038/ismej.2012.122.

(50) Telea, A. An Image Inpainting Technique Based on the Fast Marching Method. *Journal of Graphics Tools* **2004**, *9*, 23–34, DOI: 10.1080/10867651.2004.10487596.

(51) Bradski, G. The OpenCV Library. *Dr. Dobb's Journal of Software Tools* **2000**.

(52) Damelin, S. B.; Hoang, N. S. On Surface Completion and Image Inpainting by Biharmonic Functions: Numerical Aspects. *International Journal of Mathematics and Mathematical Sciences* **2018**, *2018*, e3950312, DOI: 10.1155/2018/3950312.

(53) Van der Walt, S.; Schönberger, J. L.; Nunez-Iglesias, J.; Boulogne, F.; Warner, J. D.; Yager, N.; Gouillart, E.; Yu, T. scikit-image: image processing in Python. *PeerJ* **2014**, *2*, e453.

(54) Riley, M. E.; MacCallum, C. J.; Biggs, F. Theoretical electron-atom elastic scattering cross sections. *Atomic Data and Nuclear Data Tables* **1975**, *15*, 443–476, DOI: 10.1016/0092-640X(75)90012-1.

(55) Grilli, M. L.; Valerini, D.; Rizzo, A.; Yilmaz, M.; Song, C.; Hu, G.; Mikhaylov, A.; Chierchia, R.; Rinaldi, A. A Comparative Study of the Mechanical and Tribological Properties of Thin Al2O3 Coatings Fabricated by Atomic Layer Deposition and Radio Frequency Sputtering. *physica status solidi (a)* **2022**, *219*, 2100398, DOI: 10.1002/pssa.202100398.

(56) Krautheim, G.; Hecht, T.; Jakschik, S.; Schröder, U.; Zahn, W. Mechanical stress in ALD-Al2O3 films. *Applied Surface Science* **2005**, *252*, 200–204, DOI: 10.1016/j.apsusc.2005.01.118.

(57) Iakoubovskii, K.; Mitsuishi, K.; Nakayama, Y.; Furuya, K. Thickness measurements with electron energy loss spectroscopy. *Microscopy Research and Technique* **2008**, *71*, 626–631, DOI: 10.1002/jemt.20597.

(58) Malis, T.; Cheng, S. C.; Egerton, R. F. EELS log-ratio technique for specimen-thickness measurement in the TEM. *Journal of Electron Microscopy Technique* **1988**, *8*, 193–200, DOI: 10.1002/jemt.1060080206.

(59) Yesibolati, M. N.; Laganá, S.; Kadkhodazadeh, S.; Mikkelsen, E. K.; Sun, H.; Kasama, T.; Hansen, O.; Zaluzec, N. J.; Mølhave, K. Electron inelastic mean free path in water. *Nanoscale* **2020**, *12*, 20649–20657, DOI: 10.1039/D0NR04352D.

(60) Lenz, F. Zur Streuung mittelschneller Elektronen in kleinste Winkel. *Zeitschrift für Naturforschung A* **1954**, *9*, 185–204, DOI: 10.1515/zna-1954-0301.

(61) Yen, B. K.; White, R. L.; Waltman, R. J.; Dai, Q.; Miller, D. C.; Kellock, A. J.; Marchon, B.; Kasai, P. H.; Toney, M. F.; York, B. R.; Deng, H.; Xiao, Q.-F.; Raman, V. Microstructure and properties of ultrathin amorphous silicon nitride protective coating. *Journal of Vacuum Science & Technology A* **2003**, *21*, 1895–1904, DOI: 10.1116/1.1615974.

(62) Milo, R.; Phillips, R. In *Cell biology by the numbers*; Garland Science, Taylor & Francis Group: New York, NY, 2016, pp 3–64.

(63) Marchello, G.; De Pace, C.; Wilkinson, N.; Ruiz-Perez, L.; Battaglia, G. 4D Liquid-phase Electron Microscopy of Ferritin by Brownian Single Particle Analysis, 2019, DOI: 10.48550/arXiv.1907.03348.

(64) Kim, M.; Rho, Y.; Jin, K. S.; Ahn, B.; Jung, S.; Kim, H.; Ree, M. pH-Dependent Structures of Ferritin and Apoferritin in Solution: Disassembly and Reassembly. *Biomacromolecules* **2011**, *12*, 1629–1640, DOI: 10.1021/bm200026v.

(65) Narayanan, S.; Shahbazian-Yassar, R.; Shokuhfar, T. In Situ Visualization of Ferritin Biomineralization via Graphene Liquid Cell-Transmission Electron Microscopy. *ACS Biomaterials Science & Engineering* **2020**, *6*, 3208–3216, DOI: 10.1021/acsbiomaterials.9b01889.

(66) Heusterspreute, M.; Crichton, R. R. Amino acid sequence of horse spleen apoferritin. *FEBS letters* **1981**, *129*, 322–327, DOI: 10.1016/0014-5793(81)80193-7.

(67) Granick, S. Ferritin: I. Physical And Chemical Properties Of Horse Spleen Ferritin. *Journal of Biological Chemistry* **1942**, *146*, 451–461, DOI: 10.1016/S0021-9258(18)44965-4.

(68) Voet, D.; Voet, J. G., *Biochemistry*; John Wiley & Sons: 2010.

(69) Tablin, F.; Weiss, L. The equine spleen: an electron microscopic analysis. *The American Journal of Anatomy* **1983**, *166*, 393–416, DOI: 10.1002/aja.1001660403.

(70) Hansma, H. G.; Vesenka, J.; Siegerist, C.; Kelderman, G.; Morrett, H.; Sinsheimer, R. L.; Elings, V.; Bustamante, C.; Hansma, P. K. Reproducible imaging and dissection of plasmid DNA under liquid with the atomic force microscope. *Science* **1992**, *256*, 1180–1185, DOI: 10.1126/science.256.5060.1180.

(71) Lyubchenko, Y.; Luda, S.; Aki, T.; Adhya, S. Atomic Force Microscopic Demonstration of DNA Looping by GalR and HU. *Nucleic acids research* **1997**, *25*, 873–6, DOI: 10.1093/nar/25.4.873.

(72) Bultema, L. A.; Bücker, R.; Schulz, E. C.; Tellkamp, F.; Gonschior, J.; Miller, R. J. D.; Kassier, G. H. The effect of secondary electrons on radiolysis as observed by in liquid TEM: The role of window material and electrical bias. *Ultramicroscopy* **2022**, *240*, 113579, DOI: 10.1016/j.ultramic.2022.113579.

(73) Zhao, X.; Schwartz, C. L.; Pierson, J.; Giovannoni, S. J.; McIntosh, J. R.; Nicastro, D. Three-Dimensional Structure of the Ultraoligotrophic Marine Bacterium "Candidatus Pelagibacter ubique". *Applied and Environmental Microbiology* **2017**, *83*, e02807–16, DOI: 10.1128/AEM.02807-16.

(74) Woehl, T. J.; Kashyap, S.; Firlar, E.; Perez-Gonzalez, T.; Faivre, D.; Trubitsyn, D.; Bazylinski, D. A.; Prozorov, T. Correlative Electron and Fluorescence Microscopy of Magnetotactic Bacteria in Liquid: Toward In Vivo Imaging. *Scientific Reports* **2014**, *4*, 6854, DOI: 10.1038/srep06854.

(75) Ercius, P. openNCEM: A collection of packages and tools for electron microscopy data analysis supported by the National Center for Electron Microscopy facility of the Molecular Foundry.

(76) De la Peña, F. et al. hyperspy/hyperspy: Release v1.7.3, version v1.7.3, 2022, DOI: 10.5281/zenodo.7263263.

(77) Collette, A., *Python and HDF5*; O'Reilly: 2013.

(78) Schneider, C. A.; Rasband, W. S.; Eliceiri, K. W. NIH Image to ImageJ: 25 years of image analysis. *Nature Methods* **2012**, *9*, 671–675, DOI: 10.1038/nmeth.2089.

(79) Egerton, R. F. Electron energy-loss spectroscopy in the TEM. *Reports on Progress in Physics* **2008**, *72*, 016502, DOI: 10.1088/0034-4885/72/1/016502.

(80) Keskin, S.; Besztejan, S.; Kassier, G.; Manz, S.; Bücker, R.; Riekeberg, S.; Trieu, H. K.; Rentmeister, A.; Miller, R. J. D. Visualization of Multimerization and Self-Assembly of DNA-Functionalized Gold Nanoparticles Using In-Liquid Transmission Electron Microscopy. *The Journal of Physical Chemistry Letters* **2015**, *6*, 4487–4492, DOI: 10.1021/acs.jpclett.5b02075.

(81) Bethe, H. In *Quantentheorie*, Bethe, H., Hund, F., Mott, N. F., Pauli, W., Rubinowicz, A., Wentzel, G., Smekal, A., Eds.; Handbuch der Physik; Springer: Berlin, Heidelberg, 1933, pp 273–560, DOI: 10.1007/978-3-642-52619-0_3.

(82) Yao, L.; Ou, Z.; Luo, B.; Xu, C.; Chen, Q. Machine Learning to Reveal Nanoparticle Dynamics from Liquid-Phase TEM Videos. *ACS Central Science* **2020**, *6*, 1421–1430, DOI: 10.1021/acscentsci.0c00430.

(83) Stevens, A.; Yang, H.; Carin, L.; Arslan, I.; Browning, N. D. The potential for Bayesian compressive sensing to significantly reduce electron dose in high-resolution STEM images. *Microscopy* **2014**, *63*, 41–51, DOI: 10.1093/jmicro/dft042.

(84) Bertalmio, M.; Sapiro, G.; Caselles, V.; Ballester, C. In *Proceedings of the 27th annual conference on Computer graphics and interactive techniques*, ACM Press/Addison-Wesley Publishing Co.: USA, 2000, pp 417–424, DOI: 10.1145/344779.344972.

(85) Ede, J. M.; Beanland, R. Partial Scanning Transmission Electron Microscopy with Deep Learning. *Scientific Reports* **2020**, *10*, 8332, DOI: 10.1038/s41598-020-65261-0.

(86) Sanders, T.; Dwyer, C. Inpainting Versus Denoising for Dose Reduction in Scanning-Beam Microscopies. *IEEE Transactions on Image Processing* **2020**, *29*, 351–359, DOI: 10.1109/TIP.2019.2928133.

(87) Kovarik, L.; Stevens, A.; Liyu, A.; Browning, N. D. Implementing an accurate and rapid sparse sampling approach for low-dose atomic resolution STEM imaging. *Applied Physics Letters* **2016**, *109*, 164102, DOI: 10.1063/1.4965720.

(88) Sang, X.; Lupini, A. R.; Unocic, R. R.; Chi, M.; Borisevich, A. Y.; Kalinin, S. V.; Endeve, E.; Archibald, R. K.; Jesse, S. Dynamic scan control in STEM: spiral scans. *Advanced Structural and Chemical Imaging* **2016**, *2*, 6, DOI: 10.1186/s40679-016-0020-3.

(89) Trépout, S. Tomographic Collection of Block-Based Sparse STEM Images: Practical Implementation and Impact on the Quality of the 3D Reconstructed Volume. *Materials* **2019**, *12*, 2281, DOI: 10.3390/ma12142281.

(90) Sang, X.; Lupini, A.; Ding, J.; Kalinin, S.; Jesse, S.; Unocic, R. Precision controlled atomic resolution scanning transmission electron microscopy using spiral scan pathways. *Scientific Reports* **2017**, *7*, 43585, DOI: 10.1038/srep43585.

(91) Turnbaugh, C.; Axelrod, J. J.; Campbell, S. L.; Dioquino, J. Y.; Petrov, P. N.; Remis, J.; Schwartz, O.; Yu, Z.; Cheng, Y.; Glaeser, R. M.; Mueller, H. High-power

near-concentric Fabry–Perot cavity for phase contrast electron microscopy. *Review of Scientific Instruments* **2021**, *92*, 053005, DOI: 10.1063/5.0045496.

(92) Russo, C. J.; Passmore, L. A. Controlling protein adsorption on graphene for cryo-EM using low-energy hydrogen plasmas. *Nature methods* **2014**, *11*, 649–652, DOI: 10.1038/nmeth.2931.

(93) Dearnaley, W. J.; Schleupner, B.; Varano, A. C.; Alden, N. A.; Gonzalez, F.; Casasanta, M. A.; Scharf, B. E.; Dukes, M. J.; Kelly, D. F. Liquid-Cell Electron Tomography of Biological Systems. *Nano Letters* **2019**, *19*, 6734–6741, DOI: 10.1021/acs.nanolett.9b01309.

(94) Wang, C.; Qiao, Q.; Shokuhfar, T.; Klie, R. F. High-Resolution Electron Microscopy and Spectroscopy of Ferritin in Biocompatible Graphene Liquid Cells and Graphene Sandwiches. *Advanced Materials* **2014**, *26*, 3410–3414, DOI: 10.1002/adma.201306069.

(95) Marchello, G.; De Pace, C.; Duro-Castano, A.; Battaglia, G.; Ruiz-Pérez, L. End-to-end image analysis pipeline for liquid-phase electron microscopy. *Journal of Microscopy* **2020**, *279*, 242–248, DOI: 10.1111/jmi.12889.

(96) Knaus, C.; Zwicker, M. Progressive Image Denoising. *IEEE Transactions on Image Processing* **2014**, *23*, 3114–3125, DOI: 10.1109/TIP.2014.2326771.

(97) Béché, A.; Goris, B.; Freitag, B.; Verbeeck, J. Development of a fast electromagnetic beam blanker for compressed sensing in scanning transmission electron microscopy. *Applied Physics Letters* **2016**, *108*, 093103, DOI: 10.1063/1.4943086.

(98) Barclay, G. G. In *Encyclopedia of Materials: Science and Technology*, Buschow, K. H. J., Cahn, R. W., Flemings, M. C., Ilschner, B., Kramer, E. J., Mahajan, S., Veyssière, P., Eds.; Elsevier: Oxford, 2001, pp 1–3, DOI: 10.1016/B0-08-043152-6/01384-X.

Appendices

Appendix A

Photolithography

The general scheme for photolithography can be found in Figure A.1. A photoresist is a thick polymer that is deposited onto a wafer surface by a process called spin-coating.[98] During spin-coating the wafer is secured to a chuck (normally by vacuum), the photoresist is poured onto the surface, and the chuck is spun at 1000-4000rpm to spread an even layer of photoresist across the wafer. The wafer is baked to solidify the photoresist. The wafer is then exposed to UV light in a specific pattern or using a physical mask. A positive photoresist is weakened by UV light, and a negative photoresist is strengthened by UV light.[98] The wafer is then bathed in a developer chemical which dissolves the exposed photoresist (positive) or unexposed photoresist (negative). Then the pattern is complete.[98]

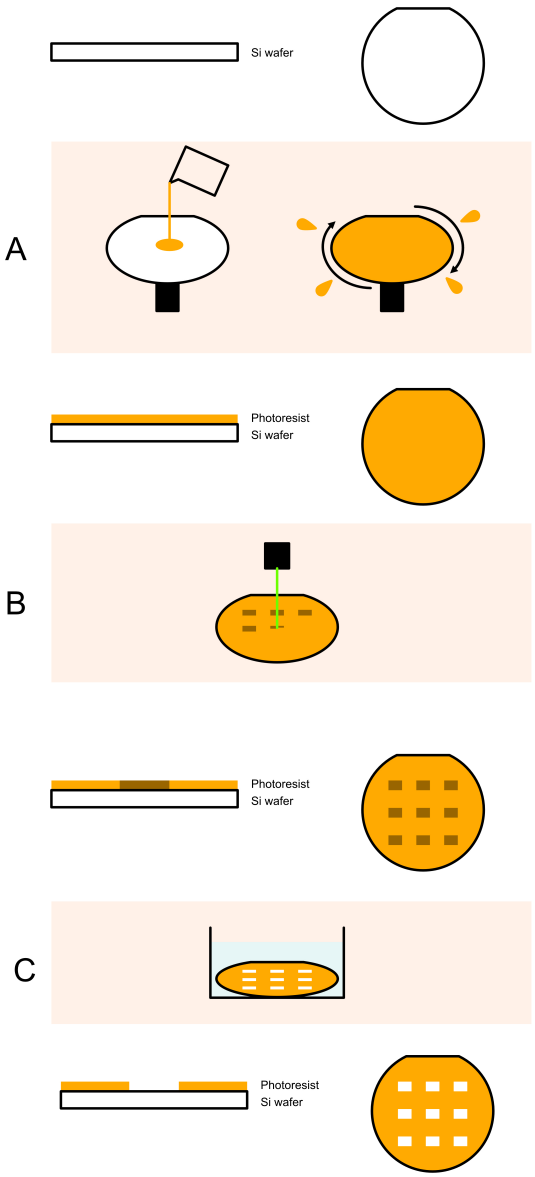


Figure A.1: General scheme for patterning a mask on a wafer via photolithography. Panel A shows the first step, where a photoresist is spin-coated onto the wafer. Panel B shows the second step, where the photoresist is exposed to a laser in a patterned fashion. Panel C shows the final step of creating the photoresist mask, where the wafer is exposed to a developing solution, which removes the photoresist pattern. In this example, a positive photoresist is depicted.

Appendix B

Inpainting results

The figures below show the raw outputs for each of the results shown in Figures 8.4 and 8.3. The percentage of inpainting corresponds to the amount of data removed from the original image before the inpainting algorithm is run on the masked image. For example, the 80% inpainted image has 80% of the original pixels within the original area removed. In this example, the spiral-masked image has 80% of the pixels in the circular region removed, and the random-masked has 0% of the total pixels removed.

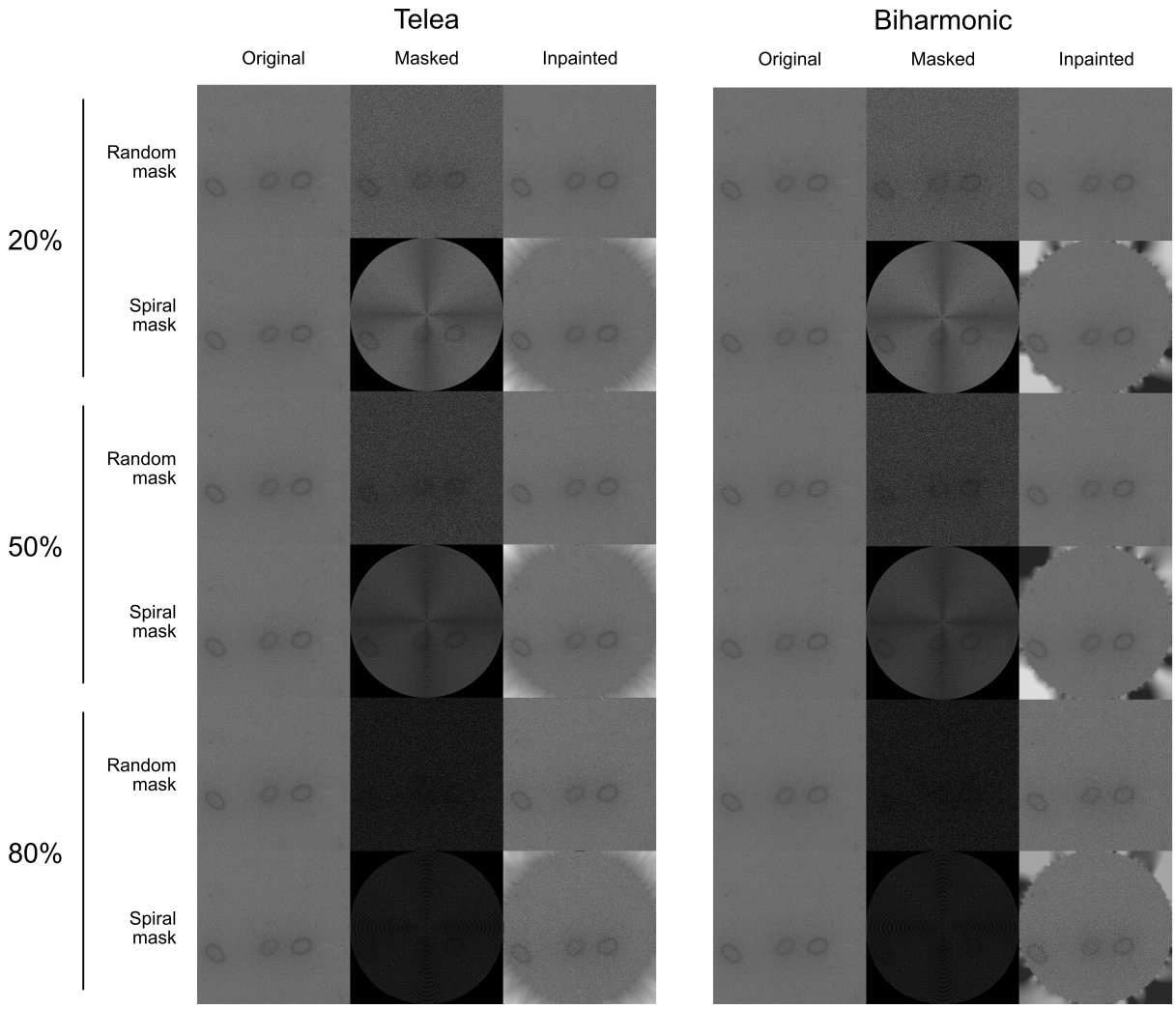


Figure B.1: Inpainting results for selected image of vesicles. Each test shows the original image, the masked image, and the inpainting result. The left panel shows data from the Telea algorithm, and the right panel shows data from the biharmonic algorithm. Each test was run using a random mask (above) and spiral mask (below) at 20%, 50% and 80% inpainting.

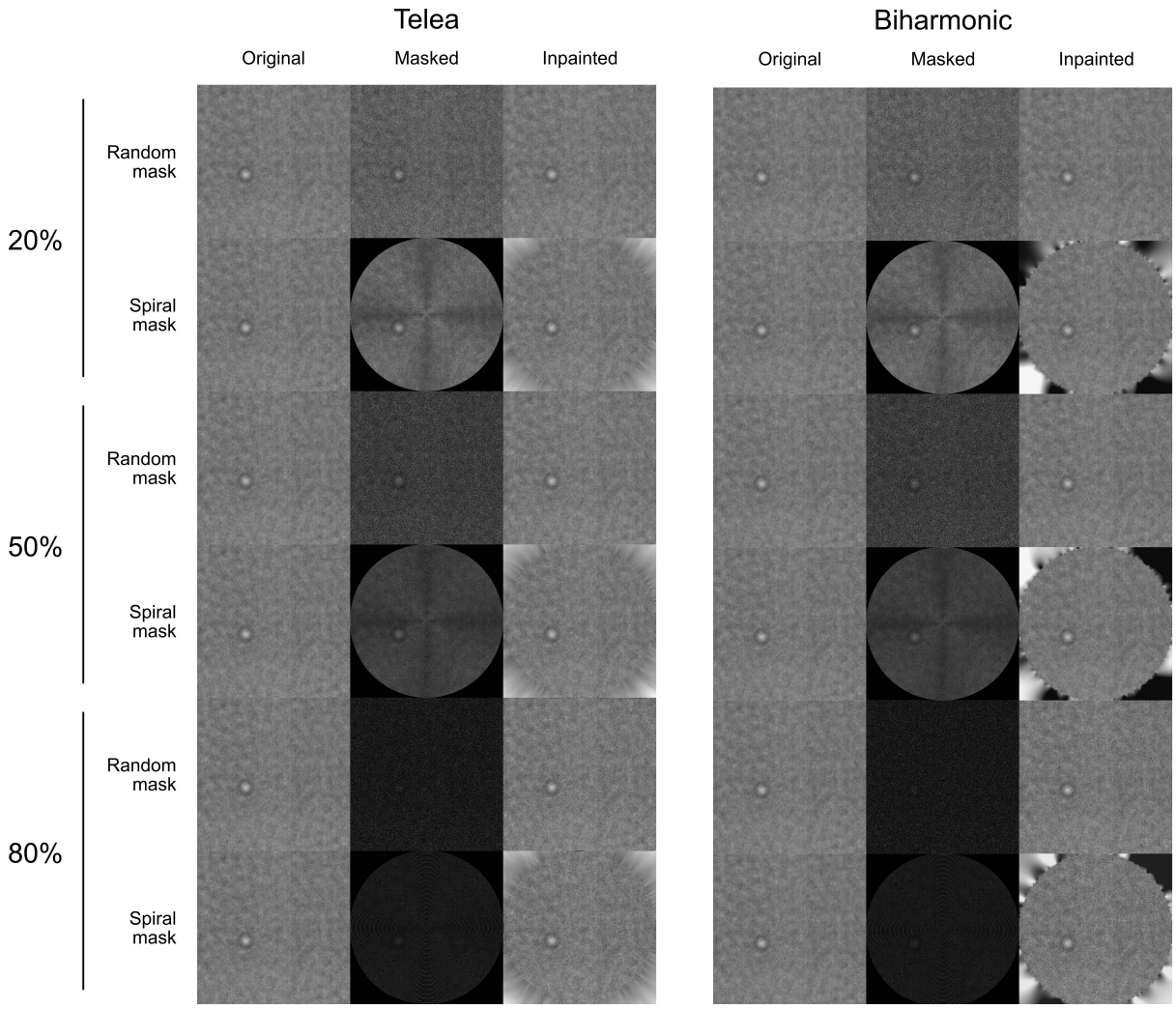


Figure B.2: Inpainting results for selected image of AAV. Each test shows the original image, the masked image, and the inpainting result. The left panel shows data from the Telea algorithm, and the right panel shows data from the biharmonic algorithm. Each test was run using a random mask (above) and spiral mask (below) at 20%, 50% and 80% inpainting.

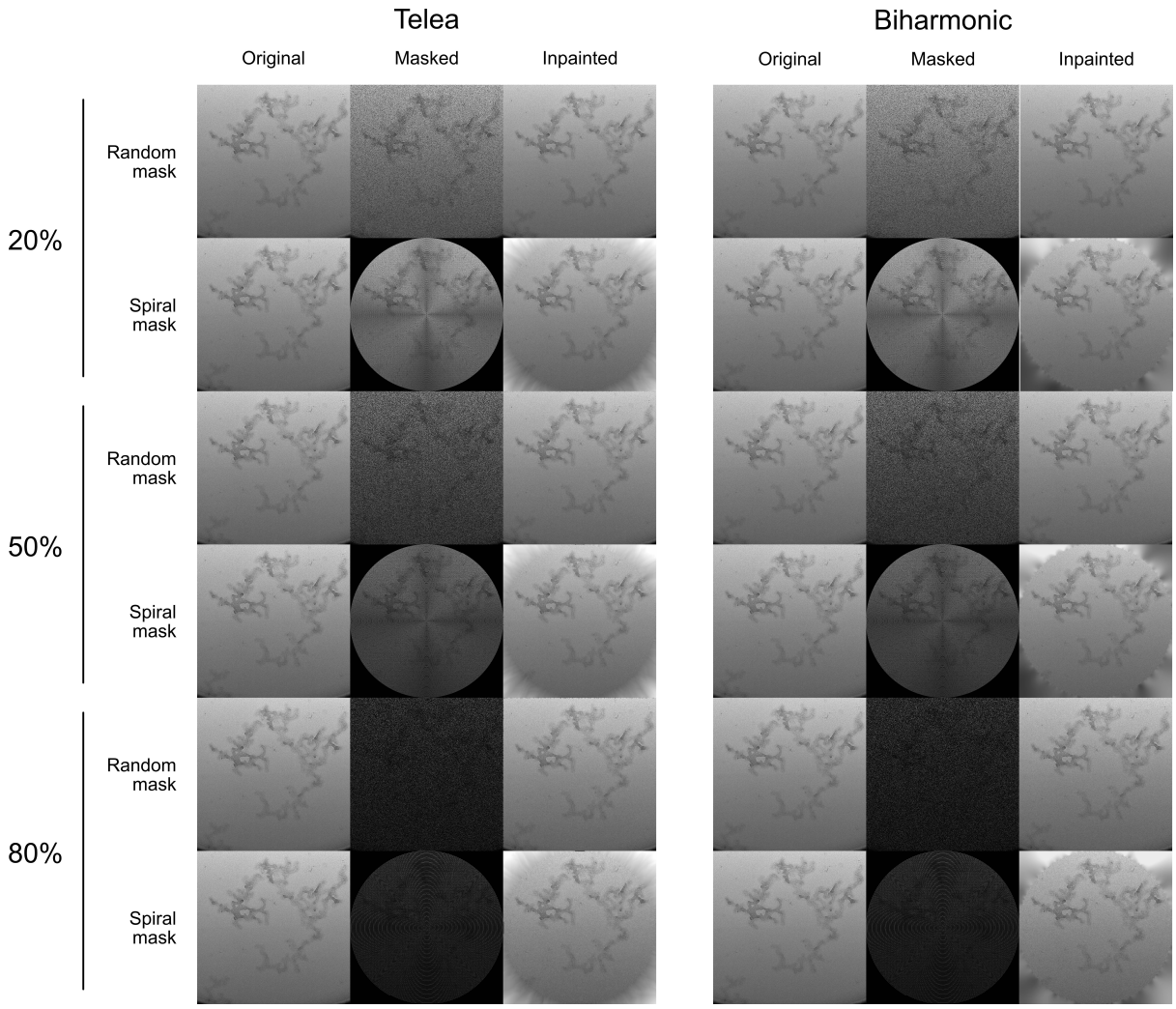


Figure B.3: Inpainting results for selected image of pAAV plasmid. Each test shows the original image, the masked image, and the inpainting result. The left panel shows data from the Telea algorithm, and the right panel shows data from the biharmonic algorithm. Each test was run using a random mask (above) and spiral mask (below) at 20%, 50% and 80% inpainting.

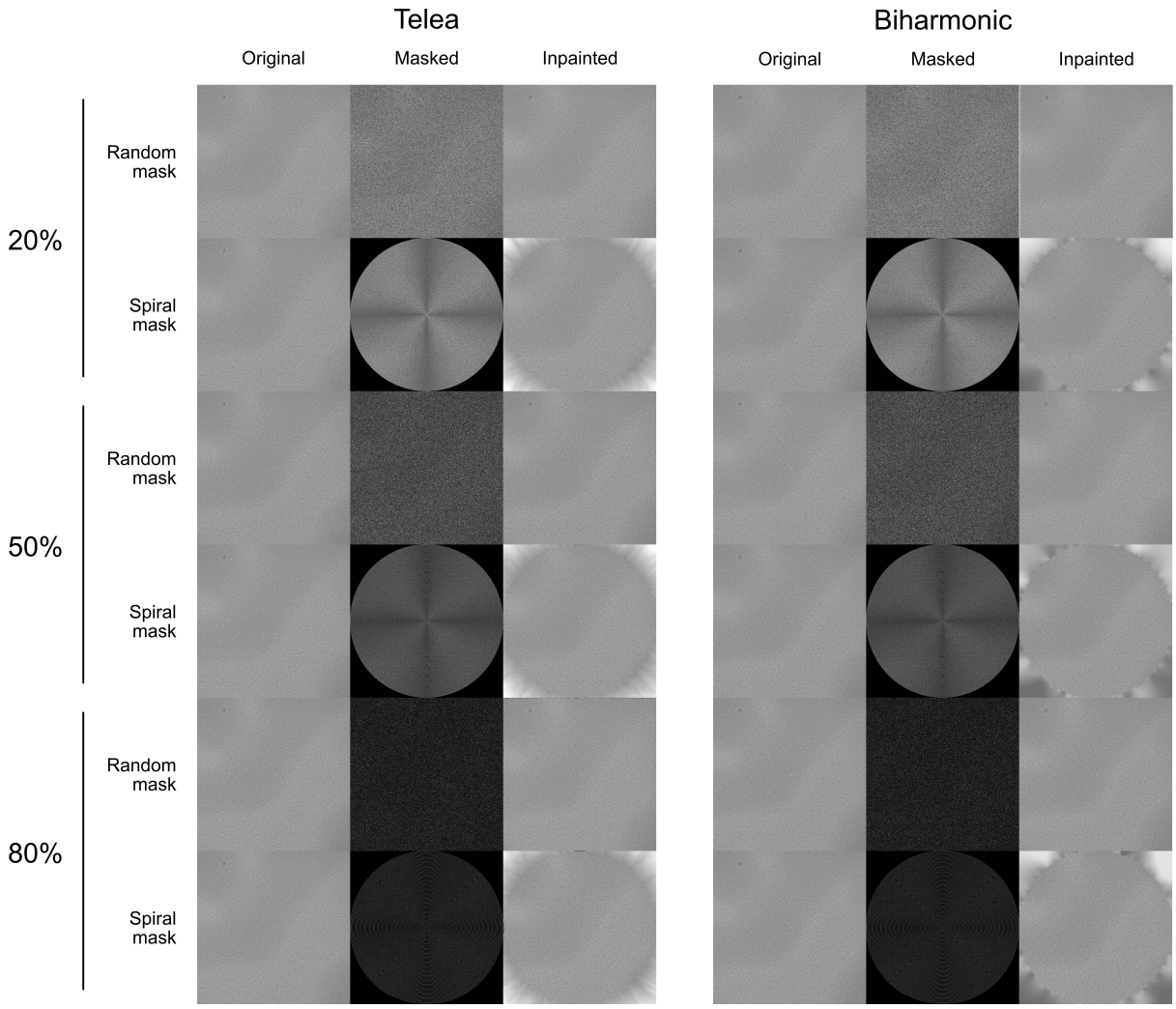


Figure B.4: Inpainting results for selected image of vesicles. Each test shows the original image, the masked image, and the inpainting result. The left panel shows data from the Telea algorithm, and the right panel shows data from the biharmonic algorithm. Each test was run using a random mask (above) and spiral mask (below) at 20%, 50% and 80% inpainting.

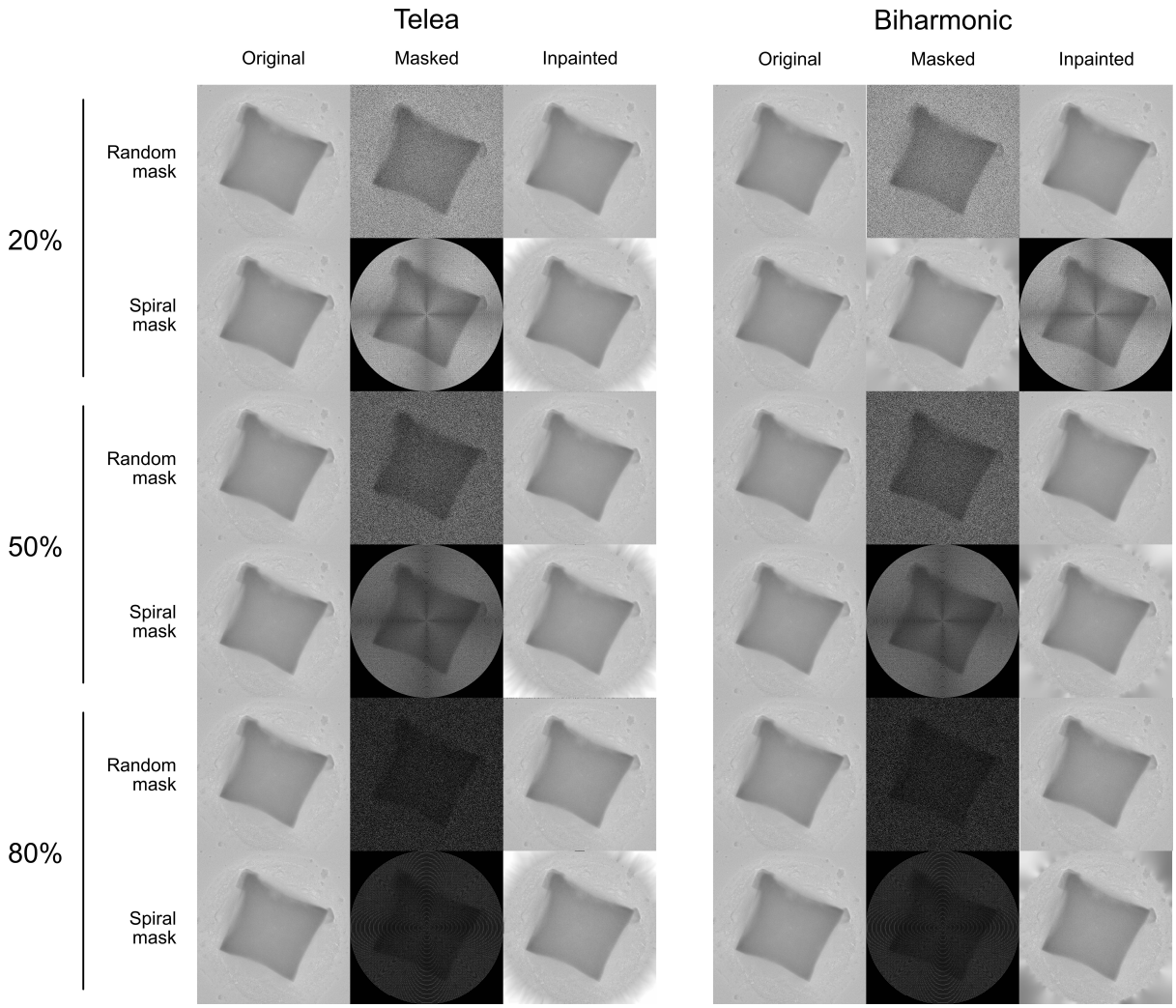


Figure B.5: Inpainting results for selected image of salt. Each test shows the original image, the masked image, and the inpainting result. The left panel shows data from the Telea algorithm, and the right panel shows data from the biharmonic algorithm. Each test was run using a random mask (above) and spiral mask (below) at 20%, 50% and 80% inpainting.

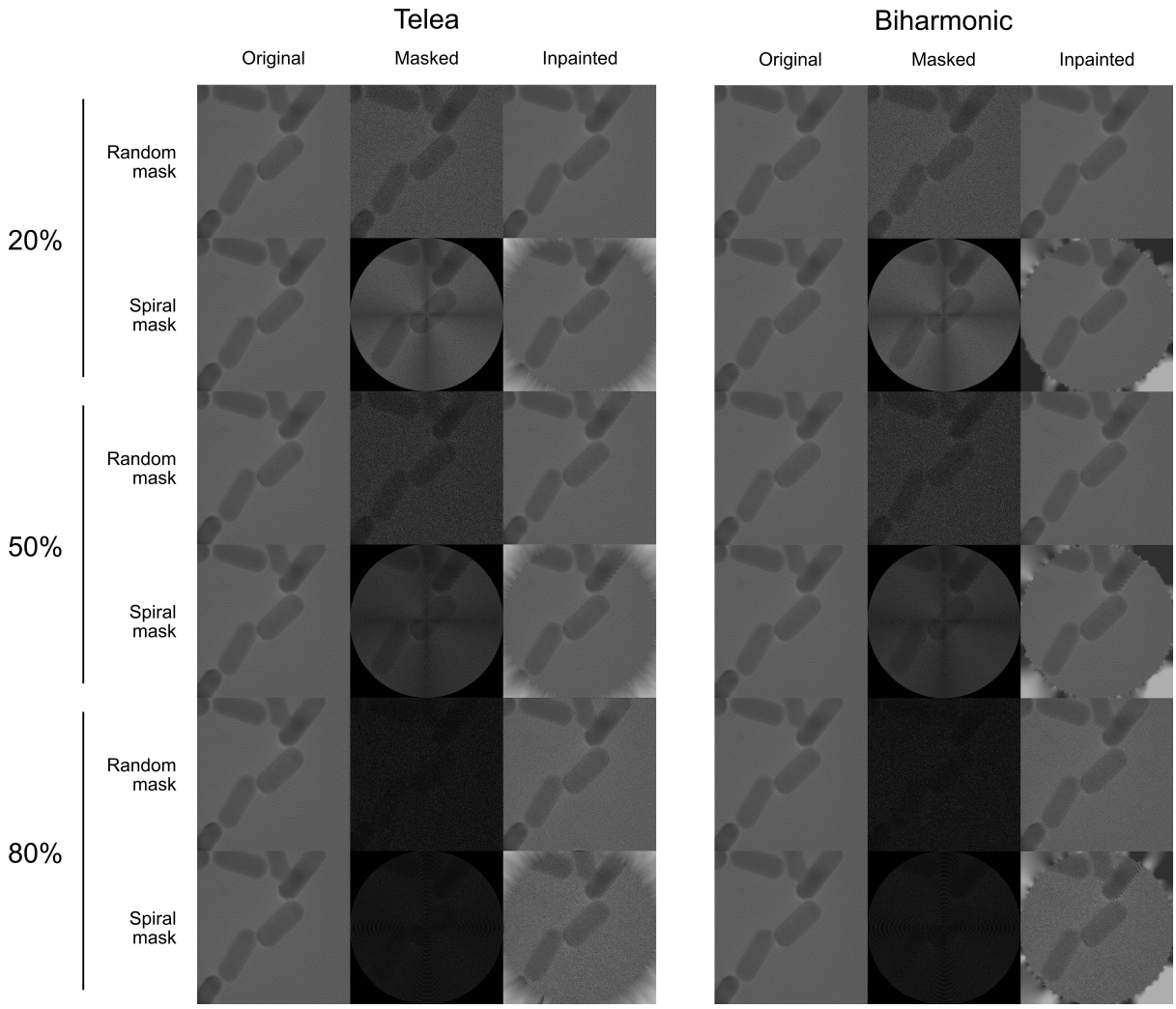


Figure B.6: Inpainting results for selected image of gold nanoparticles. Each test shows the original image, the masked image, and the inpainting result. The left panel shows data from the Telea algorithm, and the right panel shows data from the biharmonic algorithm. Each test was run using a random mask (above) and spiral mask (below) at 20%, 50% and 80% inpainting.

Appendix C

Electron dose calculations

Two methods were used to estimate the electron dose in Figure C.1. Methods 1 and 2 (shown below) yield dose rates of 0.13 $e^{-}A^{-2}s^{-1}$ or 7.3 $e^{-}A^{-2}s^{-1}$, and critical doses of 16 $e^{-}A^{-2}$ or 872 $e^{-}A^{-2}$ (where A is area). In the video of vesicle degradation taken immediately after this image was taken, the magnification is increased (and beam size was condensed), thus the dose rate and critical dose values are underestimated. Regardless, both of these calculations are on the order of magnitude expected for biosamples (see chapter 8.1). Accurate dose estimation requires calibration of the microscope being used with a Faraday cup, which has yet to be performed in the microscope used.

C.1 Method 1: Screen current

Screen current is measured on a fluorescent screen in the TEM, the screen is coated in a phosphor layer. When accelerated electrons hit the screen, photons are emitted via

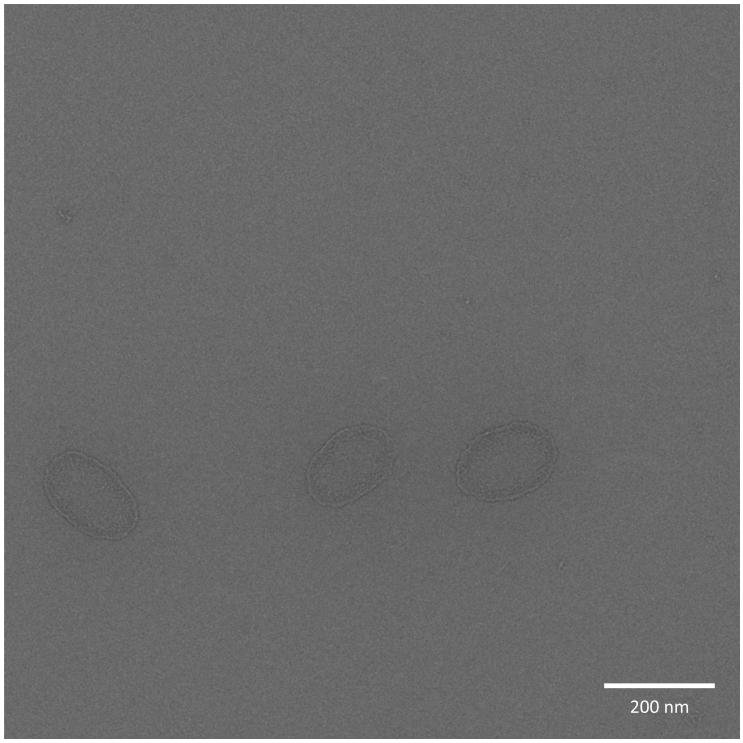


Figure C.1: Image of vesicles to estimate dose rate. The image shows vesicles similar to that in Figure 6.4 but at a lower magnification. The scalebar is indicated on the image.

Microscope	Spectra Ultra
Acceleration votlage	300 keV
Detector	BM-Ceta
Exposure	0.5 seconds
Screen current	2.038 nA
Beam convergence angle	0.0452 mrad
Camera length	0.139 m
Pixel size	0.833 nm x 0.833 nm
Image size	4096 pixels x 4096 pixels
Counts to electrons	0.0402
Pixel value to camera counts	1
Pixel value sum	1908042257

Table C.1: Metadata summary for the image of vesicles describing dose. The metadata shown is associated with the image shown in Figure C.1, the first image in a set of further images at higher magnification showing the destruction of the vesicles (see Figure 6.4).

phosphorescence.[12] The screen current can be used to measure the dose of the image. This method relies on the ability to estimate the size of the beam interacting with the sample relative to the area where the beam hits the fluorescent screen. Assuming the beam is convergent around the area of the frame (such that the edge is just outside the area of the frame), the area of the beam relative to the image is approximately 1.5 times.[1] We assume that the screen current measures the entire beam, thus the dose rate (Φ) is given by equation C.1. Where the screen current is I in Amperes, 6.28×10^{18} is the conversion to $e^{-}s^{-1}$, and the image area is A. The dose rate for this frame is thus 7.3 $e^{-}A^{-2}s^{-1}$. The vesicle lasts 119 seconds before degradation is seen, thus the critical dose for the vesicles is 872 $e^{-}A^{-2}$.

$$\Phi = \frac{I \times 6.28 \times 10^{18}}{A \times 1.5} \tag{C.1}$$

C.2 Method 2: Counts to electrons

The metadata contains a value for the conversion of detector counts to electrons. Thus when given the raw pixel values (0 - 9079) and pixel to electron counts value, the electrons incident on the image can be calculated. Here the pixel values are averaged over the area of the image, then converted to the camera counts (1:1), and converted to the electron counts. The dose rate is calculated to be 0.13 $e^{-}A^{-2}s^{-1}$, and with 119 seconds of imaging, the critical dose is 16 $e^{-}A^{-2}$.

Glossary

annealing The process of exposing a film to high temperature in a specific gas environment, to alter the film's physical and chemical properties.

atomic force microscopy (AFM) A technique used to measure the profile of features fabricated on wafers and chips, more precise than profilometry.

atomic layer deposition (ALD) A deposition technique based on gas phase chemical processes that grow thin films on a substrate.

Bernoulli A truly sparse matrix. The signals are essentially random, with the added criterion that the signals are evenly distributed.

biomolecule A molecule produced by biological organisms (e.g. DNA, lipids, proteins), or the organism itself (e.g. biological cells, viruses).

chip A single silicon piece of the LC assembly. See figure 1.2.

constant linear velocity (CLV) A type of spiral scan acquired with a constant linear velocity.

conventional transmission electron microscopy (CTEM) A type of glstem imaging mode where the beam is spread over a large area when the image is acquired.

critical dose The threshold cumulative dose before a sample begins to become damaged, measured in $e^{-}Area^{-2}$.

cryogenic electron microscopy (cryo EM) TEM experiments performed on samples frozen in vitreous ice (amorphous ice).

denoising A computational technique used to remove noise from an image.

dose rate The rate of electron dose, measured in $e^{-}Area^{-2}s^{-1}$. Also referred to as electron flux.

ellipsometry A technique used to measure thicknesses of thin films. The technique measures the change in the polarisation of light reflected off or transmitted through a surface and provides information on the dielectric properties of the film(s).

epitaxy film deposition characterised as having a high degree of matching orientation to the base layer, typically associated with high crystallinity and low stress between the base and deposited film.

fly-back time The time taken to move from the end of one line to the beginning of the next line when scanning in a raster fashion in STEM mode.

holder The apparatus housing the LC assembly that is inserted into the TEM.

inelastic mean free path (λ_{inel}) The average distance an inelastically scattered electron travels through a material before its energy or direction changes.

inpainting A computational technique used to reconstruct an image with missing pixels.

interferometry A technique that uses the superimposition of waves to measure film properties, for example, lasers can be used to measure the slight curvatures on a wafer surface before and after deposition of a film to measure stress.

isophote A line connecting points of equal brightness, or the sections of a gradient.

Lenard window A thin layer of aluminium foil strong enough to preserve vacuum in the chamber of a Crookes tube (and electrical discharge tube, with partial vacuum).

liquid cell (LC) An assembly that encloses liquid sample for liquid phase electron microscopy experiments.

loading station The apparatus used to assemble the LC assembly in the holder.

low-pressure chemical vapour deposition (LPCVD) A chemical vapour deposition technique that uses heat and low pressure to grow thin films on a substrate.

pAAV Plasmid DNA for AAV cloning.

photolithography The process of patterning features on a wafer photolithography techniques, see Appendix A

pillar The area on a LC chip that holds the window, where the height between the spacer and the pillar dictates the nominal sample thickness.

piranha A mixture used to clean wafer surfaces of concentrated sulfuric acid and 30% hydrogen peroxide, where the ratio is typically 2:1 for a strong clean, and 3:4 for a gentle clean.

profilometer A tool used to measure the profile of features fabricated on wafers and chips.

scannning transmission electron microscopy (STEM) A type of glstem imaging mode where the beam is focused to a probe and raster scanned over the sample to acquire an image.

spacer The material that contacts between two LC chips which ideally determines thickness of the sample between the two windows.

total mean free path (Λ_{tot}) The average distance an electron travels through a material before its energy or direction changes.

wafer A thin, circular, semiconductor material, such as silicon, used as a base for fabrication.

window The area containing a thin, freestanding, transmissive film in LC chips where the TEM electron beam passes through and produced an image.

x-ray crystallography A technique to measure the structure of a crystal through diffraction of x-rays.

zero loss peak (ZLP) The peak at the beginning of an EELS spectrum that represents non scattered and elastically scattered electrons.